



## AN ABSTRACT OF THE THESIS OF

Adam Brigantic for the degree of Master of Science in Nuclear Engineering presented on September 26, 2014.

Title: Applying Uncertainty and Sensitivity on Thermal Hydraulic Subchannel Analysis for the Multi-Application Small Light Water Reactor

Abstract approved:

---

Wade R. Marcum

Small modular reactors (SMRs) are a recent advancement in commercial nuclear reactor design with growing interest worldwide. New SMR concepts, such as the Multi-Application Small Light Water Reactor (MASLWR), must undergo a licensing processes established by the U.S. Nuclear Regulatory Commission (NRC) prior to commercial operation. Given the lack of historical, full scale operating experience, a general uncertainty and sensitivity analysis methodology was developed to help aid SMR designs through this process. Uncertainty was quantified through the empirical cumulative distribution function (ECDF) created from a desired data set. Linear regression techniques were applied to measure sensitivity. This methodology was demonstrated through the thermal hydraulic subchannel analysis of the MASLWR concept using RELAP5-3D Version 4.0.3 and VIPRE-01 Mod 2.2.1. Twelve uncertain input parameters were selected. System response uncertainty in the minimum departure from nucleate boiling ratio (MDNBR), maximum fuel temperature, and maximum clad temperature was evaluated. These figures were shown to satisfy U.S. NRC regulatory requirements for steady state operation at the 95 percent probability and 95 percent confidence level under the evaluated conditions. Sensitivity studies showed input parameters affecting local power generation within the core had a large influence on MDNBR, maximum fuel temperature, and maximum clad temperature.

©Copyright by Adam Brigantic  
September 26, 2014  
All Rights Reserved

Applying Uncertainty and Sensitivity on Thermal Hydraulic Subchannel Analysis for  
the Multi-Application Small Light Water Reactor

by  
Adam Brigantic

A THESIS

Submitted to

Oregon State University

in partial fulfillment of  
the requirements for the  
degree of

Master of Science

Presented September 26, 2014  
Commencement June 2015

Master of Science thesis of Adam Brigantic presented on September 26, 2014.

APPROVED:

---

Major Professor, representing Nuclear Engineering

---

Head of the Department of Nuclear Engineering and Radiation Health Physics

---

Dean of the Graduate School

I understand that my thesis will become part of the permanent collection of Oregon State University libraries. My signature below authorizes release of my thesis to any reader upon request.

---

Adam Brigantic, Author

## ACKNOWLEDGEMENTS

I would like to use this opportunity to thank my advisor Dr. Wade Marcum for the invaluable guidance and insights he has provided. His dedication to my success has helped me become a better person.

I would like to thank the faculty members in the Oregon State University Nuclear Engineering Department for the educational opportunities they have provided during my course of study.

I would like to thank those at NuScale Power who have supported me in this endeavor, particularly Kenny Anderson, Wendell Wagner, and Dr. Kent Welter.

I would finally like to thank my friends and family for the support they have given me, my parents Robert and Laurie, and especially my wife Rebecca for her encouragement during this time.

## TABLE OF CONTENTS

<u>Section</u>	<u>Page</u>
1. INTRODUCTION.....	1
Purpose.....	3
Objectives.....	3
2. SURVEY OF LITERATURE .....	5
Overview of Uncertainty Analysis Methodologies.....	5
Code Scaling, Applicability, and Uncertainty.....	5
Response Surface .....	8
Wilks' Method .....	9
Statistical Analysis Using VIPRE-01 .....	10
Natural Convection Subchannel Evaluation Using RELAP5-3D.....	12
Closing .....	14
3. MASLWR DESCRIPTION .....	15
MASLWR Design Overview .....	15
MASLWR Core Geometry .....	17
4. METHODOLOGY.....	19
MASLWR Core Model.....	19
Flow Channel Description.....	20
Axial Flow Resistance.....	23
Axial Nodalization .....	24
Channel Cross Flow Description .....	26
Nuclear Fuel Rod .....	29
Fuel Rod Gap .....	31
Core Power Distribution .....	33
RELAP5-3D Model .....	39
Coolant Source (805) .....	40
Coolant Source to Inlet Plenum Junctions (806).....	41
Inlet Plenum (807).....	41
Inlet Plenum to Core Flow Channel Junctions (401-438).....	41
Core Flow Channels (101-138) .....	41

## TABLE OF CONTENTS (Continued)

<u>Section</u>	<u>Page</u>
Core Crossflow Junctions (201-270) .....	41
Core Heat Structures (1101-1138) .....	42
Core Flow Channels to Coolant Sink Junctions (501-538).....	42
Coolant Sink (810) .....	42
VIPRE Model.....	43
Figures of Merit .....	44
DNB Correlation .....	45
Input Uncertainty .....	46
Input Sampling .....	49
Uncertainty Analysis.....	50
ECDF with Confidence Bands .....	51
Sensitivity Analysis.....	54
Rank Transformation .....	54
Scatter Plots.....	54
Partial Rank Correlation Coefficients .....	55
p-values .....	56
Summary .....	56
5. RESULTS AND DISCUSSION .....	59
Influence of Sample Size .....	59
RELAP5-3D and VIPRE-01 Model Results .....	60
Pressure .....	61
Mass Flux .....	62
Equilibrium Quality .....	64
Heat Flux .....	65
DNBR.....	67
Fuel Centerline Temperature.....	68
Clad Temperature .....	69
Uncertainty Analysis Results .....	71
MDNBR .....	71

## TABLE OF CONTENTS (Continued)

<u>Section</u>	<u>Page</u>
Maximum Fuel Temperature.....	73
Maximum Clad Temperature .....	75
Sensitivity Analysis Results.....	77
MDNBR .....	78
Maximum Fuel Temperature.....	84
Maximum Clad Temperature .....	86
6. CONCLUSIONS.....	88
Observations.....	88
Limitations & Assumptions .....	89
Future Work .....	89
BIBLIOGRAPHY .....	91
NOMENCLATURE.....	96
APPENDIX A (Supplementary Information) .....	100
Flow Channel Type Diagrams .....	100
Cross Flow Geometry .....	105
Sensitivity Analysis Scatter Plots .....	107

## LIST OF FIGURES

<u>Figure</u>	<u>Page</u>
Figure 2-1: Fourteen steps of the CSAU methodology.....	7
Figure 2-2: One-channel RELAP5-3D model used by Marcum et al. [18]. ....	13
Figure 3-1: Layout of MASLWR components [2].....	16
Figure 3-2: Schematic of the MASLWR prototypical core [2].....	17
Figure 3-3: Diagram of a 17x17 assembly with guide tube locations.....	17
Figure 4-1: Assemblies used in the one-quarter model; numbering scheme from [5].	20
Figure 4-2: Channel numbering scheme in the one-quarter MASLWR core model. .	21
Figure 4-3: Square subchannel with guide tube unit dimensions. ....	22
Figure 4-4: Axial nodalization of fuel rod. ....	25
Figure 4-5: Cross flow path between square subchannels with guide tube. ....	27
Figure 4-6: Radial discretization of a nuclear fuel rod. ....	30
Figure 4-7: Fuel temperature profiles with changing gap thickness. ....	33
Figure 4-8: Effect of hot channel factor on overall radial factor profile.....	37
Figure 4-9: RELAP5-3D system model.....	40
Figure 4-10: Normal distribution with mean of zero and standard deviation of one..	52
Figure 4-11: Normal distribution ECDF with confidence bands. ....	53
Figure 4-12: Overall methodology summary.....	58
Figure 5-1: DKW error term versus increasing N.....	60
Figure 5-2: Local pressure in the hot channel.....	61
Figure 5-3: Mass flux distribution through the hot channel.....	62
Figure 5-4: Mass flux with no grid spacers and at zero power. ....	63
Figure 5-5: Equilibrium quality in the hot channel.....	64
Figure 5-6: Clad surface heat flux in the hot channel. ....	66
Figure 5-7: Local DNBR in the hot channel. ....	67
Figure 5-8: Fuel centerline temperature in the hot channel. ....	69
Figure 5-9: Clad surface temperature in the hot channel. ....	70
Figure 5-10: The MDNBR ECDF plot. ....	71
Figure 5-11: The maximum fuel temperature ECDF plot.....	74
Figure 5-12: The maximum clad temperature ECDF plot. ....	76

## LIST OF FIGURES (Continued)

<u>Figure</u>	<u>Page</u>
Figure 5-13: RELAP5-3D MDNBR ranked sensitivity plots. ....	80
Figure 5-14: VIPRE-01 MDNBR ranked sensitivity plots. ....	82
Figure A-1: Flow channel type 1; channel at assembly corner. ....	100
Figure A-2: Flow channel type 2; channel at assembly edge. ....	101
Figure A-3: Flow channel type 3; square subchannel with no guide tube. ....	101
Figure A-4: Flow channel type 4; square subchannel with guide tube. ....	102
Figure A-5: Flow channel type 5; lumped 2x5 channel. ....	102
Figure A-6: Flow channel type 6; lumped 2x5 channel. ....	103
Figure A-7: Flow channel type 7; lumped 4x4 channel. ....	103
Figure A-8: Flow channel type 8; lumped one-quarter assembly. ....	104
Figure A-9: Flow channel type 9; lumped full assembly. ....	104
Figure A-10: RELAP5-3D maximum fuel temperature ranked sensitivity plots. ....	109
Figure A-11: VIPRE-01 maximum fuel temperature ranked sensitivity plots. ....	111
Figure A-12: RELAP5-3D maximum clad temperature ranked sensitivity plots. ....	113
Figure A-13: VIPRE-01 maximum clad temperature ranked sensitivity plots. ....	115

## LIST OF TABLES

<u>Table</u>	<u>Page</u>
Table 2-1: Number of data samples required for the first order Wilks' method. ....	9
Table 3-1: MASLWR steady-state operating conditions. ....	15
Table 3-2: Prototypical MASLWR core geometry [2,22] .....	18
Table 4-1: Description of nine flow channel types. ....	23
Table 4-2: Grid spacer location in fuel assembly.....	26
Table 4-3: Radial geometry of a nuclear fuel rod. ....	30
Table 4-4: Nominal radial power factors and power generated in 38 flow channels. 36	
Table 4-5: Nominal axial power factors.....	38
Table 4-6: Nominal operational parameter values and ranges of uncertainty. ....	47
Table 4-7: Nominal manufactured values and ranges of uncertainty. ....	48
Table 5-1: MDNBR percentile values from 5000 samples. ....	72
Table 5-2: Maximum fuel temperature [K] percentile values from 5000 samples. ....	74
Table 5-3: Maximum clad temperatures [K] percentile values from 5000 samples. ..	76
Table 5-4: MDNBR sensitivity analysis results.....	83
Table 5-5: Maximum fuel temperature sensitivity analysis results. ....	84
Table 5-6: Maximum clad temperature sensitivity analysis results. ....	86
Table A-1: Cross flow path descriptions.....	105

# **Applying Uncertainty and Sensitivity on Thermal Hydraulic Subchannel Analysis for the Multi-Application Small Light Water Reactor**

## **1. INTRODUCTION**

Small modular reactors (SMRs) are a recent advancement in commercial nuclear reactor design with growing interest and development worldwide. Small modular reactors represent a shift in reactor design away from traditional large plants, with power production in excess of 1000 MW<sub>e</sub>; SMRs are defined as power plants that produce 300 MW<sub>e</sub> or less. This decreased power production allows deployment of SMRs toward a number of potential energy markets which would have otherwise been precluded through use of traditionally sized nuclear power plants (NPPs) [1]. Included within these potential new markets is the relative locale for deployment of SMRs throughout the world. Additional benefits of SMRs include potential for increased plant security and reactor safety, particularly when coupled with passive safety systems. Due to the modular design of SMRs, it is possible to construct offsite production facilities; resulting in a different supply chain than has historically been utilized within the nuclear power industry. This alternate supply chain model has significant potential to reduce fabrication cost and time. While there presently exists a diverse range of SMR concepts currently under development, the quickest designs from a licensing and deployment perspective utilize the light water reactor technology found in many NPPs operating today. One such SMR concept is the Multi-Application Small Light Water Reactor (MASLWR), developed by Idaho National Engineering and Environmental Laboratory, Oregon State University (OSU), and NEXANT [2]. The MASLWR design utilizes natural circulation under normal operation and features passive safety systems.

There are many challenges faced within the SMR community before any of the proposed concepts become commercially operational. One such challenge is the lack of historical operating experience. Due to the immense importance of nuclear reactor safety, previous operational experience is considered highly valuable. This is reflected

in current Nuclear Regulatory Commission (NRC) licensing requirements, which have been created upon the foundation of traditional NPPs that have been operating in the United States for a number of decades, with present efforts underway to update appropriate regulation for SMR concepts. One particular regulatory challenge, specific to the MASLWR design, is the utilization of natural circulation to provide cooling under normal operation. There are currently no licensed reactor designs in the United States designed for operation solely under natural circulation. Unlike forced circulation designs, where coolant flow through the reactor is controlled via pumps, flow in natural circulation is maintained through temperature and elevation differences between a heat source and heat sink. These attributes create a net difference in fluid density which results in buoyancy forces that drive natural circulation. The lack of forced convection yields coolant flow rates that are relatively lower than the traditional power plant design which in-turn requires a reduced power density within the core region in order to maintain appropriate safety margin(s). These traits present further challenges to the thermal hydraulic safety analysis of the MASLWR design, specifically to core subchannel analysis.

One tool with the potential to increase confidence in the results of thermal hydraulic analysis on the MASLWR design is that of uncertainty and sensitivity analysis. This type of analysis seeks to characterize the epistemic uncertainties associated with a mathematical system model. Epistemic uncertainty results from the inability to know an appropriate value for a quantity which otherwise assumed constant (e.g., instrumentation measurement uncertainty) [3]. Uncertainty analysis was introduced to the United States nuclear industry following changes made in 1988 to emergency core cooling system (ECCS) evaluation described in 10 CFR 50.46 [4]. These changes allowed the use of “best estimate” calculations with uncertainty analysis rather than the conservative 10 CFR 50 Appendix K methods which had been used until that time [4]. While uncertainty analysis was first introduced for ECCS calculations, the analysis methods themselves can be applied to any system model where epistemic uncertainty exists. Uncertainty analysis specifically seeks to characterize the total

uncertainty found in a system response, while sensitivity analysis seeks to identify how much influence each individual, independent parameter has on a system response.

### **Purpose**

One challenge of the MASLWR design includes the thermal hydraulic subchannel analysis which is operated under natural circulation. In subchannel analysis, thermal hydraulic calculations are performed on the reactor core to ensure that reactor safety limits are not exceeded. Previous subchannel calculations have been performed on the MASLWR core using VIPRE-01 [5]. The purpose of this study is to increase confidence in the outcomes of a subchannel analysis through uncertainty and sensitivity analysis relative to that of deterministic, conservative approach. This analysis is performed using the thermal hydraulic system code RELAP5-3D Version 4.0.3 and subchannel code VIPRE-01 Mod 2.2.1. Additionally, results from this work will provide further insight regarding each code's ability to model the MASLWR. This is considered especially important given the lack of SMR operational experience.

### **Objectives**

The objective of this study is to use the thermal hydraulic codes RELAP5-3D and VIPRE-01 to perform a subchannel analysis on the MASLWR under a prescribed set of operating conditions while performing a comprehensive uncertainty and sensitivity analysis. Both quantitative and qualitative comparisons of the results between RELAP5-3D and VIPRE-01 will be made. These objectives will be completed through the following tasks:

- Selection of existing uncertainty and sensitivity analysis methods which may easily be applied to both lumped parameter codes RELAP5-3D and VIPRE-01. Methods are selected based on their ability to accurately characterize nonlinear systems.
- A general subchannel analysis methodology is developed. This methodology accounts for modeling requirements in both RELAP5-3D and VIPRE-01. Independent input parameters are identified defined within the scope of this

study; these parameters are assigned a range of uncertainty with justification for their respective values.

- RELAP5-3D and VIPRE-01 models are created based on the methodology developed herein.
- A Fortran 90 program is developed to propagate uncertainty values through the RELAP5-3D and VIPRE-01 models. Additionally, this program extracts desired figures of merit from RELAP5-3D and VIPRE-01 and compiles this information appropriately.
- MATLAB is utilized to process all compiled data using the selected uncertainty and sensitivity analysis methods.
- Finally, a quantitative and qualitative comparison between results from RELAP5-3D and VIPRE is made.

In summary, this study performs a subchannel uncertainty and sensitivity analysis on the MASLWR using both the RELAP5-3D and VIPRE system models.

## 2. SURVEY OF LITERATURE

### **Overview of Uncertainty Analysis Methodologies**

Uncertainty analysis was introduced to the United States nuclear industry following changes made in 1988 to ECCS evaluation described in 10 CFR 50.46 [4]. Prior to this change, ECCS calculations were required to follow the conservative assumptions published in 10 CFR 50 Appendix K in 1974. Continuing loss-of-coolant-accident (LOCA) research showed the original conservative assumptions made in Appendix K were excessive [3]. To reflect this increased understanding, 10 CFR 50.46 was amended in 1988 to allow best-estimate methods with uncertainty quantification when evaluating ECCS performance.

#### *Code Scaling, Applicability, and Uncertainty*

In order to support the revised ECCS regulation, the NRC and its contractors and consultants developed an uncertainty analysis methodology called code scaling, applicability, and uncertainty (CSAU) [6]. The CSAU method provides general guidelines for quantifying code calculation uncertainty which are structured, auditable, and traceable. The CSAU method is separated into three major elements consisting of fourteen total steps.

The first element in the CSAU method is *requirements and code capabilities*. This element focuses on defining the problem and collecting required technical resources. To begin, a specific event scenario and plant type are selected. In step 3, phenomena specific to the scenario and plant type are captured through a phenomena ranking and identification table (PIRT). In steps 4 and 5, a frozen code version is selected and complete code documentation is provided. The first element ends with step 6, where qualitative comparisons of the identified phenomena and code documentation are made to assess the code's capability to analyze the selected scenario.

The second element is *assessment and ranging of parameters*. Step 7 establishes a code assessment matrix where applicable experiments are selected based on the important phenomena identified in step 3. Step 8 acknowledges the effect of code nodalization on uncertainty. An iterative process is used to compare experimental data with changing nodalization, and a final nodalization is selected as the standard for subsequent analysis. Step 9 evaluates code accuracy by comparing the selected experimental data with code calculated data. In step 10, the effect of test scale on uncertainty is evaluated.

The final element of the CSAU method is *sensitivity and uncertainty analysis*. Step 11 evaluates the effect of uncertainties in plant operating state. In steps 12 and 13, multiple code runs are executed to determine the sensitivity and uncertainty associated with individual parameters identified in steps 9-11. Finally, the total uncertainty is presented in step 14. The fourteen steps of the CSAU method are summarized in Figure 2-1.

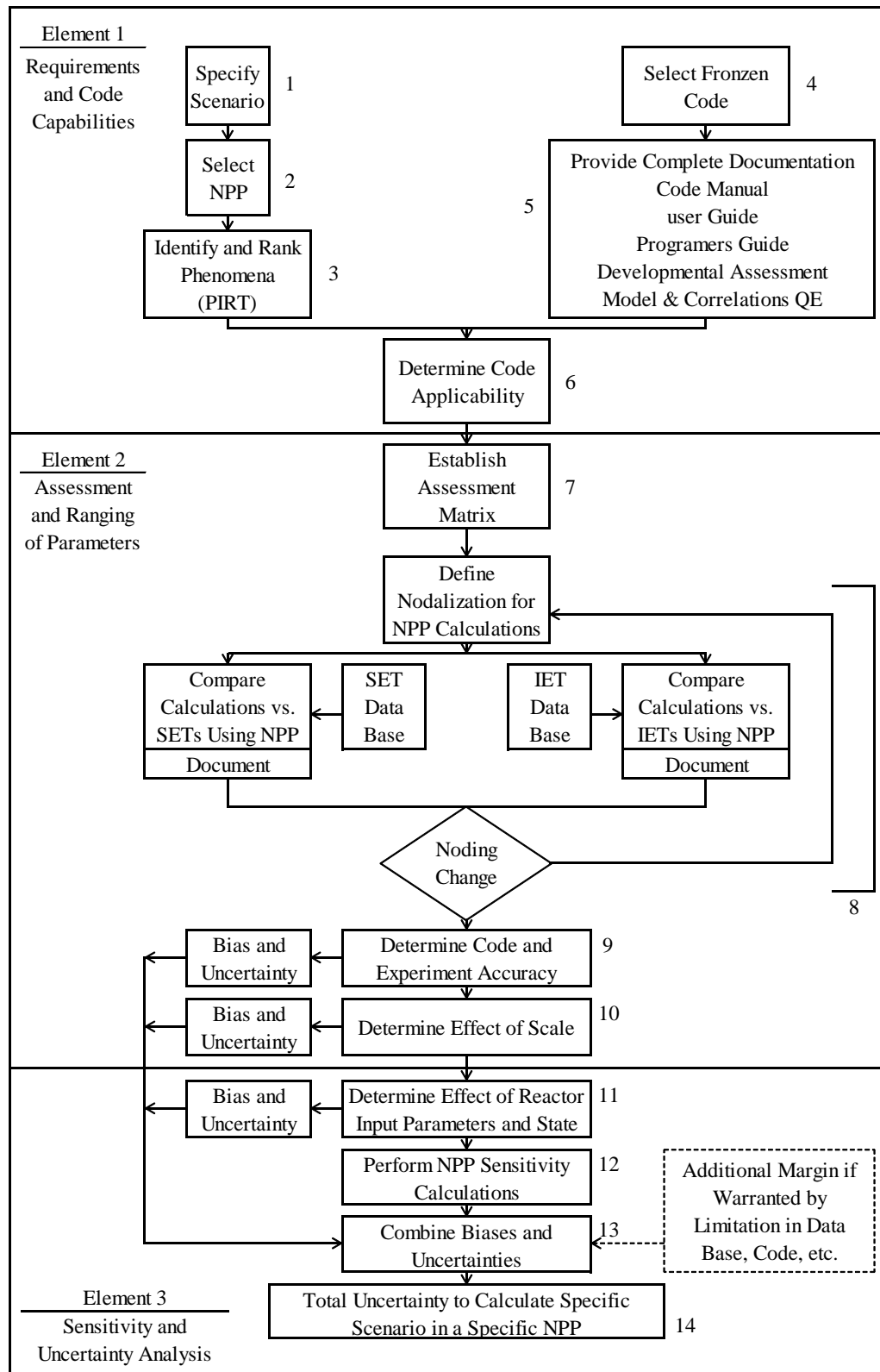


Figure 2-1: Fourteen steps of the CSAU methodology.

### *Response Surface*

The purpose of step 13 of the CSAU method is to combine the bias and uncertainty in the individual parameters which were identified as ‘important’ as a part of step 11. The original CSAU publication applied the response surface method for uncertainty quantification [6]. The response surface (RS) is a parametric method where the desired figure of merit (FOM) is described through a multinomial least-squares fit in terms of the selected important parameters [6]. This can be written generally as  $FOM = f(x_1, x_2, \dots, x_N)$ , where  $N$  is the number of parameters. Additional error, inherent to any parametric method, results from the difference between the response surface fit, i.e., the estimator, and the code calculation, i.e., the estimated. This error is quantified through the root-mean-square (RMS) error between the response surface fit and the calculated data [6]. Reduction of the RMS error is possible by applying higher order polynomials. However, doing so increases the required number of data points to generate the RS [6]. Additionally, larger values of  $N$  increase the number of unknown terms found in the response function. This also increases the required number of data points. Therefore, a trade-off exists between the RMS error, the number of selected parameters, and computational cost to generate the RS.

The final RS represents a simplified form of the full system model, where the complex thermal-hydraulic interactions have been reduced to a single polynomial expression. Monte Carlo sampling is performed on the RS to generate the probability distribution function (PDF) for the selected FOM [6]. Standard statistical processing may then be applied to determine the appropriate confidence levels necessary to demonstrate a comprehensive understanding of the system (i.e. 95 percent). NUREG/CR-5249 has suggested that taking 50,000 samples from the RS produces acceptable PDF results for the application of CSAU [6]. Generating these 50,000 samples is considered inexpensive relative to the computational cost of generating the actual RS from the full system model.

### *Wilks' Method*

While the RS method was demonstrated in the original CSAU publication, modern best-estimate methodologies have replaced the RS in favor of non-parametric methods [7,8]. Unlike parametric methods, non-parametric methods make no assumptions about the distribution shape of the desired FOM. As such, the number of required data samples is independent from the number of selected important parameters [8].

Wilks' method has become a common non-parametric method in recent best-estimate methodologies [9,10]. This method was originally presented in 1941 by S.S. Wilks for use in manufacture processes [11,12]. A set of equations was derived through which the number of required data samples can be solved for a desired tolerance limit and confidence level. The minimum number of data samples is found by Wilks' method at the first order. Equations for one-sided and two-sided tolerance limits are given as

$$1 - a^n \geq b \quad (2-1)$$

and

$$1 - a^n - n(1 - a)a^{n-1} \geq b \quad (2-2)$$

where  $a$  is the desired coverage,  $b$  is the confidence level, and  $n$  is the minimum number of required data samples [13]. Data sample requirements are presented in Table 2-1 for the one-sided and two-sided tolerance intervals.

Table 2-1: Number of data samples required for the first order Wilks' method.

	One-Side Limits			Two-Side Limits		
$b/a$	0.90	0.95	0.99	0.90	0.95	0.99
0.90	22	45	230	38	77	388
0.95	29	59	299	46	93	473
0.99	44	90	459	64	130	662

Examples demonstrating the application of Wilks' method includes AREVA's realistic large break LOCA analysis methodology [8]. This methodology, licensed by the NRC in 2003, follows the fourteen step process outlined by the CSAU method to provide a best-estimate LOCA evaluation. However, AREVA has opted to apply the Wilks'

method for uncertainty analysis rather than the original RS method. The non-parametric Wilks' method was selected as it decouples the number of uncertain parameters from the number of required calculations [8]. Another example which couples Wilks' method to CSAU is given in [14]. This report applies the modified CSAU method with Wilks' uncertainty to the feed-and-bleed transient analysis of the OSU Advanced Plant Experiment (APEX) facility. This shows the robustness of the CSAU method allows for applications beyond the original purpose of LOCA analysis.

An additional application of the Wilks' method is shown in [15]. In this report, the concept of the Quantified PIRT is introduced. To develop the Quantified PIRT, uncertainty analysis is performed using the Wilks' method in order to rank the importance of given phenomena associated with an event. The intended purpose of the Quantified PIRT is to assist the development of the traditional PIRT for code validation [15].

### **Statistical Analysis Using VIPRE-01**

Uncertainty and sensitivity analysis has been applied to VIPRE-01 to demonstrate a statistical core design methodology developed at Pennsylvania State University by Lloyd and Feltus [16]. The goal of this methodology, termed the Pennsylvania State Statistical Core Design Methodology (PSSCDM), was to develop a best-estimate departure from nucleate boiling (DNB) correlation. In short, sensitivity analysis is applied to determine which independent parameters should be included in the DNB correlation. Uncertainty is then calculated to determine the range of applicability for the correlation. The PSSCDM method was demonstrated to support reducing the conservative 1.3 DNB ratio (DNBR) safety limit found in the publicly available Westinghouse W-3 critical heat flux (CHF) correlation [24].

A one-eighth core model was developed using VIPER-01 which represents a typical 2703 MW pressurized water reactor (PWR) containing 17x17 Westinghouse fuel assemblies. The hot subchannel and surrounding subchannels were modeled at their

actual size and were located at the core center. Remaining channels were lumped into progressively larger regions as the distance from the core center increased. Sensitivity studies were made using the Electric Power Research Institute (EPRI) CHF correlation, specifically the EPRI-1 correlation used in VIPRE-01, to calculate DNBR [24]. Tested parameters included the following: system pressure, core inlet temperature, mass flux, power, grid loss coefficient, axial nodalization, radial nodalization, the flow field model, turbulent momentum mixing, and turbulent cross-flow mixing. Of these, pressure, inlet temperature, mass flux, power, and axial power shape were determined to have high significance on DNBR [16].

These five parameters were used to generate a new quadratic correlation for DNBR. To begin, each parameter was assigned a range of uncertainty. A software package, titled SAS/GRAPH, was then used to develop a series of response surfaces over the valid range of each parameter using VIPRE-01 results. Because the area of interest in the DNBR correlation is near 1.0, data points yielding a DNBR greater than 4.0 were removed to improve the quality of fit. For this same reason, Monte Carlo sampling of the input parameters was used to generate additional data points for use when generating the DNBR correlation.

Residuals between the PSSCDM DNBR correlation and VIPRE-01 calculated DNBR results were found to be normally distributed with a standard deviation of 3.89%. The EPRI-1 correlation, which was used to generate the PSSCDM correlation, has a reported standard deviation of 8.56%. The overall standard deviation in the PSSCDM correlation was calculated through root-mean-squares by

$$\sigma_{new} = \sqrt{\sigma_{EPRI}^2 + \sigma_{PSU}^2} \quad (2-3)$$

$$\sigma_{new} = \sqrt{0.0856^2 + 0.0389^2} \quad (2-4)$$

yielding a  $\sigma_{new}$  of 9.4%. A one-sided tolerance limit was calculated using

$$\bar{x} + K\sigma, \quad (2-5)$$

where  $\bar{x}$  is the sample mean,  $\sigma$  is the standard deviation, and  $K$  is a tabulated value for one-sided tolerance factors from Table 2 in [17]. At a 95/95 confidence level, the final one-sided limit was calculated as

$$1.0 + (1.874)(0.0940) = 1.18, \quad (2-6)$$

giving a new minimum DNBR safety limit of 1.18. It was concluded that the uncertainty and sensitivity analysis methods demonstrated in the PSSCDM could be applied to any plant specific DNBR correlation in order to gain more operational margin.

### **Natural Convection Subchannel Evaluation Using RELAP5-3D**

RELAP5-3D has been used to perform core thermal-hydraulic calculations on a small reactor cooled through natural circulation. This work was performed for the Oregon State TRIGA<sup>®</sup> Reactor (OSTR) to support safety analysis calculations as the OSTR underwent conversion from highly enriched uranium (HEU) to low enriched uranium (LEU) in 2008. After the fuel conversion was complete, Marcum et al. performed a comparative study between measured bulk coolant temperatures within the OSTR core and the theoretical predictions calculated by RELAP5-3D [18].

The OSTR is a 1.1 MW<sub>th</sub> open pool reactor which operates at atmospheric pressure and is cooled primarily through natural convection. The core is made from seven concentric rings of fuel pins with an overall diameter of 0.71 m and height of 0.66 m. MCNP5 was used to calculate the relative power in each fuel pin for the new LEU core. This also provided the location of the hottest fuel pin within the core.

Three RELAP5-3D models of the OSTR were developed: a one-channel model, a two-channel model, and an eight-channel model. Multiple models were developed to evaluate the effect the number of channels had on bulk coolant temperatures and the effects of crossflow. The one-channel model was used to represent the hot channel in the OSTR core (Figure 2-2). Time dependent volumes, used to model the coolant source and sink, provided system inlet and outlet boundary conditions. The cold leg

provided a pressure differential between the cold coolant at the core entrance and hot coolant at the core exit. This allows RELAP5-3D to model natural circulation flow. The hot fuel pin was modeled using a heat structure component which was thermally coupled to the hot channel.

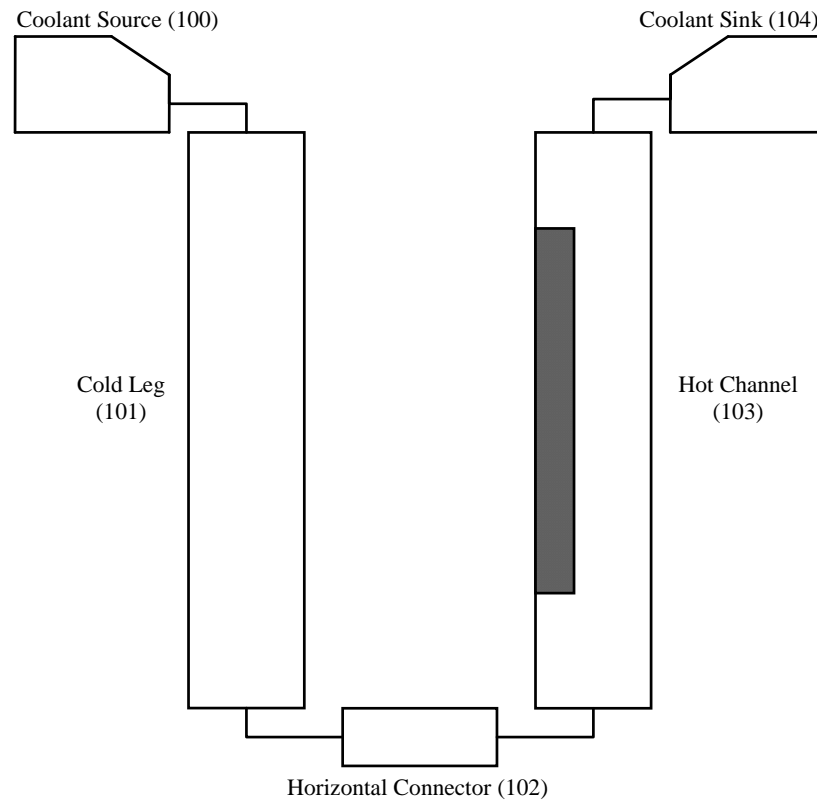


Figure 2-2: One-channel RELAP5-3D model used by Marcum et al. [18].

The two-channel model is similar to the one-channel model, with an addition flow volume adjacent to the hot channel. This second volume represents the remainder of the OSTR core channels lumped into a single volume. Junctions between the hot channel and lumped channel were made along the axial length of the core. These junctions allowed crossflow between the two volumes. The remaining OSTR fuel pins were lumped into a single representative heat structure. This component was thermally linked with the lumped channel volume. A similar method was used in the either-channel model. In this model, each of the seven rings of fuel pins were lumped into

their own volume. The hot channel remained separate from the other volumes. Crossflow junctions were made between the hot channel volume and the closest two rings.

A K-type thermocouple was used to measure bulk coolant temperature at various locations within the OSTR core, including the hot channel, at steady-state operating conditions. Comparisons were made between the three RELAP5-3D model results and the measured hot channel coolant temperature. It was shown that agreement between the RELAP5-3D results and experimental data improves as the number of modeled channels increases. Average coolant temperature errors between the one-, two-, and eight-channel models and the experimental data was 11.94%, 11.69%, and 8.78% respectively. An additional comparison was made between measured temperatures in an instrumented fuel element and RELAP5-3D predicted fuel temperatures. This comparison showed the one-, two-, and eight- channel models over predicted the measured fuel element temperature by 12.6°C, 12.6°C, and 12.5°C respectively. In all cases, RELAP5-3D gave conservative safety analysis results.

### **Closing**

In summary, a brief history of best-estimate calculations has been presented to provide insight into the current U.S. regulatory framework relating to uncertainty and sensitivity studies. The ability to employ different types of uncertainty analysis methodologies was shown, with the current trend leaning towards nonparametric methods. Additionally, it was shown that uncertainty analysis has broad applicability towards numerous different kinds of safety analyses. Finally, the application of RELAP5-3D for subchannel analysis was discussed to provide justification for its inclusion in this study. From these statements, it was determined that nonparametric uncertainty methods are suitable for the subchannel analysis of the MASLWR design. A detailed description of the MASLWR is subsequently given in Chapter 3.

### 3. MASLWR DESCRIPTION

The Multi-Application Small Light Water Reactor conceptual SMR design was developed by Oregon State University, Idaho National Engineering and Environmental Laboratory, and NEXANT [2]. Research for the MASLWR was funded by the U.S. Department of Energy's (DOE) Nuclear Energy Research Initiative (NERI) program. Initial design criteria for the MASLWR project included low cost, use of passive safety systems, shop fabrication through use of modularization, transportable by rail and road, 60 year plant life cycle, use of off-the-shelf components, and use of currently used industry components with some adaptation [2].

#### **MASLWR Design Overview**

The MASLWR is an integral PWR design which utilizes natural circulation during both steady-state operation and transient conditions [20]. The reactor pressure vessel (RPV) features an integrated helical coil steam generator (SG) located near the top of the hot leg riser. Primary coolant flowing over the SG tubes and generates steam inside the helical coils on the system's secondary side. Within the reactor pressure vessel, coolant buoyancy differences between the SG and the core produces the fluid body forces necessary to drive flow through the primary system during normal operation. The layout of the MASLWR design concept is shown in Figure 3-1. Primary system steady state operating conditions are given in Table 3-1.

Table 3-1: MASLWR steady-state operating conditions.

Parameter	Value	Reference
Reactor Thermal Power ( $\text{MW}_{\text{th}}$ )	150	[2]
System Pressure (MPa)	7.8	Table 4-1 of [2]
Primary Mass Flow Rate (kg/s)	596	Table 4-1 of [2]
Core Inlet Temperature (K)	491.8	Table 4-1 of [2]

The MASLWR design also features passive safety systems and does not require emergency pumps to maintain core coolability [19]. Instead, the RPV is closely

enclosed inside a cylindrical containment vessel which is partially filled with water [20]. This containment vessel is submerged in a pool of water which acts as the ultimate heat sink. Six valves connect the RPV to containment at different axial heights. These valves form the automatic depressurization system (ADS) and are opened in an emergency scenario. The outcome is a blowdown from the RPV into containment which reduces the primary system pressure. When pressure inside the RPV and containment equalize, the blowdown phase ends and a natural circulation loop is established [21]. Vapor from the core exits through ADS valves at the top of the RPV and then condenses inside containment. Liquid coolant flows downward and reenters the core through ADS valves at the bottom of the RPV. This natural circulation loop provides passive cooling by transferring thermal energy from the core to the ultimate heat sink [20].

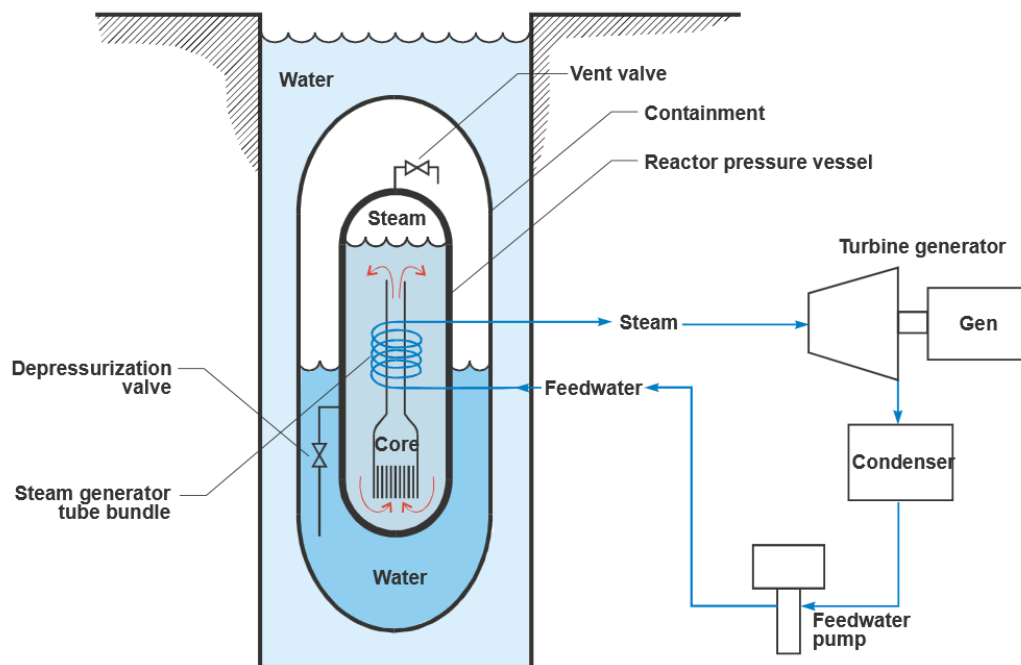


Figure 3-1: Layout of MASLWR components [2].

### MASLWR Core Geometry

The MASLWR module was designed to generate  $150 \text{ MW}_{\text{th}}$  or  $35 \text{ MW}_{\text{e}}$  assuming a 23 percent efficient cycle [2]. The MASLWR core has 24 assemblies arranged in a cylindrical configuration (Figure 3-2). Each assembly comprises a typical 17x17 PWR design with 264 fuel rods and 25 guide tubes of half length (Figure 3-3) [2].

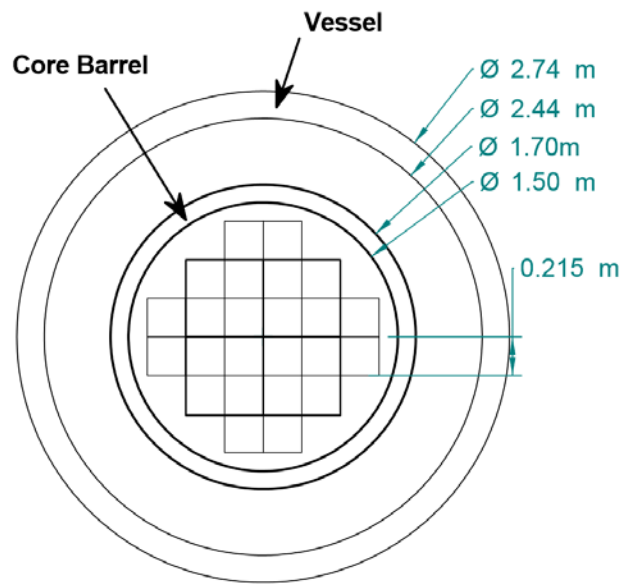


Figure 3-2: Schematic of the MASLWR prototypical core [2].

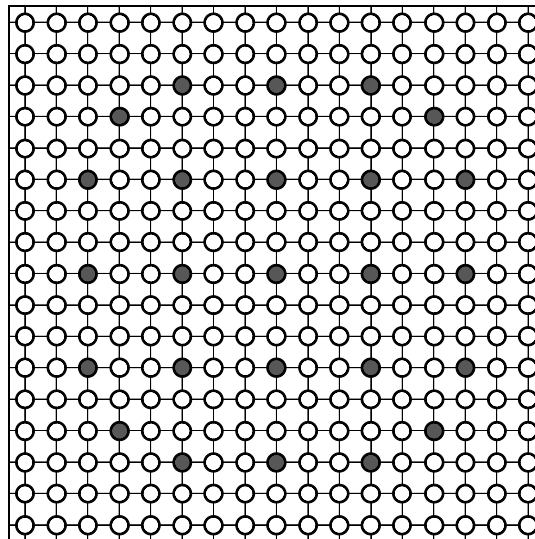


Figure 3-3: Diagram of a 17x17 assembly with guide tube locations.

A typical PWR fuel rod utilizes  $\text{UO}_2$  fuel pellets pressed inside zirconium tubes. Since the MASLWR uses light water as a moderator, the isotope U-235 must be enriched within the fuel. Previous studies have evaluated potential MASLWR core designs with the intended goal of a five year full power cycle [22]. These studies evaluated U-235 enrichments up to 8% in order to reach this goal. Core geometry for the MASLWR core is presented in Table 3-2. Additional studies relating to the MASLWR design can be found in [5], [19], and [23].

Table 3-2: Prototypical MASLWR core geometry [2,22]

Parameter	Value	Reference
Fuel Rod Lattice Arrangement (#)	17 x 17	[2]
Number of Guide Tubes (#)	25	[2]
Number of Fuel Rods (#)	264	[2]
Cladding OD (cm)	0.952	[2]
Cladding ID (cm)	0.838	[2]
Fuel Pellet OD (cm)	0.826	[2]
Fuel Rod Pitch (cm)	1.263	[2]
Guide Tube OD (cm)	1.22	[22]
Active Fuel Height (cm)	160.0	[22]

The MASLWR design descriptions presented in this chapter, particularly those summarized in Table 3-1 and Table 3-2, were used to develop a representative core model for use during subchannel analysis. The core model and associated calculation methodologies are presented in Chapter 4.

#### 4. METHODOLOGY

A model of the MASLWR prototypical core geometry was developed using two unique codes – RELAP5-3D Version 4.0.3 and VIPRE-01 Mod 2.2.1. A selection of uncertainty and sensitivity analysis methodologies has been applied to thermal hydraulic calculations performed with these models and is detailed herein. The MASLWR core models in RELAP5-3D and VIPRE-01 have been designed as similar as possible. The development of the model geometry and boundary condition inputs between the two codes are analogous to one another, unless explicitly detailed hereinafter. Therefore, it is assumed that any discrepancies found during uncertainty and sensitivity analysis result from differences between RELAP5-3D and VIPRE-01 themselves. This assumption is further explored in Chapter 5.

##### **MASLWR Core Model**

A simplified core model is built from the MASLWR prototypical core described in Chapter 3. A simplified model is desirable given the relatively large number of data samples required for uncertainty and sensitivity analysis. Based on the core design shown in Figure 3-2 being geometrically symmetric, one-quarter of the core is modeled (Figure 4-1), note that this is similar in model configuration to previous studies which have modeled the MASLWR core [5].

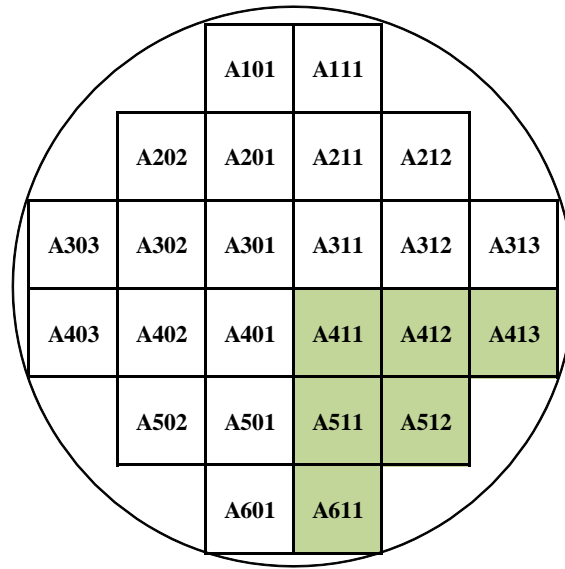


Figure 4-1: Assemblies used in the one-quarter model; numbering scheme from [5].

#### *Flow Channel Description*

Because the premise of this study supports the safety basis of the MASLWR design, it is desirable to clearly and comprehensively understand phenomenon which are characteristic within the most limiting conditions of the reactor core; that is, the location within the core which produces the most extreme fluid conditions, referred to hereinafter as the ‘hot channel’ (e.g. low flow in combination with high heat flux and equilibrium quality). A lumped channel approach is used to model axial flow paths through the core. In order to maintain relatively high geometric resolution of the hot channel, a five by five (5x5) subchannel section is defined with the hot channel located at the center. This 5x5 section is placed in assembly A411 shown in Figure 4-1. Because the radial power profile applied in this study takes a maximum value in the core center, the center assembly is considered a conservative location for the hot channel to reside. Subchannels surrounding this section are lumped into geometric volumes that increase in physical size as they increase in distance from the 5x5 section of interest. Based on recommendations from the VIPRE-01 user’s manual, channels are lumped such that the area increase is not greater than approximately one order of magnitude between adjacent volumes [26]. Assemblies A412, A413, A511, A512, and A611 from Figure 4-1 are modeled as single channels. In total, 38 flow channels are

modeled – 25 single subchannels channels and 13 lumped channels. The numbering scheme of these channels is shown in Figure 4-2, with channel 13 representing the hot channel.

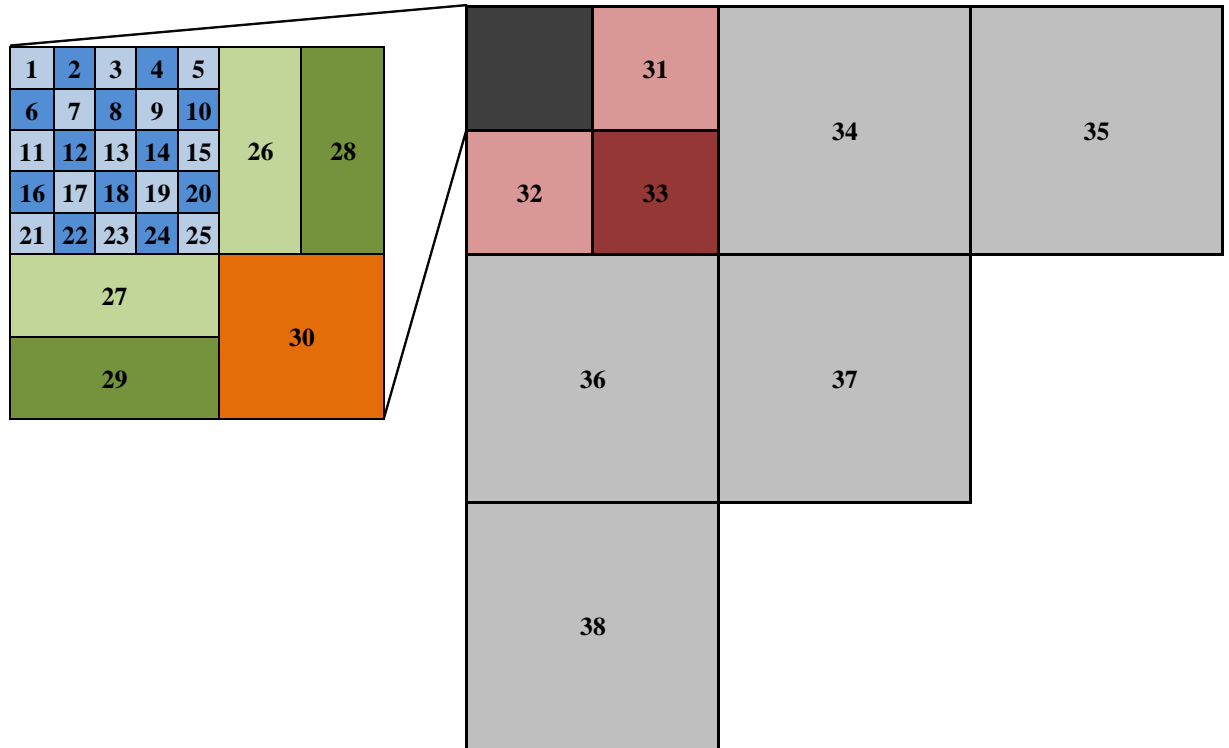


Figure 4-2: Channel numbering scheme in the one-quarter MASLWR core model.

Each of the 38 flow channels can be categorized into nine unique channel types based on common geometric traits, this is detailed further in Appendix A. Each type is defined in terms of a single subchannel unit-cell dimensions (Figure 4-3).

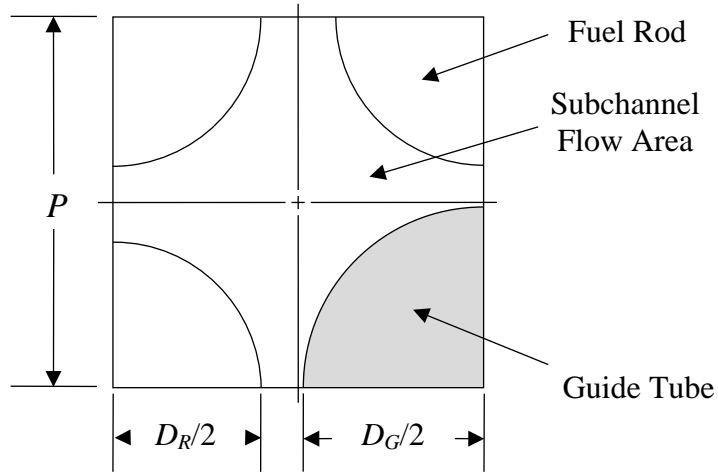


Figure 4-3: Square subchannel with guide tube unit dimensions.

Common geometry characteristics within each channel type include total fraction of a single subchannel ( $f_{sub}$ ), total fraction of fuel rods seen by the channel ( $f_R$ ), and total fraction of guide tubes seen by the channel ( $f_G$ ). Geometric parameters for each flow channel required by RELAP5-3D and VIPRE-01 include flow area ( $A$ ), wetted perimeter ( $P_{wet}$ ), heated perimeter ( $P_{heat}$ ), and hydraulic diameter ( $D_H$ ), which may be computed as

$$A = f_{sub} P^2 - \frac{\pi}{4} [f_R D_R^2 + f_G D_G^2], \quad (4-1)$$

$$P_{wet} = \pi [f_R D_R + f_G D_G], \quad (4-2)$$

$$P_{heat} = \pi f_R D_R, \quad (4-3)$$

and

$$D_H = \frac{4A}{P_{wet}}, \quad (4-4)$$

where  $P$  is the fuel rod pitch,  $D_R$  is the outside diameter of the fuel rod, and  $D_G$  is the outside diameter of the guide tube. A description of each channel type is given in Table 4-1. Equation (4-1) is solved for each channel type using nominal geometry dimensions presented in Table 3-2. Supplemental diagrams of each channel type are provided in Appendix A.

Table 4-1: Description of nine flow channel types.

Channel Type	Description	Channels	$f_{sub}$	$f_R$	$f_G$	Area (cm <sup>2</sup> )
1	Single subchannel at assembly corner.	1	0.25	0.25	0	2.205E-01
2	Single subchannel at assembly edge.	2, 3, 4, 5, 6, 11, 16, 21	0.5	0.5	0	4.410E-01
3	Subchannel with no guide tube.	7, 8, 9, 10, 12, 13, 14, 15, 17, 18, 22, 23	1	1	0	8.821E-01
4	Subchannel with guide tube.	19, 20, 24, 25	1	0.75	0.25	7.678E-01
5	2x5 lumped channel.	26, 27	9	8	1	7.482E+00
6	2x5 lumped channel.	28, 29	9	8.5	0.5	7.710E+00
7	4x4 lumped channel.	30	16	13.75	2.25	1.308E+01
8	One quarter of assembly.	31, 32, 33	72.25	66	6.25	6.087E+01
9	Full assembly.	34, 35, 36, 37, 38	289	264	25	2.435E+02

#### *Axial Flow Resistance*

In the absence of information detailing the MASLWR core flow inlet distribution, a uniform mass flux inlet condition is assumed on the underside of the lower grid plate. To eliminate bias caused by geometry driven flow redistribution resulting from a lumped channel model, a uniform axial flow resistance is defined for each channel. The hydraulic diameter of each flow channel is set to that of Channel Type 3. Solving

equations (4-3) and (4-4) using data from Table 3-1 and Table 4-1 gives a  $P_{wet}$  of 2.99 cm and a  $D_H$  of 1.18 cm. Additionally, the turbulent wall friction factor for each channel is calculated as

$$f = 0.32 \text{Re}^{-0.25}, \quad (4-5)$$

via the Blasius correlation [27], where Re is the local Reynolds number. Equation (4-5) is the default turbulent wall friction factor used in VIPRE-01 [25]. The Reynolds number for a single phase fluid in is defined by

$$\text{Re} = \frac{\rho V_m D_H}{\mu}, \quad (4-6)$$

where  $\rho$  is the fluid density,  $V_m$  is the mean (mass weighted) fluid velocity, and  $\mu$  is the fluid dynamic viscosity [27].

#### *Axial Nodalization*

The axial discretization of each flow channel and fuel rod follow the same nodalization scheme. Previous studies of the MASLWR core have been performed with an active fuel length of 160 cm [5,22]. The active fuel is subdivided into 20 axial segments 8 cm in length. A reflector segment of 8 cm comprising of depleted uranium is included at the top and bottom of the fuel rod [22]. In total, a modeled fuel rod is 176 cm in length with 22 axial volumes and 23 axial nodes (Figure 4-4).

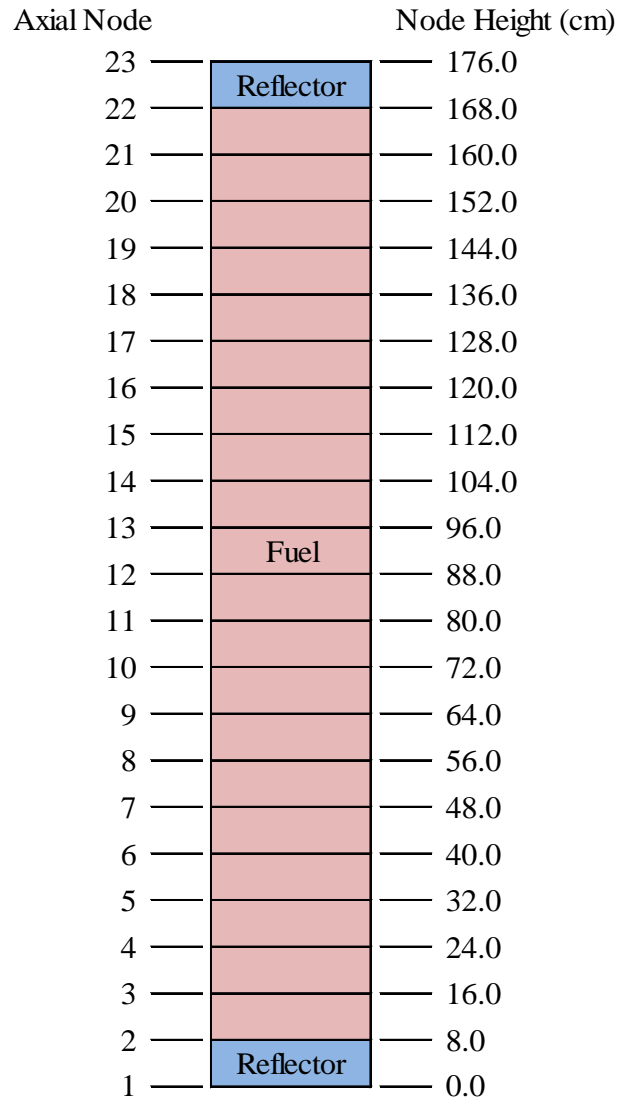


Figure 4-4: Axial nodalization of fuel rod.

In a typical PWR design, grid spacers are placed axially along the fuel assembly in order to restrain lateral motion of the fuel rods. The presence of grid spacers causes irrecoverable pressure losses along the axial flow direction [27]. This pressure loss can be calculated by

$$\Delta p = K \frac{G^2}{2\rho_{avg}}, \quad (4-7)$$

where  $K$  is the grid spacer form loss coefficient and  $G$  is the undisturbed mass flux in the axial direction [27]. These pressure losses are included within the model development of this study so as to provide a representative response to the system that is likely to occur in the prototype design. Grid spacer modeling is adopted from previous thermal hydraulic studies of the MASLWR core [5]. This model places five grid spacers in the fuel assembly with spacing of 40 cm (Table 4-2). A nominal grid spacer loss coefficient of 0.86 is assumed [5].

Table 4-2: Grid spacer location in fuel assembly.

Grid Spacer	Located at Axial Node	Height (cm)
5	22	168.0
4	17	128.0
3	12	88.0
2	7	48.0
1	2	8.0

#### *Channel Cross Flow Description*

Due to the open geometry in a PWR fuel assembly, it is possible for coolant to flow between adjacent subchannels through gaps between the fuel rods. This transverse fluid movement, or "cross flow", exchanges both fluid mass and energy between adjacent flow channels. In order to accurately model cross flow, a description of each cross flow path must be made in RELAP5-3D and VIPRE-01. Cross flow paths are modeled between individual axial volumes of adjacent flow channels. Figure 4-5 shows a cross flow path between two square subchannels. Required geometric parameters include gap width, centroid distance, cross flow area, and hydraulic diameter.

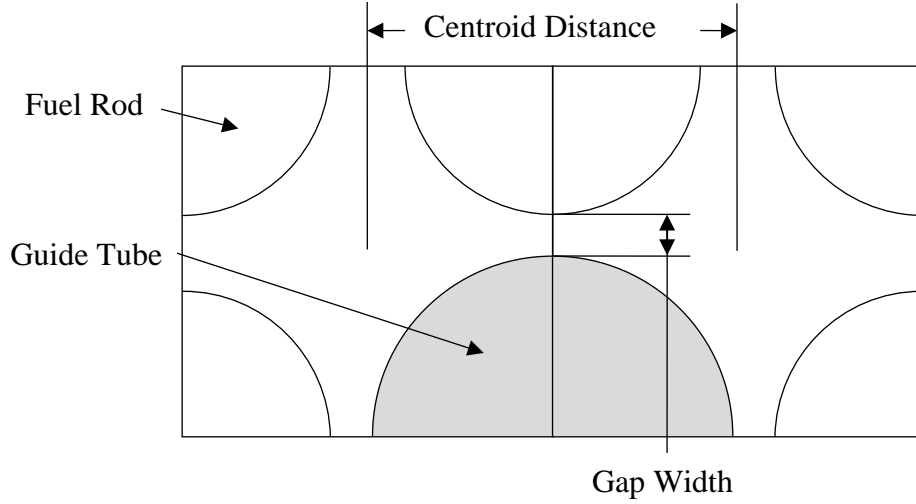


Figure 4-5: Cross flow path between square subchannels with guide tube.

Gap width ( $L_G$ ) is the minimum lateral distance between fuel rods and or guide tubes at the connecting edge of two adjacent flow channels. If two flow channels join at the center of a subchannel (e.g., a connection between channels in adjoining assemblies), then the gap width should be calculated as if fuel rods and or guide tubes still resided on the connecting edge [26]. A generalized equation for gap width is developed as

$$L_G = f_P P - f_R D_R - f_G D_G, \quad (4-8)$$

where  $f_P$  is the total fraction of fuel rod pitch  $P$ ,  $f_R$  is the total fraction of fuel rod diameter  $D_R$ , and  $f_G$  is the total fraction of guide tube diameter  $D_G$ . All of these parameters are defined along the connecting edge.

Centroid distance is the length between the geometric centers of two adjacent flow channels [26]. For channels with symmetric boundaries (e.g., channels on the corner or edge of an assembly) where the channel is divided by a line of symmetry, centroid distance is calculated assuming a complete channel geometry [26]. A generalized equation for centroid distance is developed as

$$L_C = \sqrt{P^2 (f_H^2 + f_V^2)}, \quad (4-9)$$

where  $f_H$  and  $f_V$  are the fraction of pitch lengths spanning the horizontal and vertical distances between the geometric centers of the adjacent flow channels.

Cross flow area is the cross sectional area through which coolant can flow between adjacent channels at each axial volume. This area is defined as

$$A_c = L_G L_{volume}, \quad (4-10)$$

where  $L_{volume}$  is the length of each axial volume. The wetted perimeter of a cross flow connection is

$$P_{c,wet} = 2(L_G + L_{volume}). \quad (4-11)$$

Hydraulic diameter is found by substituting equations (4-10) and (4-11) into equation (4-4). A total of 70 cross flow paths are represented in the MASLWR core model. A detailed call-out of these paths is given in Table A-1 of Appendix A.

In addition to these geometric parameters, each cross flow path has an associated lateral flow resistance. This resistance results from frictional drag as coolant flows through gaps between adjacent fuel rods. This lateral flow resistance is explicitly defined as a form loss for each cross flow path to increase modeling similarity between RELAP5-3D and VIPRE-01. For a flow path between adjacent subchannels, a recommended lateral flow resistance is assumed as  $K_G = 0.5$  [26]. When subchannels are lumped together, the lateral flow resistance is the sum of the resistances of the rod rows between the channel centers [26]. Lateral flow resistance between lumped channels is expressed as

$$K_i = N_i K_G. \quad (4-12)$$

where  $N_i$  is the number of rod rows between channel centroids at connection  $i$  [26].

$N_i$  is defined as

$$N_i = \frac{L_{C,i}}{P}, \quad (4-13)$$

where  $L_{C,i}$  is the centroid distance of connection  $i$  and  $P$  is the fuel rod pitch. Flow resistance,  $K_i$ , for each cross flow path is included in Table A-1 of Appendix A.

### *Nuclear Fuel Rod*

In a typical PWR fuel rod,  $\text{UO}_2$  sintered fuel pellets are placed inside a cylindrical zirconium tube, referred to as cladding. Surface roughness on the  $\text{UO}_2$  fuel pellet creates a gap at the inner clad and outer pellet interface. After the fuel is irradiated during operation, this gap fills with fission product gases released during operation, creating a region of high thermal resistance between the fuel pellet and the clad. The understanding and inclusion of appropriate thermal resistance within the fuel is an important attribute to include within a subchannel model when considering a reactor's safety basis; gap thermal resistance is further discussed in the following subsection.

Thermal energy is generated during fission that occurs within the  $\text{UO}_2$  fuel. This thermal energy is transferred to the coolant by way of the fuel pellet, gap, and cladding. The RELAP5-3D and VIPRE-01 models assume this energy transfer occurs only in the radial direction (i.e. there is no axial conductance within a fuel rod). The nuclear fuel rod is modeled as the radial path from the fuel centerline to the outer clad surface. This radial path is discretized into 12 volumes with 13 nodes: volumes 1-10 represent the fuel pellet, volume 11 represents the gap, and volume 12 represents the clad (Figure 4-6). It is assumed that the radial power profile within the fuel pellet is flat (i.e., equal in power density within each fuel volume). Within a physical nuclear reactor fuel rod, the radial power profile is represented by an approximate quadratic shape, increasing in power as radial position increases with the maximum power occurring at the outer edge of the fuel pellet. However, there are presently no available literary works that have been produced for the MASLWR design which detail this radial fuel pellet power distribution, therefore it is assumed to be most appropriate to remove ambiguity and assumptions in shape from this study's input, and maintain a uniform profile between both RELAP5-3D and VIPRE-01 models. Nominal geometry, calculated from data provided in Table 3-2, is presented in Table 4-3.

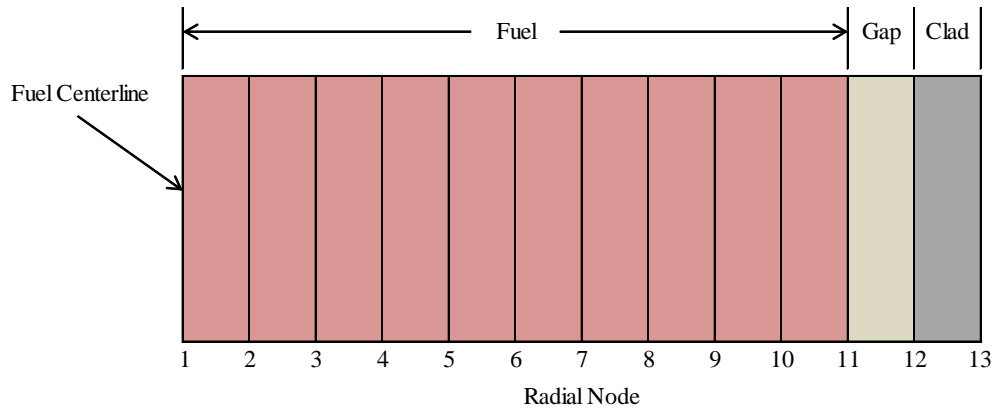


Figure 4-6: Radial discretization of a nuclear fuel rod.

Table 4-3: Radial geometry of a nuclear fuel rod.

Radial Node	Distance from Centerline (cm)	Radial Volume	Width (cm)
13	0.4761	-	-
12	0.4190	12	0.0571
11	0.4130	11	0.0060
10	0.3717	10	0.0413
9	0.3304	9	0.0413
8	0.2891	8	0.0413
7	0.2478	7	0.0413
6	0.2065	6	0.0413
5	0.1652	5	0.0413
4	0.1239	4	0.0413
3	0.0826	3	0.0413
2	0.0413	2	0.0413
1	0.0000	1	0.0413

Thermal conductivities for the  $\text{UO}_2$  fuel and zirconium cladding are manually entered into the RELAP5-3D and VIPRE-01 models in order to reduce bias in calculated fuel rod temperatures. The temperature effect on thermal conductivity is ignored. The thermal conductivity for the  $\text{UO}_2$  fuel is assumed as 3.6 W/m-K. This is the average conductivity of  $\text{UO}_2$  between 200°C and 1000°C [27]. The thermal conductivity of the

cladding is assumed as 14.0 W/m-K. This is the MATPRO predicted thermal conductivity of Zircaloy at 500°C [30].

### *Fuel Rod Gap*

To reduce bias in the calculated fuel rod temperatures, the thermal conductivity of the gap region between the fuel pellet and cladding is manually entered into RELAP5-3D and VIPRE-01. This value is assumed as 0.28 W/m-K, which is the MATPRO conductivity through helium gas at 700°C [30]. RELAP5-3D uses the specified thermal conductivity and the geometry data described in the previous subsection to calculate the total heat transfer through the gap. However rather than thermal conductivity, VIPRE-01 requires that the total conductance through the gap be specified.

A relation must be derived to relate gap conductivity to gap conductance. This correlation begins with the one dimensional form of Fourier's Law, which is written for cylindrical geometry in the radial direction as

$$\frac{q_r}{A_r} = -k \frac{dT}{dr}, \quad (4-14)$$

where  $q_r$  is heat transferred in the radial direction,  $A_r$  is the surface area at radius  $r$ ,  $k$  is the thermal conductivity, and  $T$  is the material temperature. Equation (4-14) is rewritten in the form

$$\int_{r_1}^{r_2} \frac{q_r}{2\pi L r} dr = \int_{T_1}^{T_2} -k dT, \quad (4-15)$$

where  $r_1$  is outer radius of the fuel pellet and  $r_2$  is the inner radius of the cladding. Integrating equation (4-15) gives

$$\frac{q_r}{2\pi L} \ln\left(\frac{r_2}{r_1}\right) = k \Delta T. \quad (4-16)$$

Next, the heat transfer coefficient is introduced as

$$\frac{q_r}{A_r} = h \Delta T, \quad (4-17)$$

where  $h$  represents the conductance through the gap. Equation (4-17) is rewritten as

$$q_r = 2\pi L r_{avg} h \Delta T , \quad (4-18)$$

where  $r_{avg}$  is the average gap radius. Equation (4-18) is now substituted into equation (4-16) to give

$$r_{avg} h \ln\left(\frac{r_2}{r_1}\right) = k . \quad (4-19)$$

Finally, equation (4-19) is written to solve for  $h$

$$h = \frac{k}{r_{avg} \ln\left(\frac{r_2}{r_1}\right)} . \quad (4-20)$$

Inputting the appropriate geometric values and thermal conductivity into equation (4-20) yields an equivalent VIPRE-01 gap conductance of 46.7 W/m<sup>2</sup>-K. A test case was performed to verify that this modeling does not introduce any bias into the RELAP5-3D and VIPRE-01 results. While keeping all other inputs at their nominal value, 100 calculations are performed in RELAP5-3D and VIPRE-01 with gap thicknesses varying from 6.0E-6 cm to 0.012 cm. Temperature profiles for fuel centerline temperature, outer fuel pellet temperature, inner clad temperature, and surface clad temperature are plotted versus gap thickness in Figure 4-7. As can be seen from Figure 4-7, the temperatures predicted by RELAP5-3D and VIPRE-01 have very close agreement. It is concluded that equation (4-20) is a valid method to calculate gap conductance without biasing the temperature results.

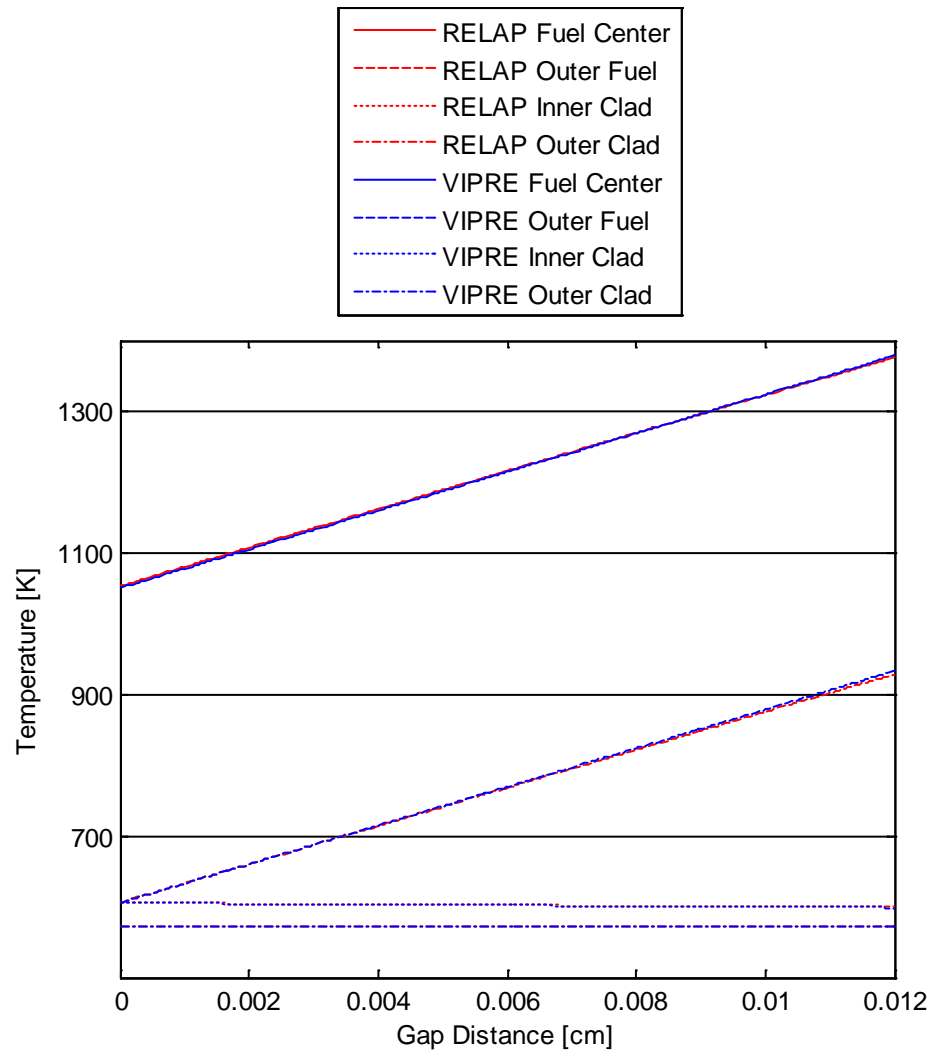


Figure 4-7: Fuel temperature profiles with changing gap thickness.

### *Core Power Distribution*

Power generation within a nuclear core is not uniform. Instead, it is a function of fuel enrichments, burnable poisons, local coolant properties, control rods, etc. Therefore, local power generation within each fuel rod should be specified. General power shapes are created assuming a homogenous, unreflected cylindrical core. For this core type and study, it is assumed that radial power follows a zero order Bessel function of the

first kind and axial power follows a chopped cosine [27]. Radial and axial power shapes, ignoring extrapolation lengths, are defined as

$$\phi_R(r) = J_0\left(\frac{2.4048 r}{R}\right), \quad (4-21)$$

$$\phi_Z(z) = \cos\left(\frac{\pi z}{L}\right), \quad (4-22)$$

where  $r$  is the radial distance from the center of the core,  $R$  is the radius of the core,  $z$  is the vertical distance from the axial centerline, and  $L$  is the active fuel length. In this model,  $R$  is taken as the width of three assemblies, 64.4 cm, and  $L$  is 160.0 cm.

A lumped rod approach is used when modeling fuel rods in the MASLWR core. With this approach, power generation in each flow channel is represented by a single fuel rod. Each flow channel will have a single corresponding radial and axial power factor, defined by

$$F_{R,i} = \frac{P_{R,i}}{P_{R,avg}} \quad (4-23)$$

and

$$F_{Z,i} = \frac{P_{Z,i}}{P_{Z,avg}}, \quad (4-24)$$

where  $P_R$  is the power generated in a rod and  $P_{R,avg}$  is the core average rod power generation. Similarly for a specific rod,  $P_Z$  is the power generated within an axial volume and  $P_{Z,avg}$  is the rod average axial volume power generation.

By definition, channel 13 will have the highest radial power factor in the core in order to be the hot channel. Radial power in all other channels is found using equation (4-21) where  $r$  is the distance from the geometric center of channel 13 to the geometric center of the channel. Once  $\phi_R$  for each channel is assigned, the factors are normalized such that the average radial power factor is one.

In order to control the final radial factor of the hot channel, the radial power shape  $\phi_R$  is first vertically translated by the value

$$t_R = \frac{\phi_R(r_{hot}) \sum_{i=1}^N f_{r,i} - F_{hot} \sum_{i=1}^N (\phi_R(r_i) f_{r,i})}{\left( \sum_{i=1}^N f_{r,i} \right) (F_{hot} - 1.0)}, \quad (4-25)$$

where  $N$  equals 38 channels,  $r_{hot}$  equals 0.0 cm,  $f_r$  is the total fraction of fuel rods seen by channel  $i$ , and  $F_{hot}$  is the desired radial power factor in the hot channel. Equation (4-25) is added to equation (4-21) to give

$$\phi_{R,new}(r) = \phi_R(r) + t_R. \quad (4-26)$$

The radial power factor in each channel is now calculated by

$$F_R = w_R \phi_{R,new}(r), \quad (4-27)$$

where

$$w_R = \frac{\sum_{i=1}^N f_{r,i}}{\sum_{i=1}^N (\phi_{R,new}(r_i) f_{r,i})}. \quad (4-28)$$

The total power generated in a channel can now be calculated by

$$P_R = P_{R,avg} F_R f_r. \quad (4-29)$$

A nominal hot channel radial power factor of 1.15 is assumed (Table 4-6). Table 4-4 shows the nominal radial power for all 38 channels. Core radial power shapes are shown in Figure 4-8 using equation (4-27) with hot channel power factors of 1.05, 1.15, and 1.25.

Table 4-4: Nominal radial power factors and power generated in 38 flow channels.

Flow Channel	Radial Distance from Hot Channel (cm)	$f_r$	$F_R$	Power Generated (kW)
1	3.571	0.25	1.1485	6.797
2	2.823	0.50	1.1490	13.601
3	2.525	0.50	1.1492	13.604
4	2.823	0.50	1.1490	13.601
5	3.571	0.50	1.1485	13.595
6	2.823	0.50	1.1490	13.601
7	1.786	1.00	1.1496	27.216
8	1.263	1.00	1.1498	27.221
9	1.786	1.00	1.1496	27.216
10	2.823	1.00	1.1490	27.203
11	2.525	0.50	1.1492	13.604
12	1.263	1.00	1.1498	27.221
13	0.000	1.00	1.1500	27.225
14	1.263	1.00	1.1498	27.221
15	2.525	1.00	1.1492	27.207
16	2.823	0.50	1.1490	13.601
17	1.786	1.00	1.1496	27.216
18	1.263	1.00	1.1498	27.221
19	1.786	0.75	1.1496	20.412
20	2.823	0.75	1.1490	20.402
21	3.571	0.50	1.1485	13.595
22	2.823	1.00	1.1490	27.203
23	2.525	1.00	1.1492	27.207
24	2.823	0.75	1.1490	20.402
25	3.571	0.75	1.1485	20.392
26	4.464	8.00	1.1476	217.350
27	4.464	8.00	1.1476	217.350
28	6.973	8.50	1.1442	230.245
29	6.973	8.50	1.1442	230.245
30	8.035	13.75	1.1423	371.838
31	14.116	66.00	1.1265	1760.111
32	14.116	66.00	1.1265	1760.111
33	19.641	66.00	1.1052	1726.851
34	30.177	264.00	1.0490	6556.078
35	51.166	264.00	0.9004	5627.244
36	30.177	264.00	1.0490	6556.078
37	41.068	264.00	0.9753	6095.470
38	51.166	264.00	0.9004	5627.244

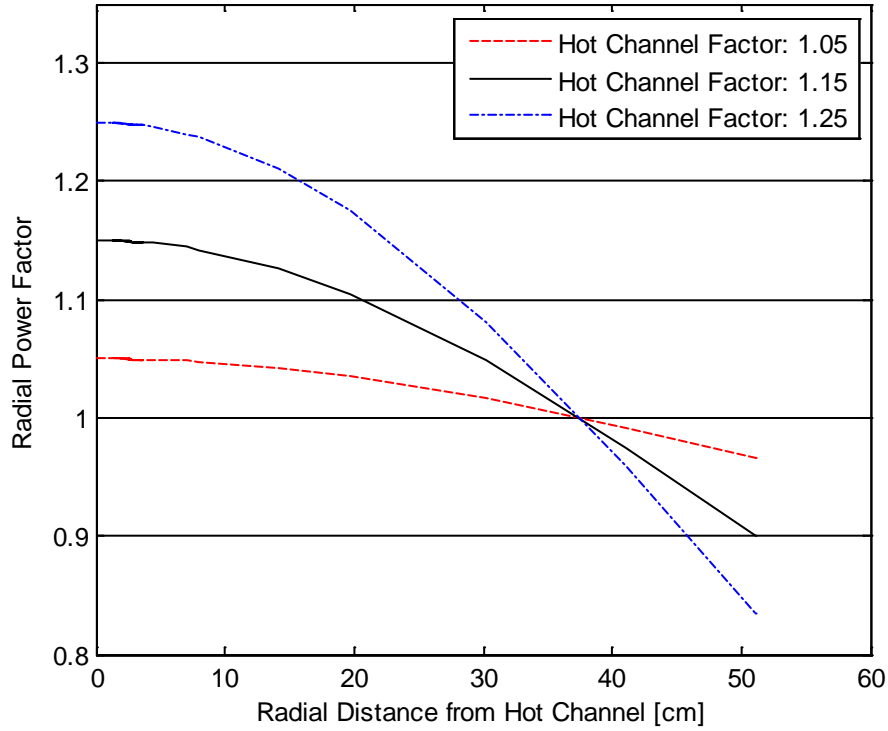


Figure 4-8: Effect of hot channel factor on overall radial factor profile.

Power generation within each flow channel is also divided between axial volumes. Axial power factors are found by modifying equations (4-25), (4-26), (4-27), and (4-28) to give

$$t_z = \frac{\phi_Z(z_{center}) \sum_{i=1}^N f_{z,i} - F_{center} \sum_{i=1}^N (\phi_Z(z_i) f_{z,i})}{\left( \sum_{i=1}^N f_{z,i} \right) (F_{center} - 1.0)}, \quad (4-30)$$

$$\phi_{Z,new}(z) = \phi_Z(z) + t_z \quad (4-31)$$

$$F_Z = w_z \phi_{Z,new}(z) \quad (4-32)$$

and

$$w_z = \frac{\sum_{i=1}^N f_{z,i}}{\sum_{i=1}^N (\phi_{Z,new}(z_i) f_{z,i})}. \quad (4-33)$$

Here  $\phi_Z(z_{center})$  is the axial power factor in the axial volume closes to the centerline calculated using equation (4-22) and  $F_{center}$  is the desired peak axial power factor. Because power is weighted equally in all axial volumes,  $f_z$  equals 1.0. The nominal peak axial power factor is 1.19 (Table 4-6). Nominal axial power factors are presented in Table 4-5. The total power generated within an axial volume is defined by

$$P_Z = \frac{P_{R,avg} F_R f_r F_Z}{20}. \quad (4-34)$$

Table 4-5: Nominal axial power factors.

Axial Volume	Vertical Distance from Axial Centerline (cm)	$F_Z$
21	76.0	0.7048
20	68.0	0.7867
19	60.0	0.8655
18	52.0	0.9394
17	44.0	1.0064
16	36.0	1.0651
15	28.0	1.1138
14	20.0	1.1514
13	12.0	1.1770
12	4.0	1.1900
11	-4.0	1.1900
10	-12.0	1.1770
9	-20.0	1.1514
8	-28.0	1.1138
7	-36.0	1.0651
6	-44.0	1.0064
5	-52.0	0.9394
4	-60.0	0.8655
3	-68.0	0.7867
2	-76.0	0.7048

### **RELAP5-3D Model**

A RELAP5-3D Version 4.0.3 MASLWR core model has been developed based on the methodology described in the previous section. RELAP5-3D is a thermal hydraulic system analysis code developed at Idaho National Laboratory. RELAP5-3D was developed for light water reactor (LWR) transient analyses including LOCAs, anticipated transients without scram (ATWS), and other operational transients [31]. RELAP5-3D is a finite volume code which employs a nonhomogeneous and non-equilibrium model for two-phase flow using a partially implicit solution scheme [31].

To build a RELAP5-3D model, a series of hydraulic components are defined to build the overall flow path, e.g., flow through the MASLWR core subchannels. Separate heat structure components are used to model heat transfer through the fuel rods. A representative RELAP5-3D model is shown in Figure 4-9. Each case is run in transient mode for 50 seconds for the solution to converge to steady state.

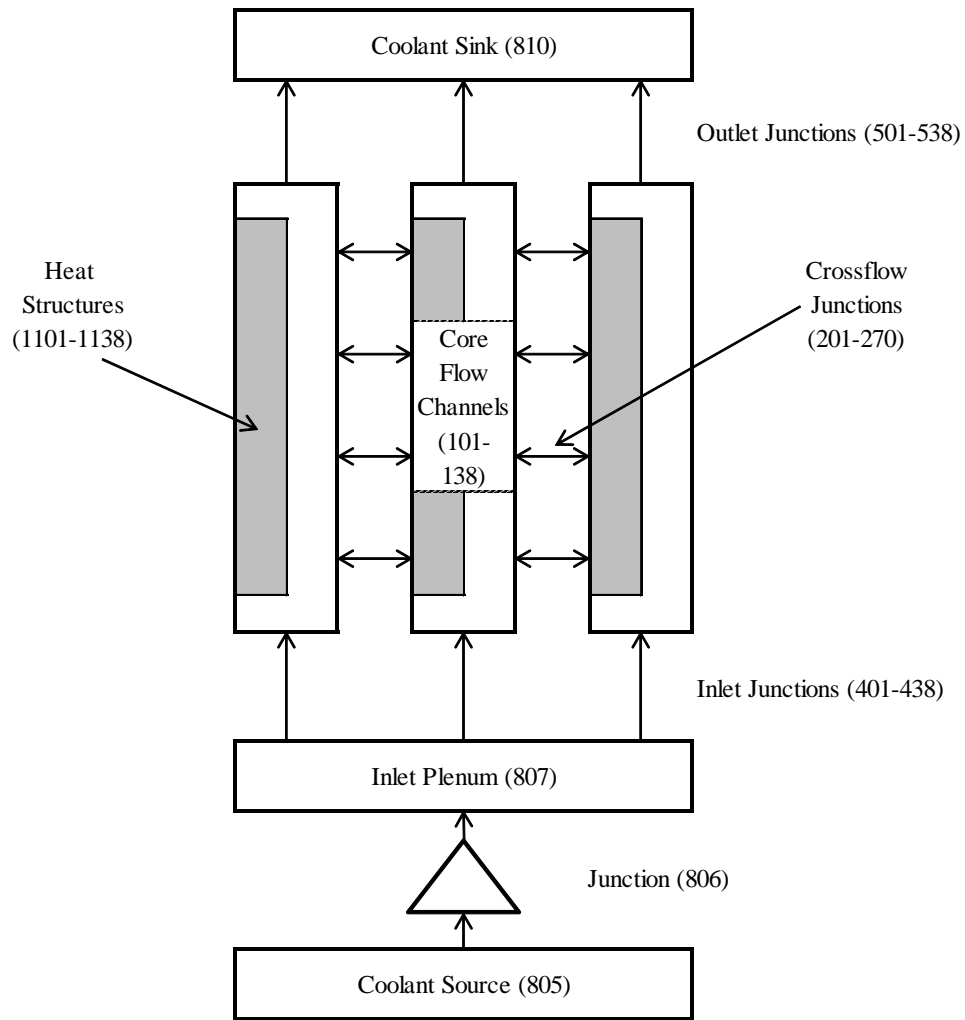


Figure 4-9: RELAP5-3D system model.

#### *Coolant Source (805)*

A coolant source is required in the RELAP5-3D model to provide inlet boundary conditions to the system. The source is modeled as a time dependent control volume with an area equal to the sum of all core flow channel areas, or  $1406.9 \text{ cm}^2$ . This component provides a source for coolant mass and the core inlet temperature to the system (Table 4-6).

### *Coolant Source to Inlet Plenum Junctions (806)*

This component connects the coolant source to the core inlet plenum. A time dependent junction is used to provide the total system flow rate (Table 4-6). An area of  $1406.9 \text{ cm}^2$  is used.

### *Inlet Plenum (807)*

The inlet plenum is an unrealistic volume in the MASLWR model required by RELAP5-3D in order to distribute total system flow to each core flow channel. The plenum is modeled with a frictionless branch component with an area of  $1406.9 \text{ cm}^2$  and height of 8 cm.

### *Inlet Plenum to Core Flow Channel Junctions (401-438)*

These junctions allow coolant to flow from the inlet plenum into each core flow channel. Each junction is given an area equal to the area of its corresponding flow channel (Table 4-1).

### *Core Flow Channels (101-138)*

Core flow channels are modeled using 38 individual pipe components within RELAP5-3D. Geometry and nodalization of these components is discussed in the previous section. Included within each pipe component is the grid spacer form loss. This is modeled as the forward/reverse loss coefficient at the corresponding internal pipe junctions (Table 4-2). Additionally, pipe wall friction is disabled in the transverse direction for every pipe volume. This ensures transverse crossflow resistance between channels is defined only by the crossflow form loss factors.

### *Core Crossflow Junctions (201-270)*

Crossflow paths are modeled using the multiple junction component within RELAP5-3D. These paths allow transverse flow between every adjacent channel at each axial volume within the core. The geometry of these junctions is described in Table A-1. Following recommendations given in the RELAP5-3D user manual, momentum flux for all crossflow junctions is disabled [32]. Additionally, crossflow is disabled at the

top of the core, axial volume 22, in order to prevent artificial recirculation. Removing this crossflow path has a negligible impact on downstream behavior in the core.

#### *Core Heat Structures (1101-1138)*

Fuel rods are modeled using heat structure components within RELAP5-3D. These components model nuclear heat generation and heat transfer through the fuel rod into the coolant. Geometry, physical properties, and power generation within these components are discussed the previous section. At steady-state conditions, heat flux from the fuel rods to the coolant is independent from the rod internal composition. Therefore, in order to reduce computation time, only the core hot rod (heat structure 1113) uses the full nuclear fuel rod geometry. The remaining rods are modeled as solid zirconium cylinders using the same outside diameter. Power generation within these cylinders is identical to that of the nuclear fuel rods they replace.

#### *Core Flow Channels to Coolant Sink Junctions (501-538)*

These junctions allow coolant transfer from the core flow channels to the system coolant sink. Each junction is given an area equal to the area of its corresponding flow channel (Table 4-1). Momentum flux at these junctions is disabled to prevent artificial recirculation. For this same reason, a large reverse flow form loss is also applied. These modeling changes have a negligible impact on downstream flow. Because momentum flux is disabled at these junctions, an upper plenum component is not required. Instead, flow channels are connected directly to the coolant sink.

#### *Coolant Sink (810)*

A coolant sink is required in the RELAP5-3D model to provide outlet boundary conditions to the system. The sink is modeled as a time dependent control volume with an area of  $1406.9 \text{ cm}^2$ . Additionally, this component provides the core exit pressure to the system (Table 4-6).

## **VIPRE Model**

A VIPRE-01 Mod 2.2.1 MASLWR core model has been developed based on the methodology previously described. VIPRE-01 is a thermal hydraulic subchannel analysis code originally developed by Battelle Pacific Northwest Laboratories for the EPRI in 1984 [24]. VIPRE-01 is a finite volume, three-equation code which uses the homogenous equilibrium assumption for solving two-phase flow [24].

Unlike RELAP5-3D, VIPRE-01 does not require explicit definition of component structures in order to define the system boundaries. Instead, a pre-defined geometric solution scheme is already built into VIPRE-01 based on core subchannel geometry. The user enters geometric information for  $N$  number of channels and  $M$  number of fuel rods. The user also defines which channels and fuel rods are physically linked to one another. This information was entered into VIPRE-01 following the MASLWR modeling methodology previously described. A tenth channel type was added to allow random perturbations in the hot channel geometry without affecting the remaining channels.

In addition to geometric information, the user must specify appropriate two-phase flow correlations and heat transfer correlations for VIPRE-01 to apply. Based on previous subchannel modeling of the MASLWR core, the default EPRI models were selected for the two-phase friction multiplier, subcooled void correlation, and bulk void correlation [5]. Heat transfer between the fuel rods and coolant is dependent on the local flow regime. For the single-phase region, the Dittus-Boelter correlation was applied [28]. For both the subcooled nucleate boiling and saturated nucleate boiling regions, the Chen correlation was selected [29]. The Chen correlation was selected as it is the default RELAP5-3D heat transfer correlation [31].

Unlike RELAP5-3D, VIPRE-01 has been developed with a fully implicit steady-state solution scheme. Three numerical solution methods are available: an iterative solution, a direct solution, and a recirculation solution. The recirculation solution was adapted

from COBRA-WC to allow reverse and recirculating flows [24]. The recirculation solution scheme is recommended when axial flows are expected become locally small [24]. Because the MASLWR has a much smaller flow rate than traditional NPPs, the recirculation solution was used. Default convergence values for the recirculation solution were applied [25].

### **Figures of Merit**

Uncertainty and sensitivity analysis requires the identification of system response variables, referred to as figures of merit, to be analyzed. There exists a vast number of potential FOM which can be extracted from the RELAP5-3D and VIPRE-01 model outputs. Relevant FOM are therefore selected based on U.S. NRC licensing requirements.

In the United States, new reactor designs are subject to the licensing approval process established by the U.S. NRC in NUREG-800. Relevant chapters to subchannel analysis include Chapter 4.2, which establishes the acceptance criteria for fuel performance characteristics, and Chapter 4.4, which establishes the acceptance criteria for thermal hydraulic calculations [33,34]. Chapters 4.2 and 4.4 in part are designed to satisfy General Design Criteria (GDC) 10 found in Appendix A of 10 CFR Part 50 [35]. This criterion requires that specified acceptable fuel design limits (SAFDLs) are not exceed during normal operation or Anticipated Operation Occurrences (AOOs). To ensure GDC 10 is satisfied, Chapter 4.2 requires evaluation of cladding and fuel pellet temperature to ensure failure does not occur [33]. Chapter 4.4 requires that there should be a 95% probability at the 95% confidence level that the hot rod in the core does not experience a DNB condition during normal operation or AOOs [34]. From these requirements, the following FOMs have been identified: peak cladding temperature, peak fuel temperature, and minimum departure from nuclear boiling ratio (MDNBR). These FOM will be evaluated for the hot channel in the core.

### *DNB Correlation*

For a heated, pressurized flow channel, departure from nuclear boiling is characterized by the formation of a vapor blanket between the heated wall and the bulk liquid coolant [27]. This vapor blanket greatly increases the thermal resistance between the heated wall and the coolant, causing a temperature spike in the heated wall. This temperature spike may damage the heated structure. A departure from nuclear boiling condition occurs when the local heat flux from the heated surface exceeds the required local heat flux to produce such a vapor blanket, referred to as the critical heat flux. Local DNBR is given by

$$\text{DNBR} = \frac{q''_{CHF}}{q''_{local}}, \quad (4-35)$$

where  $q''_{local}$  is the local heat flux through the heated wall to the coolant and  $q''_{CHF}$  is the local critical heat flux.

The mechanism behind CHF is complex, and many different correlations exist for different fuel geometries and flow conditions [36]. Using multiple CHF correlations to calculate DNBR would introduce additional uncertainty sources. Therefore, a single CHF correlation is selected to calculate DNBR for both RELAP5-3D and VIPRE-01. The selected CHF correlation is the Groeneveld 2006 AECL CHF look-up tables [36]. The 2006 AECL CHF table is based on a database containing over 30,000 data points compiled from numerous CHF studies. This correlation was selected given the lack of a MASLWR specific CHF correlation data and because it is often used as a benchmark for other CHF correlations. The 2006 AECL CHF look-up tables present CHF in a heated channel as a function of pressure, mass flux, equilibrium quality, and channel diameter [36]. Local CHF is calculated as

$$q''_{CHF} = f(P_l, G_l, X_l) \left( \frac{D_H}{0.8 \text{ cm}} \right)^{-\frac{1}{2}} \quad (4-36)$$

where  $P_l$  is the local fluid pressure,  $G_l$  is the local mass flux, and  $X_l$  is the local equilibrium quality [36]. Equilibrium quality is defined as

$$X_l = \frac{h_l - h_f}{h_g - h_f}, \quad (4-37)$$

where  $h_l$  is the local fluid enthalpy,  $h_f$  is the saturated fluid enthalpy, and  $h_g$  is the saturated vapor enthalpy [27].

### **Input Uncertainty**

The International Atomic Energy Association (IAEA) has identified three major sources of uncertainty in thermal hydraulic calculations: code or model uncertainty, representation or simulation uncertainty, and plant uncertainty [37]. In this study, code uncertainty is not considered because this requires access to the source code. As much as possible, modeling of the MASLWR core in RELAP5-3D and VIPRE-01 has been consistent in order to reduce representation uncertainty between the two codes. Therefore, plant uncertainty is evaluated herein. In this study, plant uncertainty is considered as epistemic uncertainty associated with user entered values to the RELAP5-3D and VIPRE-01 input decks.

Some uncertainty methodologies, such as the CSAU method, limit the number of uncertain parameters through expert judgment [6]. This is done through the PIRT as developed in Step 3 of the CSAU process. Parameters are limited because the parametric response surface methodology used in CSAU is dependent on the number of parameters used. As discussed in Chapter 2, the non-parametric methods used in this study are independent of the number of uncertain parameters. However, there is still motivation to limit the number of evaluated uncertain parameters. As this is a first time uncertainty study on the MASLWR design, analysis rigor should be limited to prevent erroneous conclusions which might be drawn using too large a number of uncertain parameters. Second, the lack of MASLWR operational data within the core region (applicable to subchannel analysis) requires the use of user judgment to select and assign an uncertainty distribution to a parameter. Therefore, 12 uncertain parameters have been identified for evaluation. These parameters are considered influential on the selected figures of merit. Parameters are selected with the intention

that as design and analysis maturity improves, the characterization of uncertainty sources would advance as well. These parameters are separated into two categories: plant operation uncertainty (Table 4-6) and manufacturing uncertainty (Table 4-7). Footnotes are provided to offer more detailed information when required.

Table 4-6: Nominal operational parameter values and ranges of uncertainty.

Parameter	Nominal		Uncertainty	
	Value	Reference	Range	Source
Power	150 MW	[2]	$\pm 1.5\%$	PWR operational uncertainty [38].*
Core Exit Pressure	7.8 MPa	Table 4-1 [2]	$\pm 1.3\%$	PWR operational uncertainty [38].*
System Flow	596 kg/s	Table 4-1 [2]	$\pm 2.9\%$	PWR operational uncertainty [38].*
Inlet Temperature	491.8 K	Table 4-1 [2]	$\pm 0.9\%$	PWR operational uncertainty [38].*
Radial Power Factor (Hot Channel)	1.15	Average between min/max values, Figure 4-5.2.4.A [22].	$\pm 8.7\%$	Range between min/max values in Figure 4-5.2.4.A [22]. <sup>†</sup>
Axial Peaking Factor (Hot Channel)	1.19	Average between min/max values, Figure 4-5.2.4.B [22].	$\pm 9.2\%$	Range between min/max values in Figure 4-5.2.4.B [22]. <sup>†</sup>

---

\* These are operational uncertainties and are taken from North Anna Units 1 and 2. These reactors are of a 900 MW<sub>e</sub> Westinghouse PWR design. These values are selected because they present uncertainties found in an operating NPP.

<sup>†</sup> Uncertainty includes effect from fuel burn-up and flow rate.

Table 4-7: Nominal manufactured values and ranges of uncertainty.

Parameter	Nominal		Uncertainty	
	Value	Reference	Range	Source
Grid Spacer Form Loss	0.86	[4]	$\pm 20\%$	Assumed value. <sup>‡</sup>
Clad OD (Hot Channel)	0.952 cm	[2]	$\pm 0.008$ cm	Sum of dimensional uncertainty associated with clad ID and clad thickness, Table 4.4 [30].
Gap Conductivity	0.28 W/m-K	Helium thermal conductivity model with MATPRO at 700°C, Figure 4.6 [30].	$\pm 5\%$	Experiment data bounds, Section 4.4.5 [30].
Gap Thickness	0.006 cm	[2]	$\pm 0.0013$ cm	Dimensional uncertainty associated with fuel pellet OD, Table 4.4 [30].
UO <sub>2</sub> Fuel Conductivity	3.6 W/m-K	Average between 200°C and 1000°C, Table 8.1A [27].	$\pm 0.5$ W/m-K	Experimental data bounds, Section 4.4.1 [30].
Zirconium Conductivity	14.0 W/m-K	Zircaloy at 500°C predicted by MATPRO, Figure 4.5 [30].	+5/-3 W/m-K	Experimental data bounds, Section 4.4.4 [30].

<sup>‡</sup> Because the grid spacer loss coefficient is an estimated value, it is assigned a large range of uncertainty. Grid spacer pressure drop is extensively tested on a design specific basis. It is expected that pressure drop experiments for MASLWR specific fuel assembly geometry will significantly reduce this uncertainty.

### *Input Sampling*

Each uncertain input parameter must be assigned a distribution which will be propagated through the RELAP5-3D and VIPRE-01 system codes. For this study, each uncertain parameter is assigned a uniform distribution as this is considered conservative, relative to alternate commonly utilized distributions such as normal and binomial [6]. Additionally, each uncertain parameter is assumed independent from one another. In reality, it is likely some degree of dependence exists. This is especially true under natural circulation where at steady state, single phase flow rate is proportional to thermal power on the order  $Q^{1/3}$  [39]. However, this assumption still allows valid comparisons between uncertainty and sensitivity results from RELAP5-3D and VIPRE-01.

The uniform distribution is considered conservative because the extreme values (i.e., the minimum and maximum values) are equally likely to occur as the nominal value. The PDF for the uniform distribution is given by [40]

$$\Pr[a \leq X \leq b] = f(x) = \frac{1}{b-a}. \quad (4-38)$$

where  $a$  and  $b$  are the minimum and maximum values a parameter can take. To sample from the PDF, it is converted into the cumulative probability distribution function (CDF), defined for the uniform distribution by [40]

$$\Pr[X \leq x] = F(x) = \frac{x-a}{b-a}. \quad (4-39)$$

Solving equation (4-39) for  $x$  gives

$$x = a + F(x)[b-a], \quad (4-40)$$

where  $F(x)$  represents the cumulative probability, ranging from 0 to 1.

Simplified random sampling (SRS) is used to sample values from equation (4-40). To begin, a random number uniformly distributed between 0 and 1 is chosen. This random number is then substituted into equation (4-40) as  $F(x)$ . Solving equation (4-40) now gives a randomly sampled value,  $x$ , for a given uncertain input parameter. In

this manner, values are uniformly sampled over the range of uncertainty for a specific parameter.

### **Uncertainty Analysis**

Uncertainty analysis seeks to characterize the total uncertainty in a system's response given the cumulative effect of uncertainties found in the input parameters. This study employs sampling based uncertainty analysis methods [3]. Such methods provide accurate results for relatively little development cost. These advantages come with the caveat of requiring many data samples. Additionally, this study uses non-parametric methods. These methods do not assume a distribution shape for the final system response. Therefore, non-parametric methods are suitable for non-linear systems where it may be difficult to assign a parametric distribution. Finally, this study assumes that all output variables are either completely dependent on or independent from one another. Completely dependent variables are calculated through correlations of the remaining output variables (e.g., DNBR).

Data generation required for uncertainty analysis begins through SRS of each input. Once a random value for each input is selected, these values are passed through the RELAP5-3D and VIPRE-01 system codes. Calculated values for each FOM are extracted and stored. This process continues until a sufficient number of data samples have been generated.

To quantify uncertainty in a specific FOM, the output data must be synthesized into an empirical cumulative distribution function (ECDF) and plotted with confidence bands. This method is preferred as it preserves the true distribution shape of the output FOM, where a method such as Wilks' method only expresses uncertainty as a single value. Additionally, a comparison of the Wilks' method and a Monte-Carlo calculation has shown the Wilks' method yields uncertainty values that exhibit large fluctuations when performed at the first-order [41]. Finally, a large number of data samples are required

for both the ECDF method and sensitivity analysis. Therefore, the same set of output data samples are used for both uncertainty and sensitivity analysis.

*ECDF with Confidence Bands*

From [43], the empirical distribution function is defined as

$$\hat{F}_n(x) = \frac{1}{n} \sum_{i=1}^n I(X_i \leq x), \quad (4-41)$$

where  $n$  is the total number of samples and

$$I(X_i \leq x) = \begin{cases} 1 & \text{if } X_i \leq x \\ 0 & \text{if } X_i > x \end{cases}. \quad (4-42)$$

Equation (4-41) can be expressed informally as

$$\hat{F}_n(x) = \frac{\text{number of elements in the sample} \leq x}{n}. \quad (4-43)$$

The ability of the ECDF to accurately represent the true output distribution is supported by the Glivenko-Cantelli Theorem,

$$\sup_x |\hat{F}_n(x) - F(x)| \xrightarrow{a.s.} 0, \quad (4-44)$$

which implies that the ECDF uniformly converges to the true distribution as  $n$  increases [43].

There exists an additional source of uncertainty caused by statistical variation in the output FOM data. This variation is accounted for by assigning confidence bands over the entire range of the ECDF. A confidence band is derived from the Dvoretzky-Kiefer-Wolfowitz (DKW) inequality

$$\Pr \left( \sup_x |F(x) - \hat{F}_n(x)| > \varepsilon \right) \leq 2e^{-2n\varepsilon^2}. \quad (4-45)$$

The confidence band for  $F$  is given by

$$L(x) = \max \{ \hat{F}_n(x) - \varepsilon_n, 0 \} \quad (4-46)$$

and

$$U(x) = \min\{\hat{F}_n(x) + \varepsilon_n, 1\}, \quad (4-47)$$

where

$$\varepsilon_n = \sqrt{\frac{1}{2n} \ln\left(\frac{2}{\alpha}\right)} \quad (4-48)$$

and  $1-\alpha$  is the desired level of confidence [43].  $L(x)$  represents the lower confidence bound and  $U(x)$  represents the upper confidence bound on the ECDF  $\hat{F}_n(x)$ .

To demonstrate this method, Figure 4-10 shows the PDF and CDF for a normal distribution with a mean of zero and a standard deviation of one.

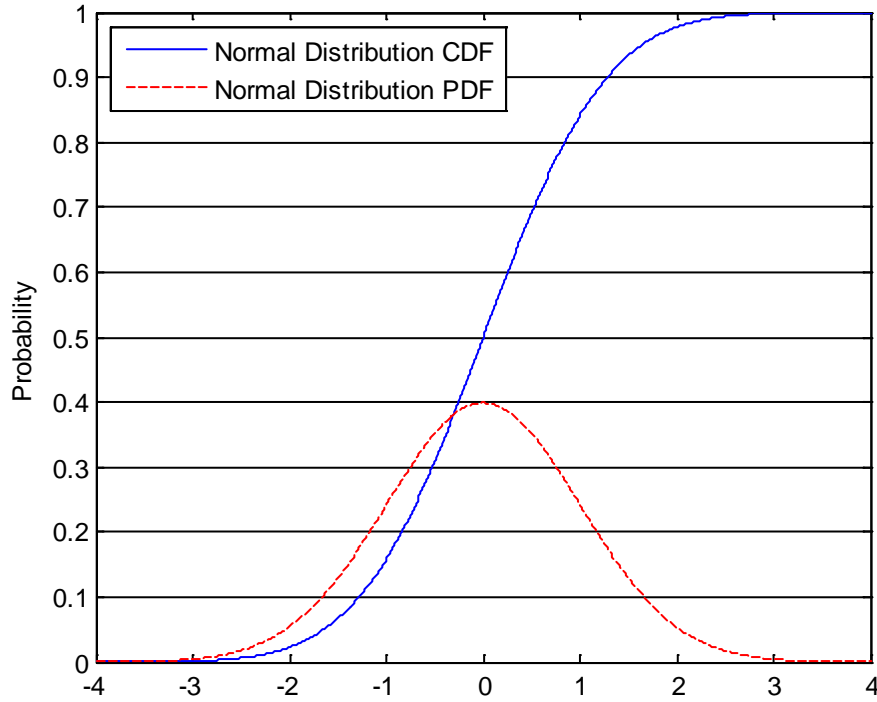


Figure 4-10: Normal distribution with mean of zero and standard deviation of one.

A CDF, such as the one shown in Figure 4-10, is typically found by integrating over the PDF of the desired data set [42]. However, if random data samples were taken from the PDF instead, these points could be used with Equation 4-41 to form the

ECDF for that data set. In this example, assuming the number of data points was sufficiently large, the blue line shown in Figure 4-10 would now represent the ECDF for a normal distribution with a mean of zero and standard deviation of one. Confidence bands from the DKW inequality are then assigned (Figure 4-11).

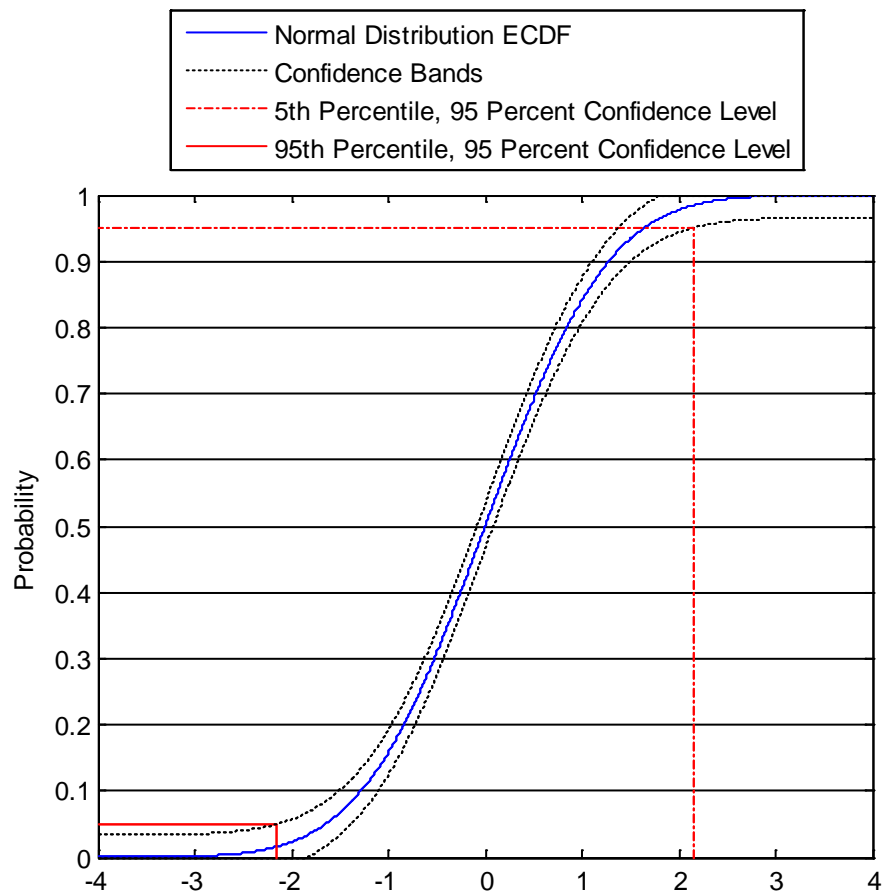


Figure 4-11: Normal distribution ECDF with confidence bands.

In Figure 4-11, the vertical dashed red line represents the maximum value which bounds 95 percent of all possible output values at the 95 percent confidence level. This value was found as the intersection point between the 95th percentile, represented by the horizontal red dashed line, and the lower confidence band. Similarly, the vertical solid red line represents the minimum value which bounds 95 percent of all possible output values at the 95 percent confidence level. This value was found as the

intersection point between the 5th percentile, represented by the horizontal solid red line, and the upper confidence band. In this manner, the minimum or maximum 95 percent probability value at the 95 confidence level can be determined.

### **Sensitivity Analysis**

Sensitivity analysis seeks to characterize the contribution individual uncertain parameters have on the total uncertainty in the system response [3]. Results from sensitivity analysis can be used to justify removing insignificant parameters from the overall analysis. Alternatively, sensitivity results can be used to identify significant parameters which may lack a sufficient knowledge base. This information can be used to focus experimental testing on those parameters which are highly influential on the system response. Regression analysis-based methods are commonly used to measure sensitivity [3]. This study applies a linear regression-based approach, specifically partial ranked correlation coefficients (PRCCs), are used as the primary measure of sensitivity.

#### *Rank Transformation*

Due to the non-linear nature of thermal hydraulic calculations, linear regression-based sensitivity measures may not capture the full influence an input parameter has on the system response. However, if the system response and an input parameter exhibit a nonlinear yet monotonic relationship, rank transformation may be applied to convert the nonlinear relationship into a linear analogue. To perform rank transformation, each data point is assigned an integer value based on its relative ranking to all other data points in that vector. For example, the smallest data point is assigned a rank of 1, the second smallest a rank of 2, and so on [3]. Applying rank transformation to data which exhibits non-linear yet monotonic relationships can improve sensitivity analysis results [3].

#### *Scatter Plots*

Scatter plots provide a simple, qualitative measure of influence and are often used as the starting point for sensitivity analysis [3]. Scatter plots are created by plotting

ranked input data  $x$  versus ranked output data  $y$ . Scatter plots allow for visual examination of the relationship between  $x$  and  $y$  and can qualitatively confirm whether that relationship is monotonic or non-monotonic.

### *Partial Rank Correlation Coefficients*

Correlation coefficients provide a measure of strength for the linear relation that exists between two variables  $x$  and  $y$  [3]. A correlation coefficient takes a value between  $-1$  and  $1$ . A positive value indicates a direct relationship between  $x$  and  $y$  while a negative value indicates an inverse relationship. The absolute value of the correlation coefficient gives a measure between  $0$  and  $1$ . Values close to  $1$  indicate that  $x$  is highly influential on  $y$ , while values close to  $0$  indicate  $x$  has no influence on  $y$ .

Due to the non-parametric sampling used during uncertainty analysis, the corresponding sensitivity analysis is global in nature [44]. While this is a more accurate representation of the system, it also means the correlation between  $x$  and  $y$  is not solely a function of the influence  $x$  has on  $y$ ; it is also affected by the influence other uncertain parameters  $x_p$  have on  $y$ . To remove this secondary influence, a linear regression model is built in the form

$$\hat{x}_j = c_0 + \sum_{\substack{p=1 \\ p \neq j}}^{nX} c_p x_p \quad (4-49)$$

and

$$\hat{y} = b_0 + \sum_{\substack{p=1 \\ p \neq j}}^{nX} b_p x_p, \quad (4-50)$$

where  $j$  is the of current input parameter of interest,  $y$  is the current FOM of interest,  $nX$  is the total number of input parameters, and  $x_p$  represents the remaining input parameters [3]. Two new variables are now defined:  $x_j - \hat{x}_j$  and  $y - \hat{y}$  [3]. These

variables represent input  $x_j$  and FOM  $y$  with the linear effects of other inputs  $x_p$  having been removed.

The partial correlation coefficient between  $x_j$  and  $y$  is defined as

$$c(x_j, y) = \frac{\sum_{i=1}^{nS} ((x_{ij} - \hat{x}_{ij}) - (\overline{x_j - \hat{x}_j})) ((y_i - \hat{y}_i) - (\overline{y - \hat{y}}))}{\left[ \sum_{i=1}^{nS} ((x_{ij} - \hat{x}_{ij}) - (\overline{x_j - \hat{x}_j}))^2 \right]^{1/2} \left[ \sum_{i=1}^{nS} ((y_i - \hat{y}_i) - (\overline{y - \hat{y}}))^2 \right]^{1/2}}, \quad (4-51)$$

where

$$\overline{x_j - \hat{x}_j} = \frac{\sum_{i=1}^{nS} x_{ij} - \hat{x}_{ij}}{nS}, \quad (4-52)$$

$$\overline{y - \hat{y}} = \frac{\sum_{i=1}^{nS} y - \hat{y}}{nS}, \quad (4-53)$$

and  $nS$  is the total number of data samples [3]. Finally, solving equation (4-51) using rank transformed data yields the PRCC between input  $x_j$  and FOM  $y$ .

### *p-values*

A PRCC value which approaches zero indicates  $x_j$  has little influence on  $y$ . However, this does not claim that  $x_j$  has no influence  $y$ . In order to qualify such a claim, p-values are instead used. The common significance level of 0.05 is applied in this study [42]. If the p-value calculated between  $x_j$  and  $y$  is  $> 0.05$ , it is claimed that  $x_j$  has no influence on  $y$  under the set of evaluated input parameter uncertainties.

### **Summary**

The overall calculation methodology is separated into two phases: data generation and data processing. The data generation phase is performed via a Fortran 90 script. The RELAP5-3D and VIPRE-01 base models are programmed into this script.

Additionally, a desired range of uncertainty for each input parameter is specified. The script then performs SRS on each input to select a random value within that range. Using these values, either a RELAP5-3D or VIPRE-01 input deck is written to a separate text file. The script uses a system command to execute a RELAP5-3D or VIPRE-01 run using the generated input deck. Once complete, the resulting output file is read and the following values for the hot channel are stored: fuel centerline temperature, clad temperature, equilibrium quality, mass flux, local pressure, and heat flux. This process is repeated until  $N$  number of data samples have been recorded. Finally, all extracted output information is written to a text file for processing.

The data processing phase is performed via MATLAB R2012b using routines from the Statistics Toolbox package. The previously generated results text file is read into MATLAB. A routine calculates CHF using linear interpolation on the 2006 AECL CHF look-up table. Confidence bands are calculated for each FOM using the DKW method. The PRCCs and  $p$ -values are also calculated using the "partialcorr" function from the MATLAB Statistics Toolbox package. Finally, MATLAB generates plots detailing uncertainty and sensitivity results. This overall calculation methodology is presented in Figure 4-12.

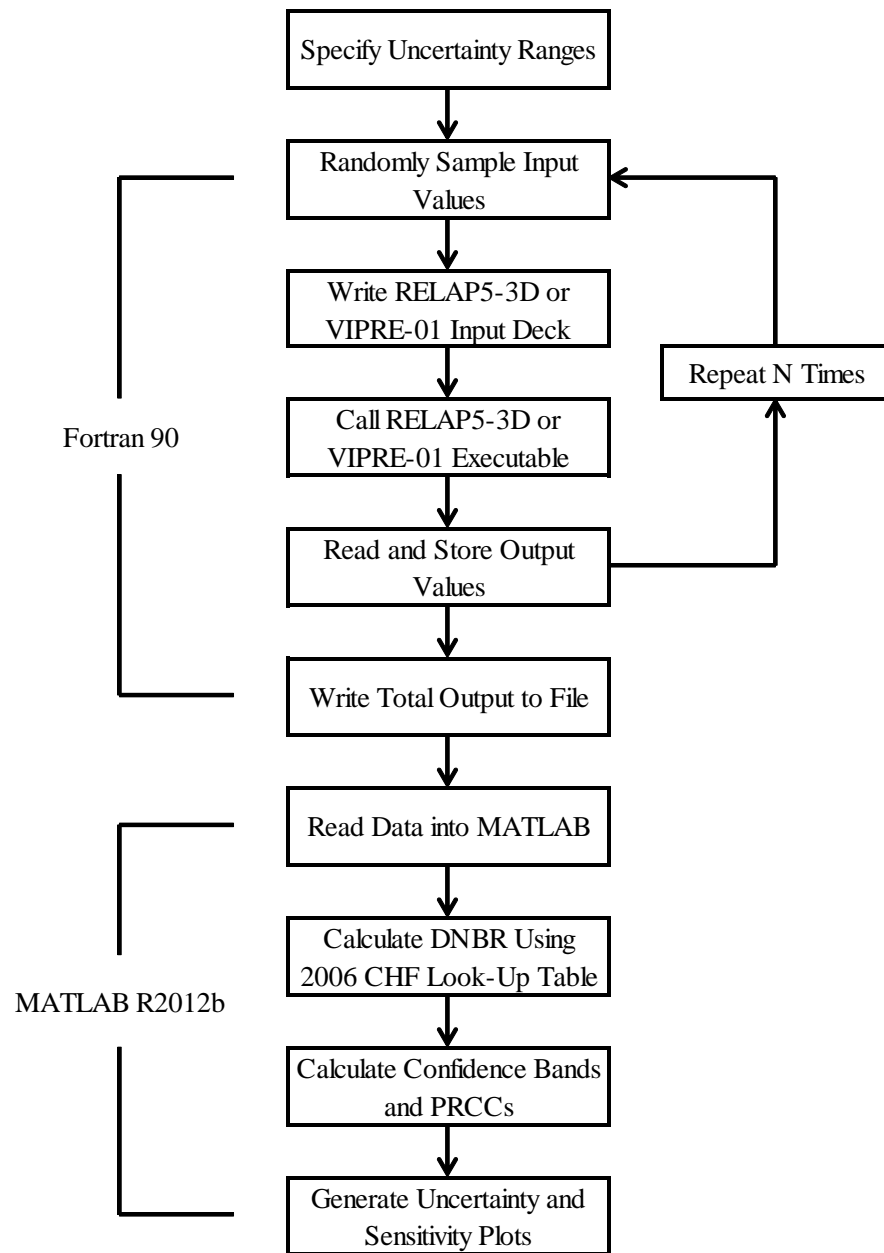


Figure 4-12: Overall methodology summary.

## 5. RESULTS AND DISCUSSION

RELAP5-3D and VIPRE-01 models of the MASLWR core were developed as described in Chapter 4. The calculation methodology shown in Figure 4-12 was applied using randomly sampled input values for the parameters identified in Table 4-6 and Table 4-7. The same sampled values were applied to both RELAP5-3D and VIPRE-01 models. Uncertainty and sensitivity analysis was performed on the data set using the methods described in Chapter 4. Justification for the number of utilized samples is first discussed.

### **Influence of Sample Size**

Sample size  $N$  affects three factors: uncertainty analysis, sensitivity analysis, and calculation execution time. The sample size effects the uncertainty results in two related ways. First, equation (4-44) shows that as  $N$  increases, the ECDF will converge to the true system response. Second, equation (4-45) shows that the confidence band surrounding the ECDF shrinks as  $N$  increases. From equation (4-45), both these effects occur on the order  $N^{-1/2}$ . Sensitivity analysis requires that the number of samples is significantly greater than the number of uncertain inputs. Finally, preliminary calculations show RELAP5-3D requires approximately 60 seconds to complete a single execution. With these three factors in mind, a sample size of  $N$  equals 5000 was selected. To demonstrate the effect of  $N$  on uncertainty results, Figure 5-1 shows the DKW error term given by equation (4-48) plotted as a percent from  $N$  equals 50 to 10,000 at the 95 percent confidence level.

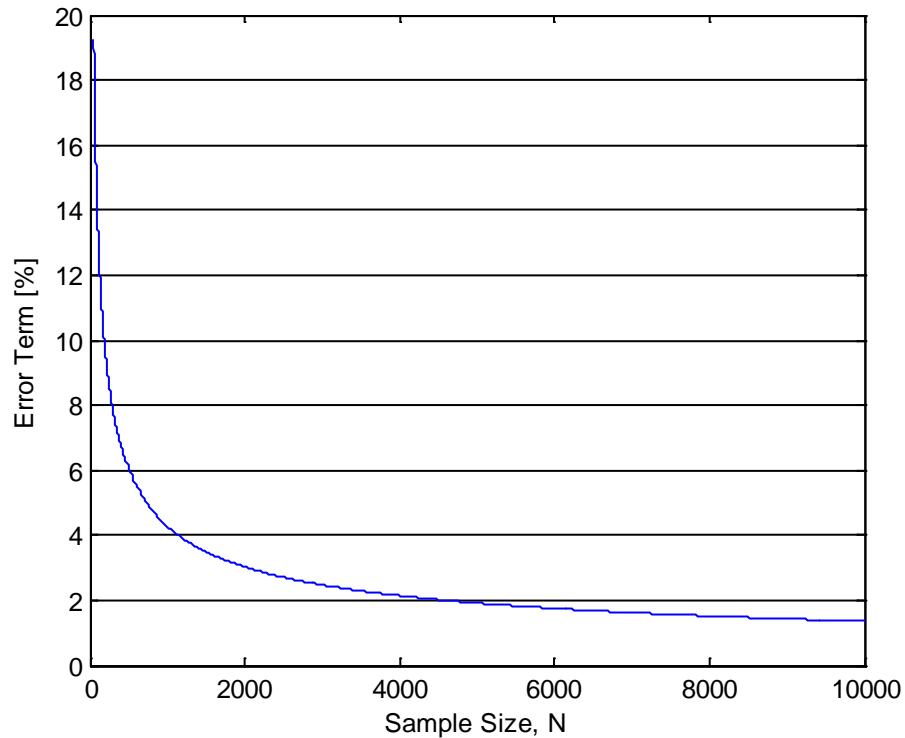


Figure 5-1: DKW error term versus increasing N.

For a sample size of  $N$  equals 5000, the error term in Figure 5-1 is approximately 1.9 percent. For uncertainty analysis, this means the 95<sup>th</sup> percentile of the true response is bounded by the 93.1<sup>th</sup> and 96.9<sup>th</sup> percentiles of the calculated ECDF at the 95 percent confidence level. Similarly, the 5<sup>th</sup> percentile of the true system response is bounded by the 3.1<sup>th</sup> and 6.9<sup>th</sup> percentiles of the calculated ECDF at the 95 percent confidence level.

### **RELAP5-3D and VIPRE-01 Model Results**

Prior to discussing uncertainty and sensitivity results, a comparison is made between the RELAP5-3D and VIPRE-01 thermal hydraulic predictions in the hot channel. Results are plotted in the hot channel heated region as a function of vertical distance from the core inlet. Solid lines represent the mean value across all 5000 data samples for a respective axial location. Long dashed lines indicate the 5<sup>th</sup> and 95<sup>th</sup> percentiles

given a 95 percent confidence interval. Short dashed lines show the absolute minimum and maximum values seen in the 5000 samples at that location. Parameters related to the FOM chosen in Chapter 4 are discussed below.

### *Pressure*

Local pressure is the first parameter required to calculate CHF in equation (4-36). Figure 5-2 shows the local pressure in the hot channel predicted by RELAP5-3D and VIPRE-01. Pressure predictions between the two codes show good agreement. The downward trend in local pressure is explained by the decreasing static coolant pressure relative to the core exit as the vertical distance from the core inlet increases. Static pressure changes linearly with vertical distance, so the linear trend in Figure 5-2 is expected.

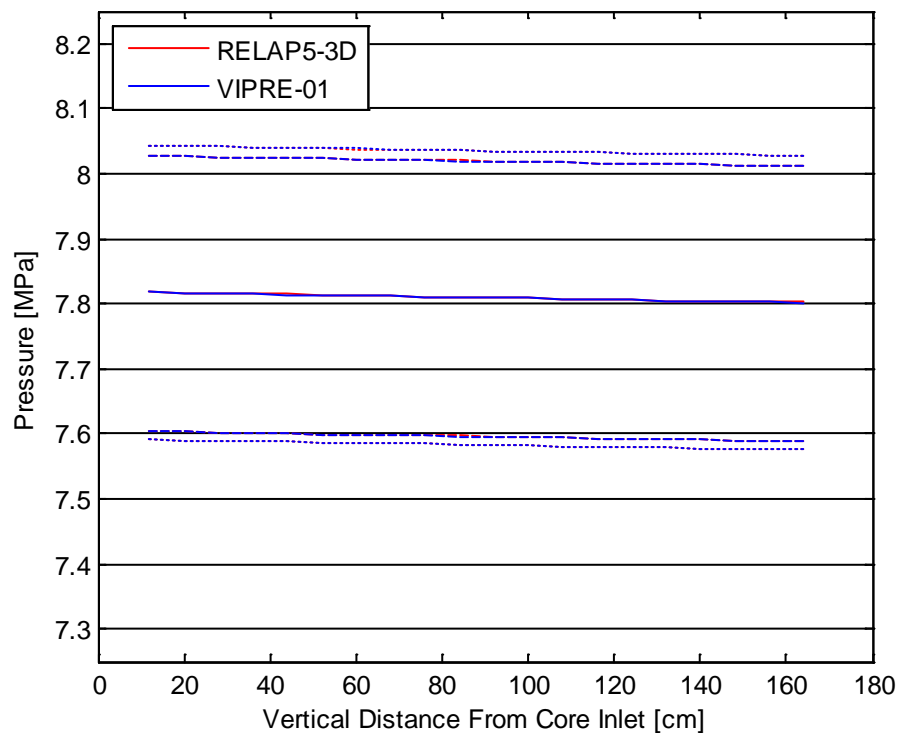


Figure 5-2: Local pressure in the hot channel.

### Mass Flux

Mass flux is the second parameter required to calculate CHF in equation (4-36). Mass flux is defined as the ratio of coolant mass flow rate through a control volume to the cross sectional area of the respective control volume. In this study, focus is directed toward the limiting safety related location within the core; therefore, the hot channel assumes the control volume herein. The axial distribution of mass flux in the hot channel is presented in Figure 5-3.

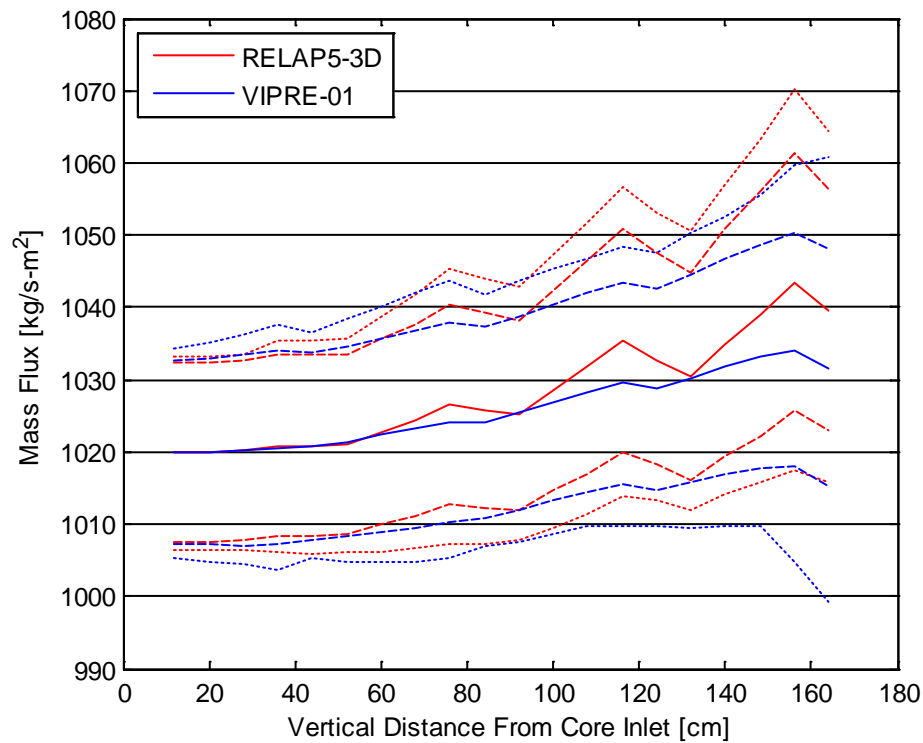


Figure 5-3: Mass flux distribution through the hot channel.

From Figure 5-3, RELAP5-3D and VIPRE-01 both show an increase in mass flux with an increase in vertical position within the hot channel. This general trend is expected as the coolant in the hot channel will thermally expand at a faster rate relative to coolant in surrounding channels. This creates a pressure difference which drives coolant from adjacent channels into the hot channel. The localized reduction in mass flux quantities (or ‘dips’) seen in Figure 5-3 correspond to grid spacer locations. In an

attempt to further understand the discrepancies observed in explicit mass flux values between RELAP5-3D and VIPRE-01, mass flux is calculated at nominal conditions at zero power and with grid spacers removed (Figure 5-4).

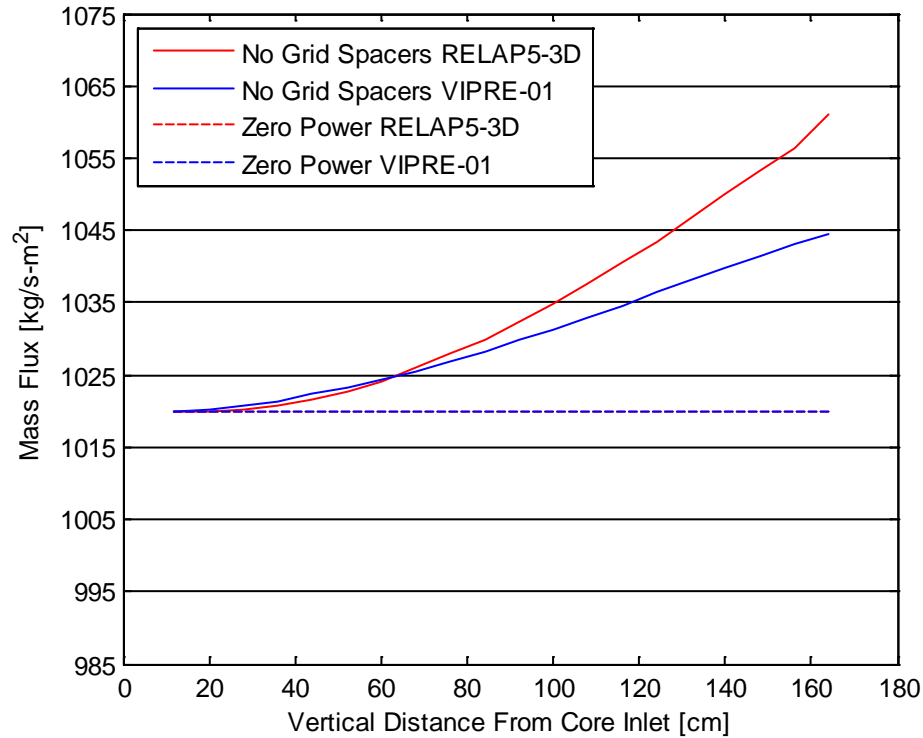


Figure 5-4: Mass flux with no grid spacers and at zero power.

Recall that the implemented models both utilize a forced flow core inlet boundary condition which is independent from core power. At zero power, RELAP5-3D and VIPRE-01 both predict a constant mass flux of  $1019.9 \text{ kg/s-m}^2$  through the hot channel. This verifies that the two models are hydraulically correct. Because the increase in mass flux is driven by the thermal expansion of the coolant, Figure 5-4 indicates that a bias exists between RELAP5-3D and VIPRE-01 fluid property calculations. Considering the case with no grid spacers, the maximum difference between RELAP5-3D and VIPRE-01 predicted mass flux is 1.68 percent. This lends further confidence toward the development of each respective model so as to allow for

claims that any calculation deviations result from the computation within the codes rather than the construction of the models themselves.

### *Equilibrium Quality*

The final parameter required to calculate CHF is equilibrium quality. Equilibrium quality, defined in equation (4-37), is plotted in Figure 5-5 for RELAP5-3D and VIPRE-01. The predicted equilibrium quality distributions between the two codes are in good agreement with the largest deviations occurring near the core exit. This difference near the core exit may be tied to the computation of mass flux within the two codes. Note that the VIPRE-01 model predicts slightly higher values at the exit than that of RELAP, this directly correlates to a lower mass flux as can be seen in Figure 5-3.

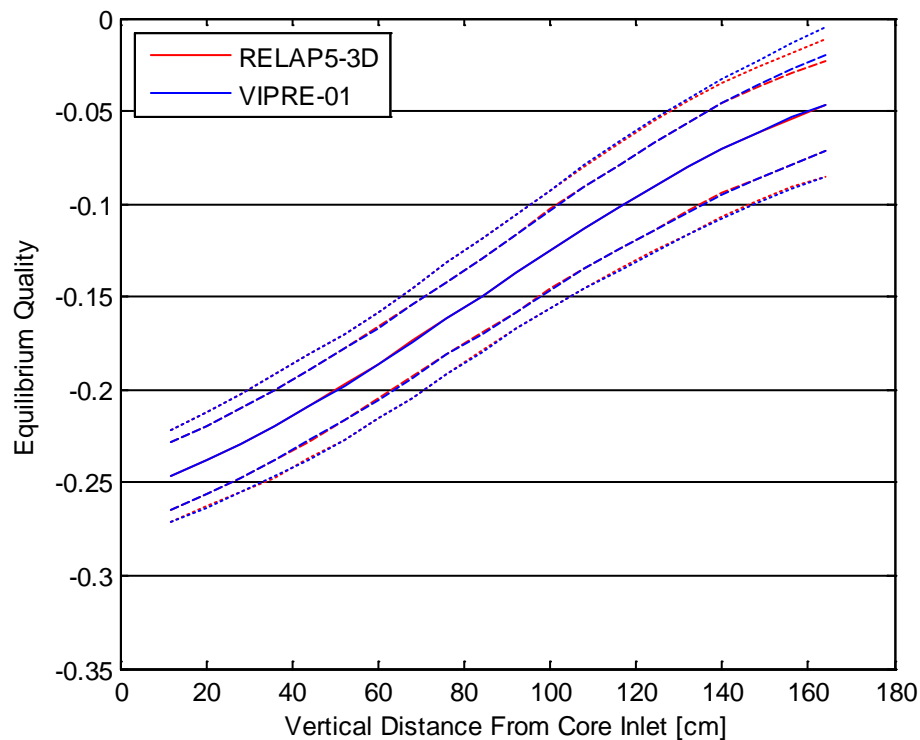


Figure 5-5: Equilibrium quality in the hot channel.

Because the equilibrium quality is less than zero, it is interpreted as the amount of subcooling in the coolant. Under the evaluated conditions, both RELAP5-3D and

VIPRE-01 show the bulk coolant never reaches saturation (i.e., equilibrium quality never exceeds zero). Equilibrium quality increases as thermal energy from the fuel rods is deposited into the coolant. The local magnitude of energy deposition is controlled by the axial power cosine shape. Integrating this profile over the length of the hot channel yields an expected sinusoidal profile for equilibrium quality. This trend is observed in Figure 5-5.

#### *Heat Flux*

Local heat flux is required to calculate DNBR in equation (4-35). The heat flux detailed herein refers to the local heat transfer rate from the clad outer surface to the coolant per unit area. The axial heat flux distribution calculated by RELAP5-3D and VIPRE-01 is shown in Figure 5-6. Heat flux calculations between the two codes are in excellent agreement. At steady state, heat flux is a function of local power and clad OD. The overlapping heat flux distributions seen in Figure 5-6 verify that local power profiles and channel geometry are correctly entered into the RELAP5-3D and VIPRE-01 models.

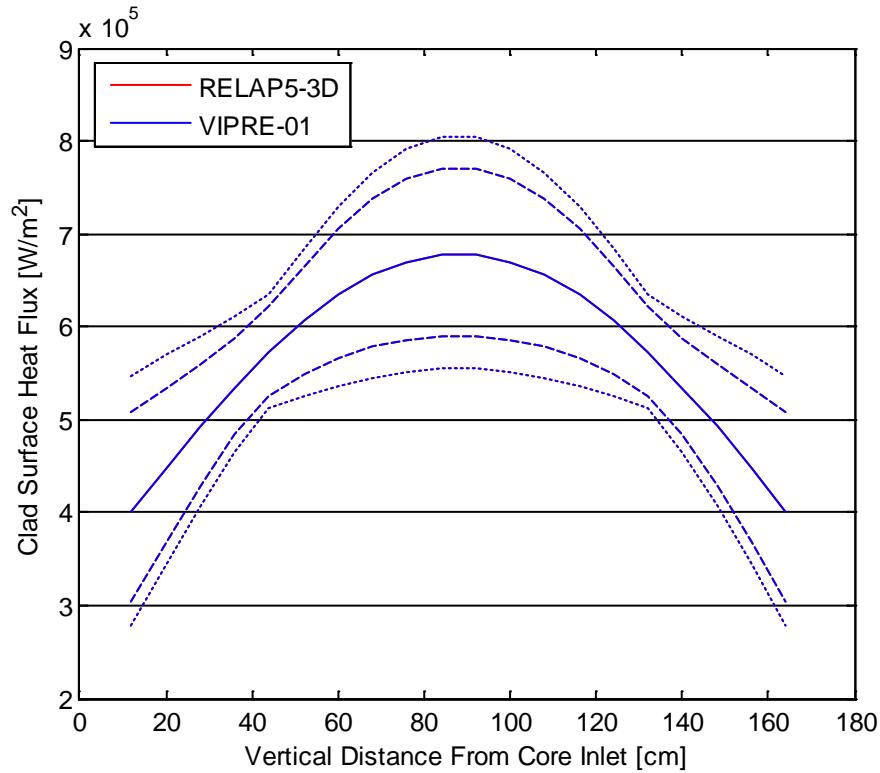


Figure 5-6: Clad surface heat flux in the hot channel.

As the axial power shape is the only nonuniform parameter which affects heat flux, the heat flux distribution is expected to follow the cosine shape described in equation (4-22). This distribution is reflected in Figure 5-6. The deflections in the upper and lower heat flux bands result from the axial power shape normalization equations described in Chapter 4. Solving these equations yield a constant local axial power factor at approximately 45 cm and 131 cm, regardless of the chosen axial peaking factor. The axial power factors at the remaining channel locations vary around these two points. A similar effect can be seen in Figure 4-8 for the radial power shape. This effect creates a relatively flat maximum heat flux profile in the lower and upper portions of the channel, while a relatively steep maximum heat flux profile is exhibited in the channel center. The opposite trend is observed for the minimum heat flux profile.

### DNBR

As MDNBR was selected as a FOM, the hot channel DNBR profile is presented below. Figure 5-7 shows the local hot channel DNBR for RELAP5-3D and VIPRE-01. The DNBR was calculated during post-processing using equation (4-35). Local CHF was computed via the 2006 AECL CHF look-up table using linear interpolation between mass flux, pressure, and equilibrium quality.

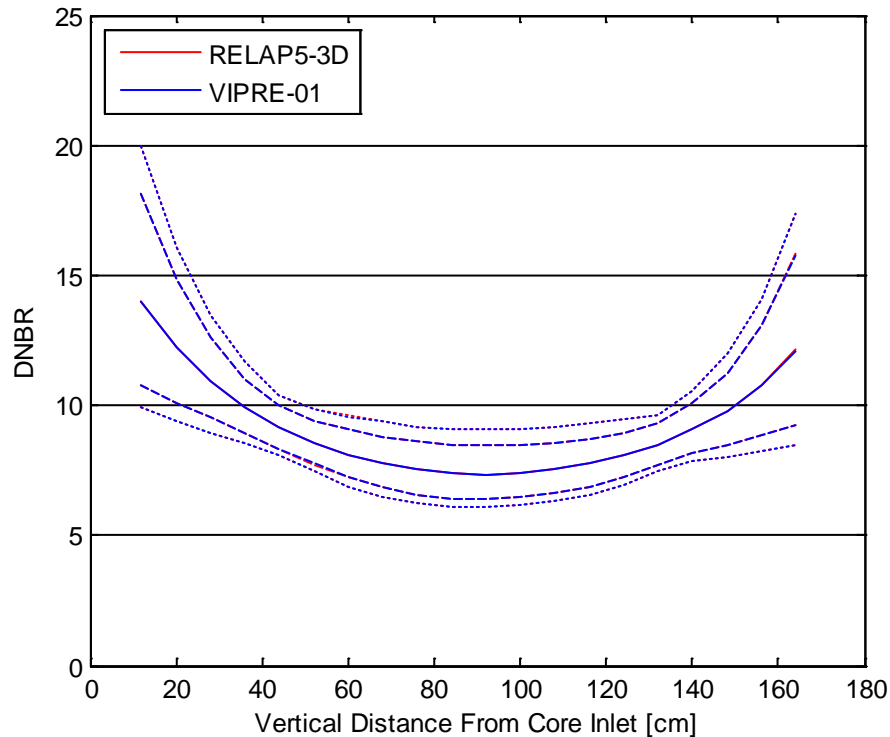


Figure 5-7: Local DNBR in the hot channel.

The DNBR distributions predicted by RELAP5-3D and VIPRE-01 are in good agreement. This is expected given the good agreement in the pressure, equilibrium quality, and heat flux results. This also indicates DNBR is much less sensitive to mass flux than the three previous quantities. Furthermore, the inverted cosine shape indicates DNBR is highly sensitive to the local heat flux distribution. This inverted cosine profile is expected from equation (4-35), where local heat flux is found in the denominator of the DNBR solution. The continually increasing equilibrium quality

seen in Figure 5-5 shifts this cosine profile such that the minimum DNBR occurs in the upper half of the hot channel. The deflections in minimum and maximum heat flux seen in Figure 5-6 are also reflected in the minimum and maximum DNBR profiles in Figure 5-7.

#### *Fuel Centerline Temperature*

The second selected FOM is maximum fuel temperature. Because this value occurs at the fuel centerline, a discussion is given regarding the observed fuel centerline temperature profile. Figure 5-8 presents fuel centerline temperature calculated by RELAP5-3D and VIPRE-01. The resulting fuel centerline temperature distributions yield nearly analogous forms. This further supports the conclusion made from Figure 4-7 that the gap modeling described by equation (4-20) is valid. Figure 5-8 shows that the fuel centerline temperature distribution follows a cosine shape. This is expected as the only nonuniform parameter affecting fuel centerline temperature is the axial power shape. This explains the deflections seen in the minimum and maximum temperature profiles, which are also seen in Figure 5-6.

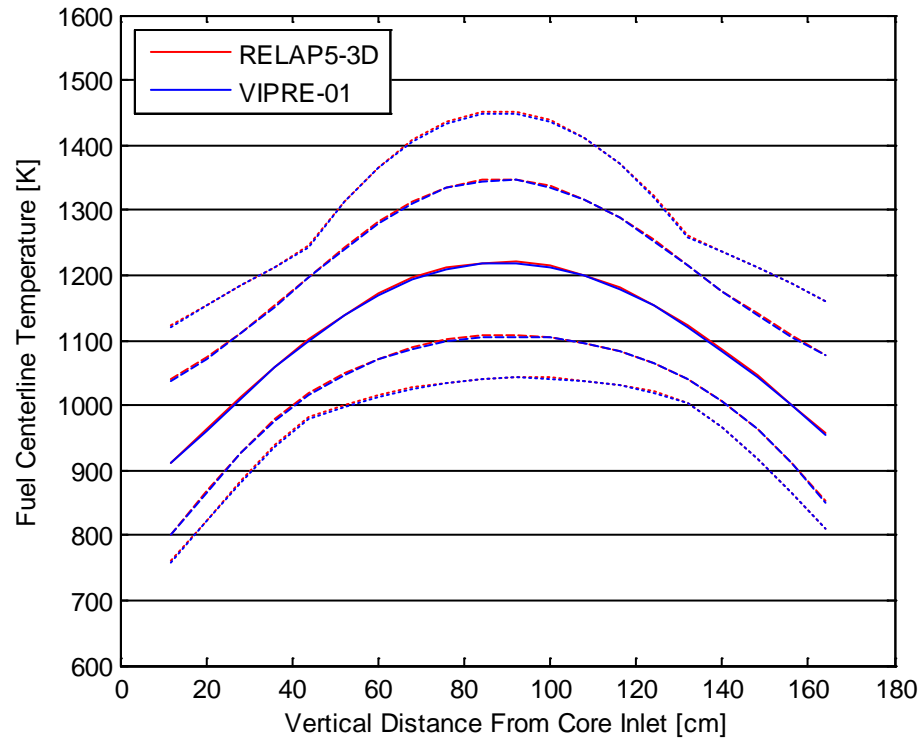


Figure 5-8: Fuel centerline temperature in the hot channel.

### *Clad Temperature*

The final FOM chosen in Chapter 4 is maximum clad temperature. The clad surface temperature profile is presented in order to better capture effects relating to the heat transfer coefficient between the clad and coolant. Figure 5-9 presents the clad surface temperature calculated by RELAP5-3D and VIPRE-01. In general the distributions are very similar between both codes, however, the cladding temperature in the lower region of the hot channel is predicted to be hotter in RELAP5-3D than that of VIPRE-01.

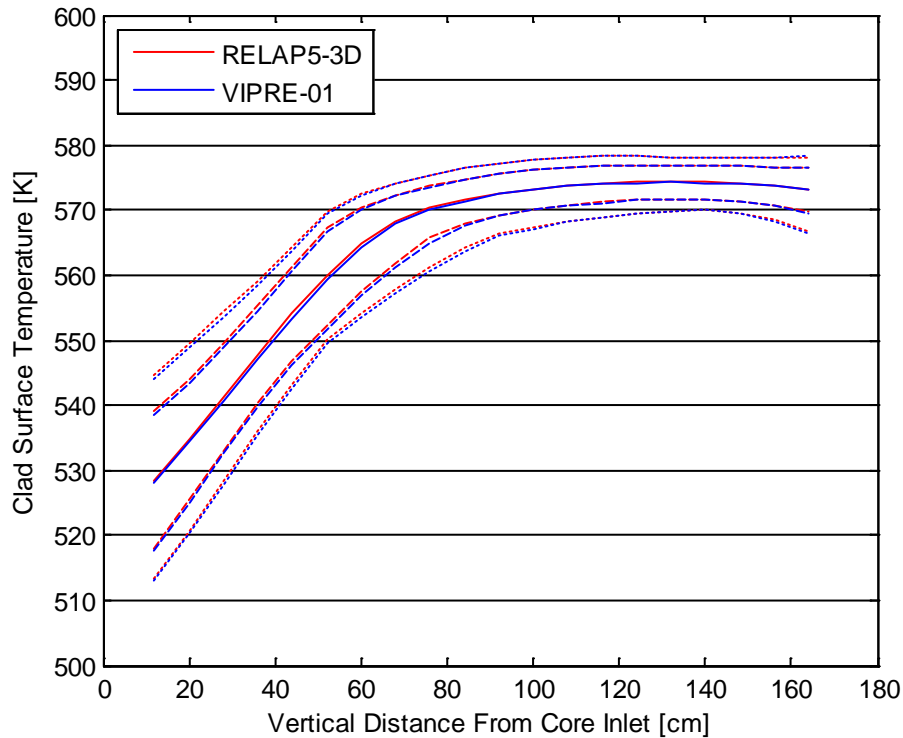


Figure 5-9: Clad surface temperature in the hot channel.

As with fuel centerline temperature, it is expected that Figure 5-9 would follow a cosine shape as the only parameter affecting clad surface temperature is the axial power shape. However after initially rising, clad surface temperature remains fairly constant in the upper half of the hot channel. This indicates the assumption that clad surface temperature is independent from other output variables is invalid. Clad surface temperature is also dependent upon the bulk coolant temperature distribution and the heat transfer coefficient between the clad and coolant. Because the pressure drop across the hot channel is relatively small, the rising equilibrium quality shown in Figure 5-5 indicates a continually rising bulk coolant temperature in the hot channel. However, the heat transfer coefficient also increases as the heat transfer regime changes from single-phase liquid to subcooled nucleate boiling at approximately 60 cm. These two facts, combined with decreasing heat flux past the axial centerline,

balance to yield a constant clad surface temperature in the upper half of the hot channel.

### Uncertainty Analysis Results

As discussed in Chapter 4, the selected FOMs for uncertainty analysis are MDNBR, maximum fuel temperature, and maximum clad temperature. For each of the 5000 data samples, the value of each FOM was taken as the respective minimum or maximum value seen at any axial location within the hot channel. For each FOM, an ECDF is plotted using equation (4-41). Lower and upper confidence bounds are plotted using equations (4-46) and (4-47) at the 95 percent confidence level.

#### *MDNBR*

As described above, an ECDF built from the MDNBR results calculated by RELAP5-3D and VIPRE-01 (Figure 5-10).

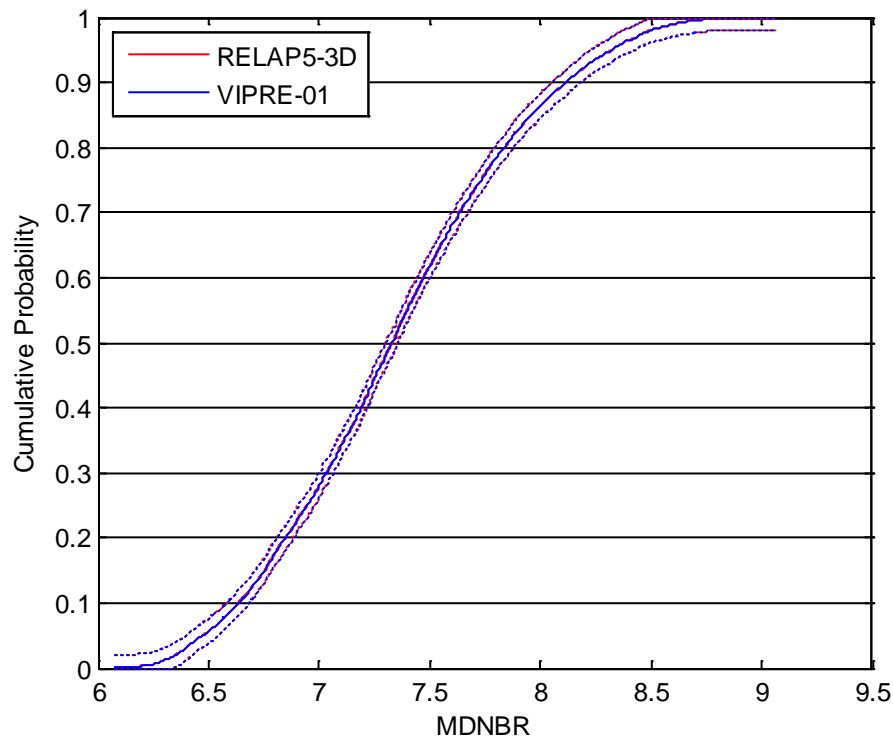


Figure 5-10: The MDNBR ECDF plot.

Figure 5-10 shows good agreement between the RELAP5-3D and VIPRE-01 results, as expected given the agreement shown in Figure 5-7. Key ECDF values, ignoring confidence intervals, are summarized in Table 5-1. The span between the 5<sup>th</sup> and 95<sup>th</sup> percentiles predicted by RELAP5-3D and VIPRE-01 is 1.855 and 1.854, respectively. This correlates to a percent difference between the 5<sup>th</sup> and 95<sup>th</sup> percentiles of 25.07 percent and 25.05 percent, respectively.

Table 5-1: MDNBR percentile values from 5000 samples.

Code	Min.	Percentile			Max.	Mean
		5 <sup>th</sup>	50 <sup>th</sup>	95 <sup>th</sup>		
RELAP5-3D	6.076	6.472	7.330	8.327	9.065	7.353
VIPRE-01	6.077	6.473	7.331	8.327	9.062	7.354

Acceptance criteria for MDNBR is taken from NUREG-800 Chapter 4.4, which states there should be a 95 percent probability at the 95 percent confidence level that the hot rod does not experience a DNB condition [34]. A DNB condition will occur whenever the MDNBR is less than 1.0. However, due to the uncertainty in the empirical correlations used to calculate CHF, additional margin above 1.0 is required. One common CHF correlation is the Westinghouse W-3 correlation, which has a minimum DNBR limit of 1.3 [16]. While a CHF correlation specific to the MASLWR design would likely have a different DNBR limit, a limit of 1.3 is applied in this study. To satisfy the statistical requirement in Chapter 4.4, MDNBR values are read from the upper bound of the 5<sup>th</sup> percentile in Figure 5-10. These values are 6.400 and 6.402 for RELAP5-3D and VIPRE-01 respectively. Because these values are greater than 1.3, the MASLWR design meets the DNBR safety requirement specified in NUREG-800 Chapter 4.4 given the parameter uncertainties evaluated in this study.

These MDNBR values are compared with those found in a large PWR plant, specifically the Westinghouse AP1000 design. For the AP1000, the MDNBR in a typical flow channel at nominal conditions is 2.80 [45]. While this value is approximately half that seen in Figure 5-10, it is recognized that this value was also

calculated using the Westinghouse WRB-2M CHF correlation. Unlike the generalized 2006 AECL CHF look-up table, the WRB-2M correlation was designed specifically for AP1000 fuel assemblies. Therefore, core power density is also compared. The MASLWR core volume is approximated as a cylinder with an active fuel height of 160.0 cm and radius of three assembly widths, or 64.4 cm. This yields a core power density of approximately 72 kW/L at a core thermal power of 150 MW. The AP1000 has a core power density of 109.7 kW/L at a core thermal power of 3400 MW [45]. The lower core power density seen in the MASLWR supports the higher MDNBR value compared to the AP1000.

#### *Maximum Fuel Temperature*

Maximum fuel temperature is the second evaluated FOM in this study. The maximum fuel temperature is taken as the highest fuel centerline temperature seen in the hot channel for each of the 5000 data samples. Figure 5-11 presents the ECDF of the maximum fuel temperature calculated by RELAP5-3D and VIPRE-01.

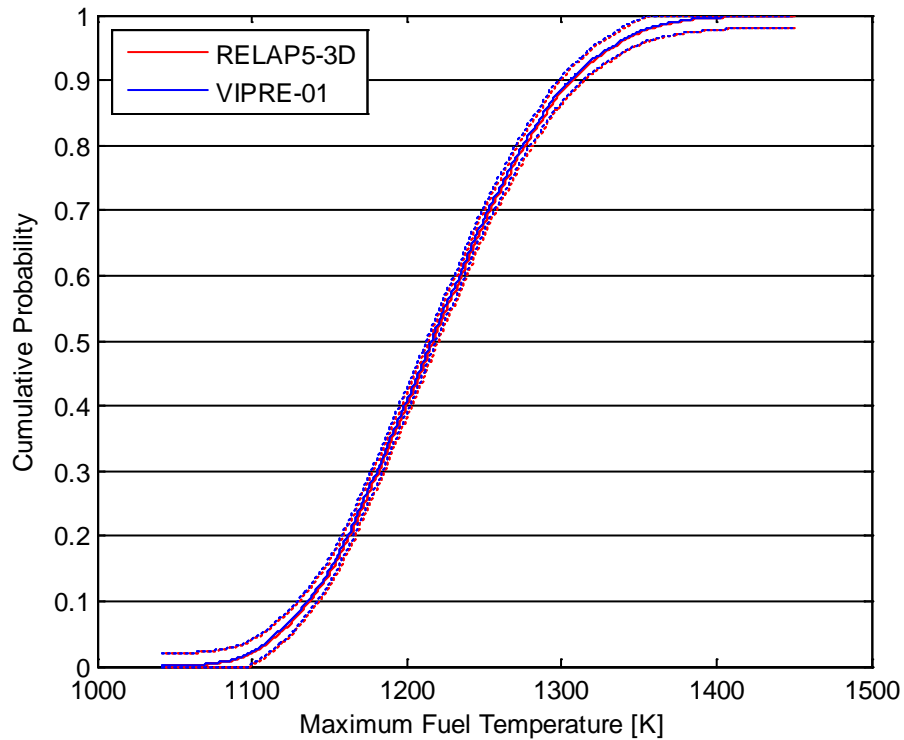


Figure 5-11: The maximum fuel temperature ECDF plot.

Figure 5-11 shows good agreement between the RELAP5-3D and VIPRE-01 calculations. This is expected given the agreement seen in Figure 5-8. Key ECDF values, ignoring confidence intervals, are summarized in Table 5-2. The span between the 5<sup>th</sup> and 95<sup>th</sup> percentiles predicted by RELAP5-3D and VIPRE-01 is 216.6 K and 216.7 K, respectively. This corresponds to a percent difference between the 5<sup>th</sup> and 95<sup>th</sup> percentiles of 17.67 percent and 17.70 percent, respectively.

Table 5-2: Maximum fuel temperature [K] percentile values from 5000 samples.

Code	Min.	Percentile			Max.	Mean
		5th	50th	95th		
RELAP5-3D	1044.4	1117.4	1217.3	1334.0	1450.6	1220.4
VIPRE-01	1042.5	1115.9	1216.0	1332.6	1449.3	1219.0

Acceptance criteria for maximum fuel temperature is taken from NUREG-800 Chapter 4.2, which prohibits fuel centerline melting during normal operation [33]. For LWR designs, the conservatively low fuel melting temperature of 2873 K is often used [27]. The 95 percent probability at the 95 confidence level is used to select maximum fuel temperature from Figure 5-11. This value is read from the lower bound of the 95<sup>th</sup> percentile. The RELAP5-3D and VIPRE-01 maximum fuel temperatures are 1347.3 K and 1345.6 K, respectively. Because these values are well below the 2873 K melting point, the MASLWR design satisfies the maximum fuel centerline temperature criteria established by NUREG-800 Chapter 4.2 given the parameter uncertainties evaluated in this study.

The MASLWR fuel centerline temperature is compared to temperatures seen in a typical PWR. From Figure 8.22 in [27], the typical fuel rod centerline temperature at a linear power rate of 16.4 kW/m is approximately 1116 K. The core average linear power rate in the MASLWR design is 14.8 kW/m. Despite having a lower linear power rate, examining Figure 5-8 shows much of the MASWR fuel centerline temperature distribution lies above the 1116 K value; furthermore, the average maximum fuel temperature from Table 5-2 is approximately 1220 K. This higher fuel centerline temperature is credited to the different flow rates between the MASLWR design and a typical PWR. As seen in Figure 5-3, the average mass flux through the hot channel is approximately 1030 kg/s-m<sup>2</sup>. From [27], the average subchannel mass flux for a 3400 MW PWR design is approximately 3800 kg/s-m<sup>2</sup>, over three times higher than the MASLWR. This higher mass flux results from the forced convection used in all large PWR designs.

#### *Maximum Clad Temperature*

Maximum clad temperature is the final FOM evaluated in this study. The maximum clad temperature is taken along the inner surface of the cladding and is tabulated through identification of the highest temperature exhibited on this surface for each of the 5000 data samples. Figure 5-12 presents the ECDF of the maximum clad temperature calculated by RELAP5-3D and VIPRE-01.

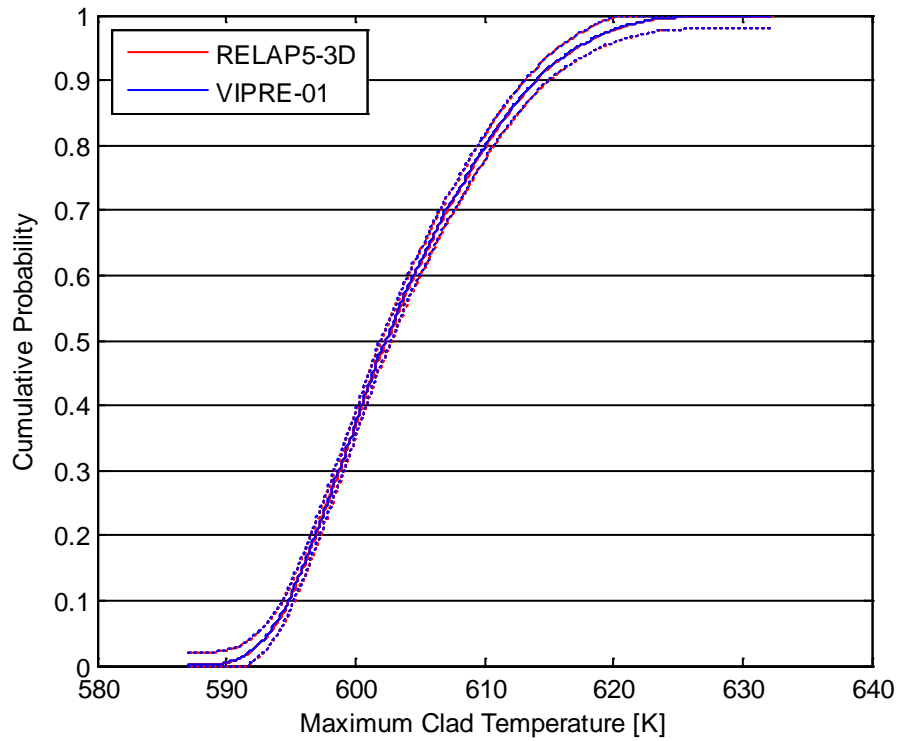


Figure 5-12: The maximum clad temperature ECDF plot.

Figure 5-12 shows good agreement between the RELAP5-3D and VIPRE-01 results. Key ECDF values, ignoring confidence intervals, are summarized in Table 5-3. The span between the 5<sup>th</sup> and 95<sup>th</sup> percentiles predicted by RELAP5-3D and VIPRE-01 is 24.0 K and 23.9 K, respectively. This corresponds to a percent difference between the 5<sup>th</sup> and 95<sup>th</sup> percentiles of 3.96 percent and 3.95 percent, respectively.

Table 5-3: Maximum clad temperatures [K] percentile values from 5000 samples.

Code	Min.	Percentile			Max.	Mean
		5th	50th	95th		
RELAP5-3D	587.1	593.3	602.4	617.3	632.3	603.6
VIPRE-01	587.1	593.3	602.4	617.2	632.2	603.5

Acceptance criteria for maximum clad temperature is taken from NUREG-800 Chapter 4.2, which requires the avoidance of clad overheating to prevent fuel failure during operation [33]. However, Chapter 4.2 also states that fuel failures associated with clad overheating will not occur as long as DNBR margin is satisfied. As previously discussed, evaluations made in this study show a DNB condition will not occur in the MASLWR core under steady state operation. Therefore, the clad temperature requirement is satisfied according to NUREG-800 Chapter 4.2.

Maximum clad temperature is of greater concern during a transient event, particularly a LOCA. In this event, clad temperature may increase rapidly due to the loss of cooling. If the zirconium cladding temperature rises too far (greater than 1477.6 K), then the cladding may undergo an exothermic reaction with water to form zirconium oxide and hydrogen gas [27]. To compare against this value, maximum clad temperatures were selected from Figure 5-12 as the lower bound of the 95<sup>th</sup> percentile. RELAP5-3D and VIPRE-01 maximum clad temperatures are determined as 619.0 K and 619.0 K, respectively. As expected for steady state operation, these values are much lower than the 1477.6 K limit.

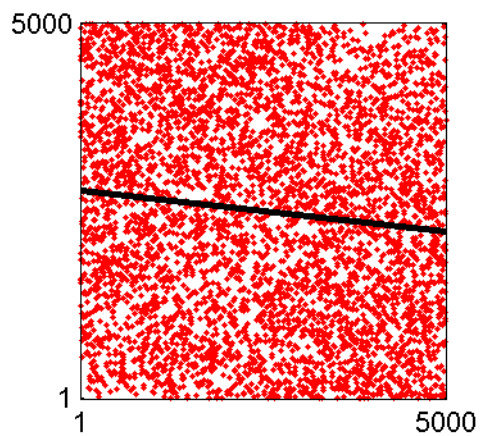
### **Sensitivity Analysis Results**

A sensitivity analysis was performed using the same FOM data set analyzed during uncertainty analysis. The sensitivity of each FOM to the 12 uncertain parameters listed in Table 4-6 and Table 4-7 was determined. Scatter plots are presented using rank transformed data, with one representing the smallest value and 5000 the largest value in a data set. The PRCCs and  $p$ -values are calculated using the "partialcorr" function from the MATLAB Statistics Toolbox package. The PRCCs describe how much influence each parameter has on the uncertainty in a FOM relative to one another. The  $p$ -values are used to provide a context for whether or not a parameter has a statistically significant influence on a FOM. It is emphasized that these  $p$ -values are limited to the range of uncertainty assigned to each input parameter, that is, a change in the evaluated uncertainty range will change the calculated  $p$ -values. If a parameter has a

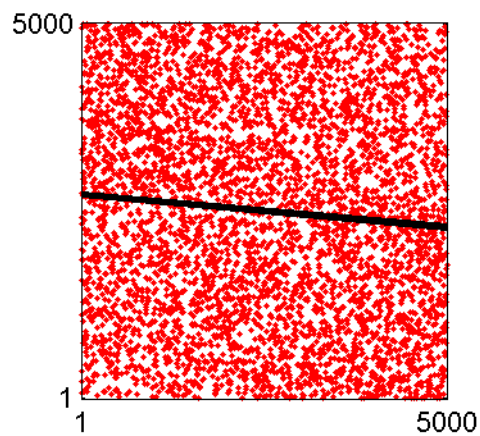
$p$ -value  $< 0.05$ , then that parameter is said to have a statistically significant influence on the corresponding FOM [42]. Neither the PRCC nor  $p$ -value indicate the magnitude of change a FOM will experience given a perturbation in the uncertain parameter. Finally, each parameter's relative influence is ranked based on the absolute value of its PRCC value. A rank of one indicates that parameter has the highest influence on a FOM and rank 12 indicates the lowest influence.

#### *MDNBR*

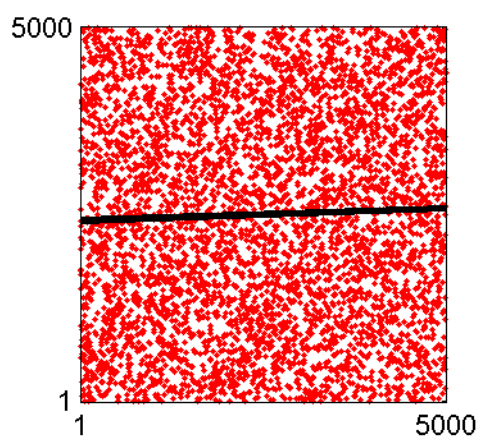
The minimum departure from nucleate boiling ratio is taken as the smallest DNBR value seen in the hot channel for each of the 5000 data samples. Sensitivity scatter plots for RELAP5-3D and VIPRE-01 are presented in Figure 5-13 and Figure 5-14, respectively.



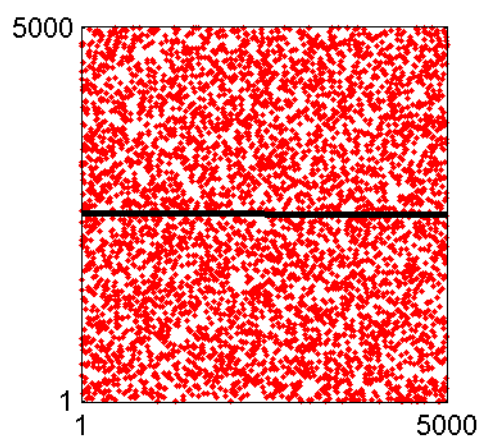
(a) Power



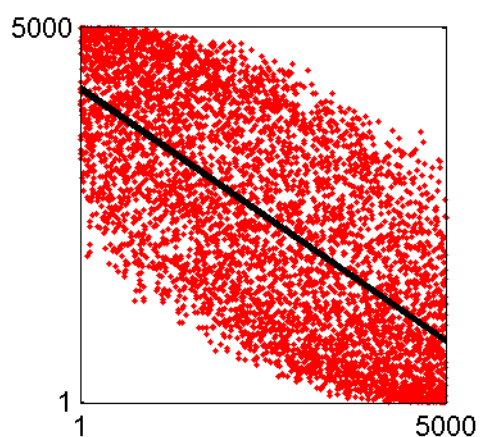
(b) Pressure



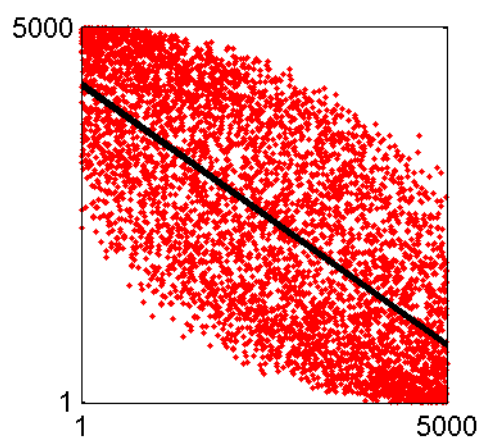
(c) System Flow



(d) Inlet Temperature



(e) Radial Power Factor



(f) Axial Power Factor

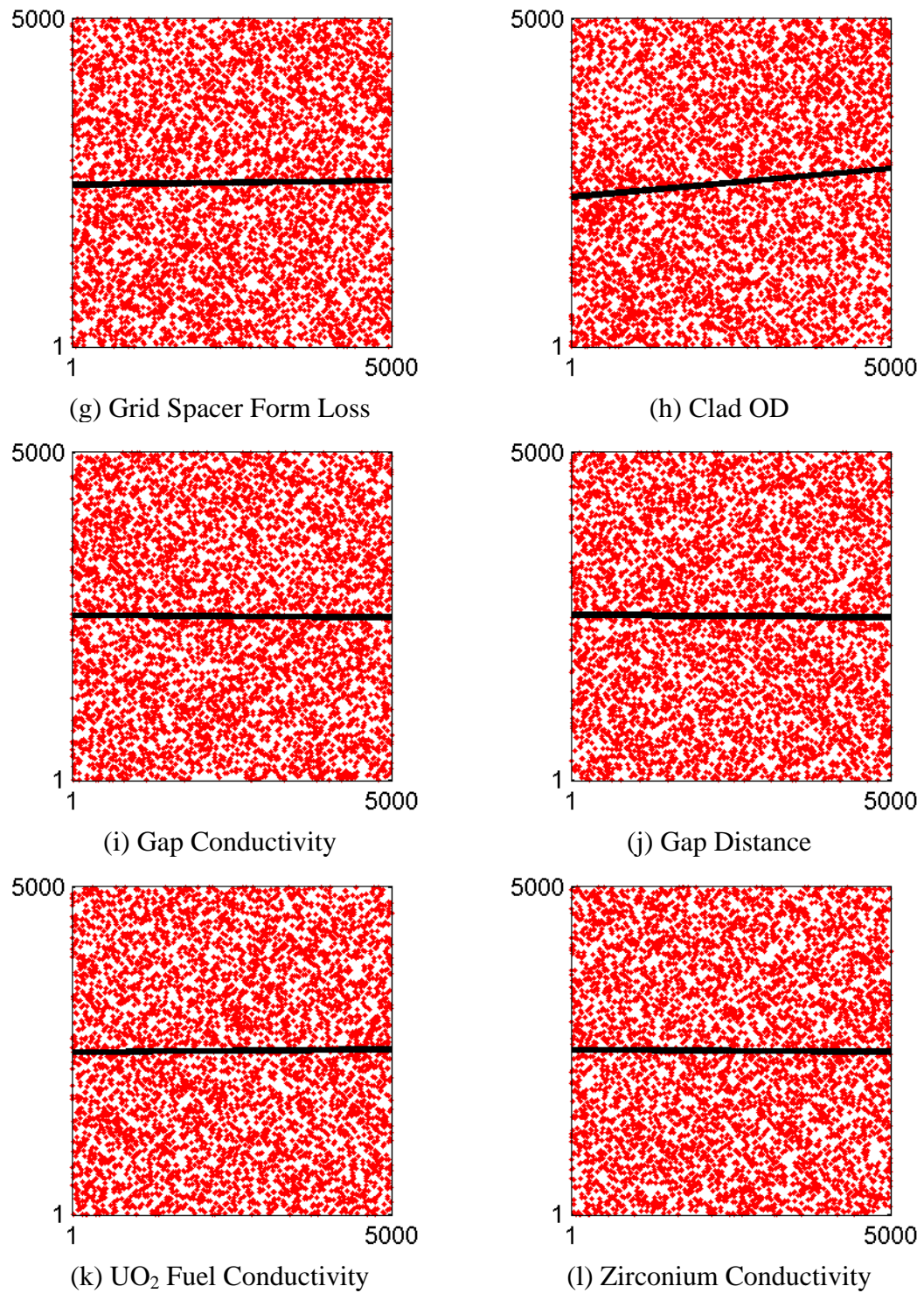
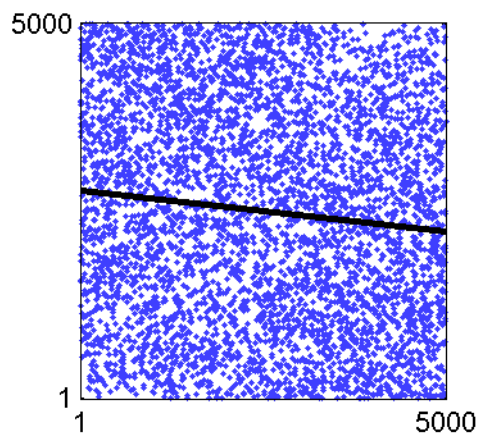
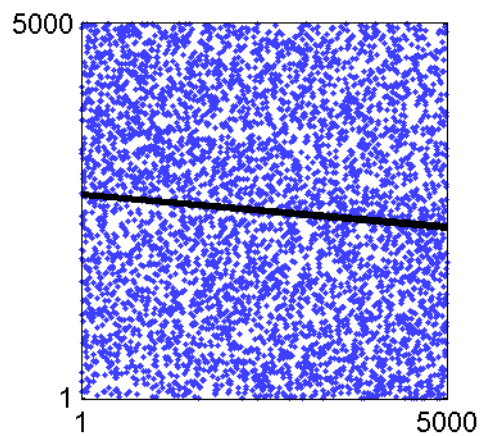


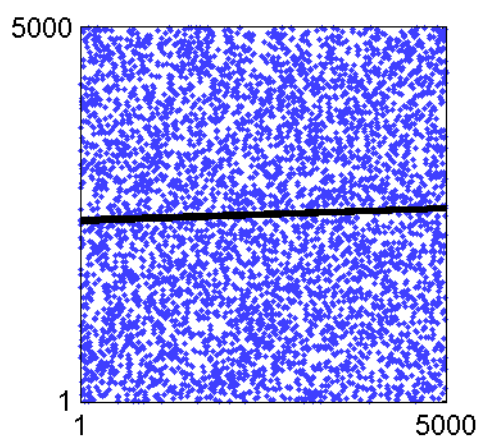
Figure 5-13: RELAP5-3D MDNBR ranked sensitivity plots.



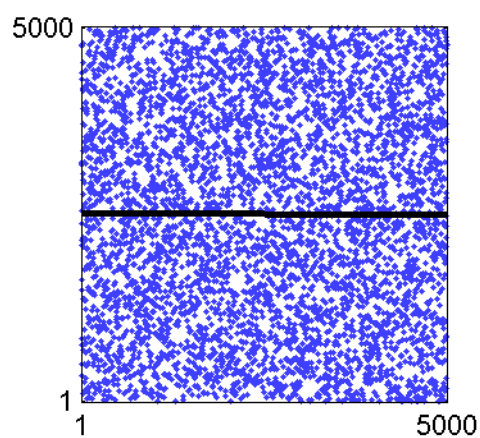
(a) Power



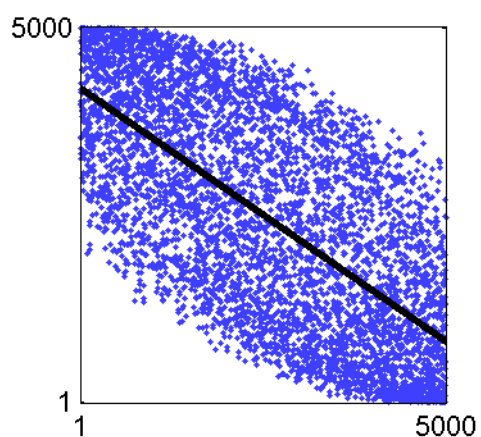
(b) Pressure



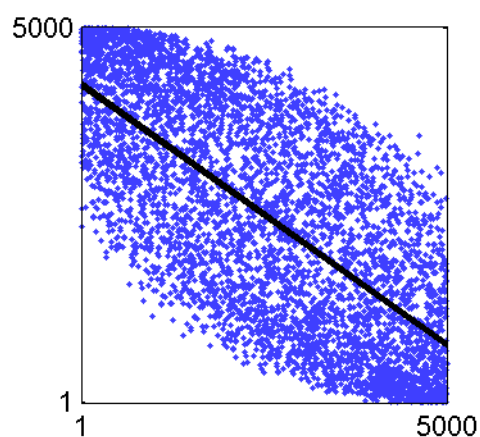
(c) System Flow



(d) Inlet Temperature



(e) Radial Power Factor



(f) Axial Power Factor

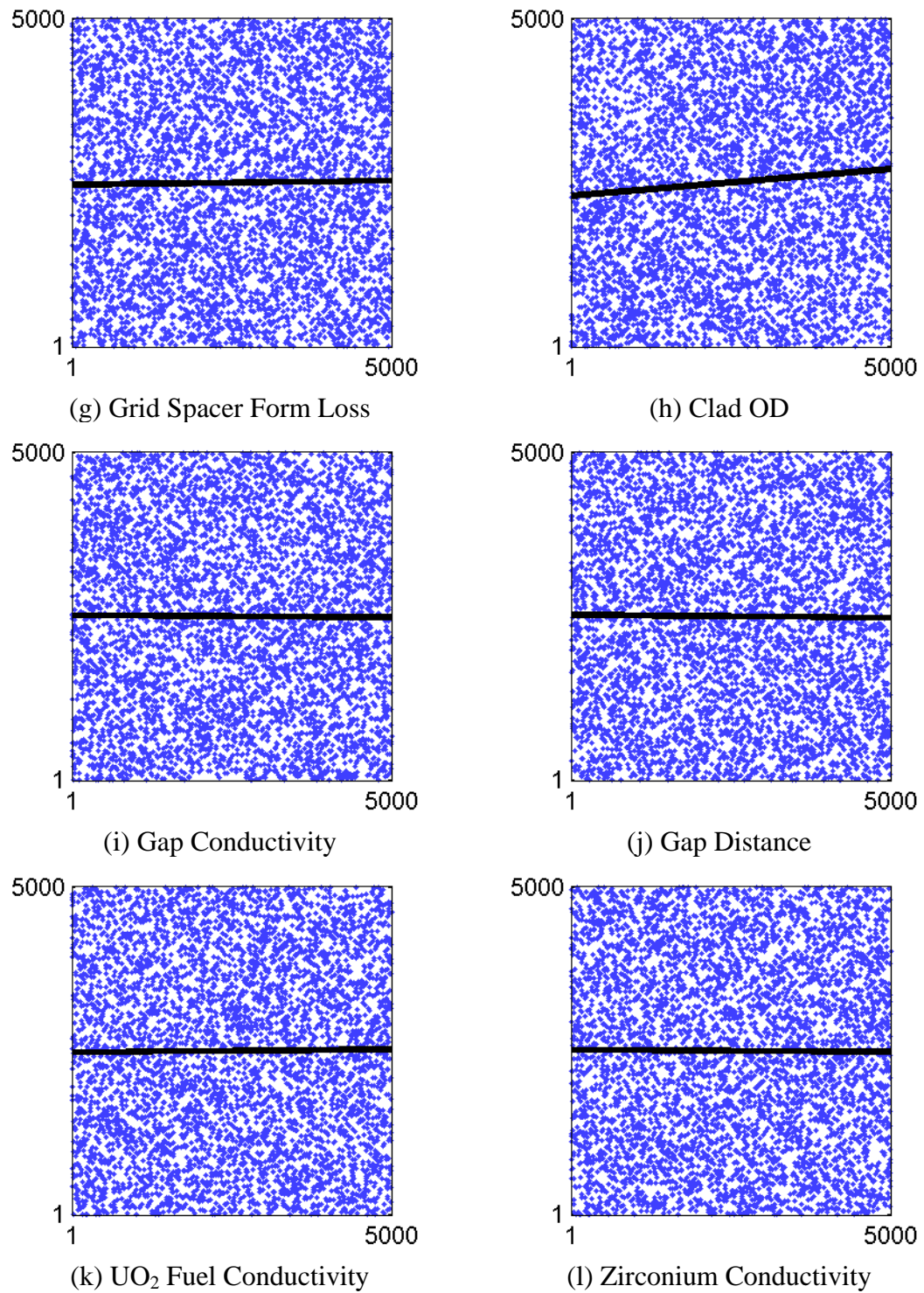


Figure 5-14: VIPRE-01 MDNBR ranked sensitivity plots.

Examining Figure 5-13 and Figure 5-14 show both codes indicate the axial power factor and radial power factor have a strong influence on MDNBR. These two parameters effect the local heat flux distribution seen in the hot channel. Equation (4-35) shows that local heat flux is directly used to calculate DNBR. Additionally, the axial and radial power factors have a larger range of uncertainty relative to that of other influential parameters. Therefore, the high influence the axial and radial power factors have on MDNBR is expected. The PRCCs,  $p$ -values, and rank of each parameter against MDNBR are shown in Table 5-4.

Table 5-4: MDNBR sensitivity analysis results.

Parameter	RELAP5-3D			VIPRE-01		
	PRCC	$p$ -value	Rank	PRCC	$p$ -value	Rank
Power	-0.893	< 0.05	3	-0.893	< 0.05	3
Pressure	-0.825	< 0.05	4	-0.824	< 0.05	4
System Flow	0.339	< 0.05	7	0.341	< 0.05	7
Inlet Temperature	-0.518	< 0.05	6	-0.522	< 0.05	6
Radial Power Factor	-0.996	< 0.05	2	-0.996	< 0.05	2
Axial Power Factor	-0.996	< 0.05	1	-0.996	< 0.05	1
Grid Spacer Form Loss	-0.017	0.23	9	-0.017	0.22	9
Clad OD	0.708	< 0.05	5	0.681	< 0.05	5
Gap Conductivity	-0.009	0.54	10	-0.007	0.60	10
Gap Distance	0.005	0.72	12	0.004	0.76	12
UO <sub>2</sub> Fuel Conductivity	-0.018	0.19	8	-0.017	0.22	8
Zirconium Conductivity	-0.007	0.60	11	-0.007	0.62	11

Table 5-4 confirms that the axial and radial power factors have the highest influence on MDNBR. Core power and system pressure are shown to be the 3<sup>rd</sup> and 4<sup>th</sup> most influential parameters on MDNBR. Core power also affects local heat flux, but on a global scale. System pressure has a direct impact on local pressure, which is used to calculate local CHF in equation (4-36).

Clad OD, inlet temperature, and system flow are the 5<sup>th</sup>, 6<sup>th</sup>, and 7<sup>th</sup> most influential parameters respectively. Clad OD is another parameter which affects local heat flux. Inlet temperature and system flow have a direct impact on equilibrium quality and mass flux in the hot channel. Because these two quantities are used to calculate local CHF in equation (4-36), inlet temperature and system flow are expected to influence MDNBR.

The remaining parameters have a  $p$ -value  $> 0.05$  and are interpreted as having no significant influence on MDNBR relative to the parameters discussed above. It is noted that the  $p$ -value reflects grid spacer influence on a global scale. As RELAP5-3D and VIPRE-01 are lumped parameter codes, it is difficult to capture the localized effect grid spacers may have on MDNBR. Finally, gap conductivity, gap distance, UO<sub>2</sub> conductivity, and zirconium conductivity do not impact local heat flux at steady state conditions. Therefore, these parameters are expected to have no influence on MDNBR.

#### *Maximum Fuel Temperature*

The maximum fuel temperature is taken as the highest fuel centerline temperature seen in the hot channel for each of the 5000 data samples. Sensitivity scatter plots for RELAP5-3D and VIPRE-01 are presented in Figure A-10 and Figure A-11 respectively. The PRCCs,  $p$ -values, and rank of each parameter against maximum fuel temperature are shown in Table 5-5.

Table 5-5: Maximum fuel temperature sensitivity analysis results.

Parameter	RELAP5-3D			VIPRE-01		
	PRCC	p-value	Rank	PRCC	p-value	Rank
Power	0.771	$< 0.05$	6	0.771	$< 0.05$	6
Pressure	0.160	$< 0.05$	9	0.155	$< 0.05$	9
System Flow	-0.015	0.28	11	-0.017	0.23	11
Inlet Temperature	0.137	$< 0.05$	10	0.143	$< 0.05$	10
Radial Power Factor	0.991	$< 0.05$	3	0.991	$< 0.05$	3
Axial Power Factor	0.991	$< 0.05$	2	0.991	$< 0.05$	2
Grid Spacer Form	-0.006	0.69	12	-0.006	0.68	12

Loss						
Clad OD	0.225	< 0.05	8	0.224	< 0.05	8
Gap Conductivity	-0.720	< 0.05	7	-0.723	< 0.05	7
Gap Distance	0.975	< 0.05	4	0.976	< 0.05	4
UO <sub>2</sub> Fuel Conductivity	-0.992	< 0.05	1	-0.992	< 0.05	1
Zirconium Conductivity	-0.809	< 0.05	5	-0.810	< 0.05	5

Table 5-5 shows the most influential parameter on maximum fuel temperature is UO<sub>2</sub> conductivity. This is expected as the UO<sub>2</sub> conductivity directly affects the ability to conduct thermal energy from the fuel centerline to the outer fuel pellet surface. The 2<sup>nd</sup> and 3<sup>rd</sup> most influential parameters are the axial and radial power factors. As with MDNBR, these two parameters control local power generation within the hot channel.

The 4<sup>th</sup>, 5<sup>th</sup>, and 7<sup>th</sup> most influential parameters are gap distance, zirconium conductivity, and gap conductivity. These parameters all affect the cumulative thermal resistance between the fuel pellet and the coolant. The 6<sup>th</sup> most influential parameter is system power, which affects heat generation within the hot channel on a global scale.

The 8<sup>th</sup>, 9<sup>th</sup>, and 10<sup>th</sup> most influential parameters are clad OD, system pressure, and system inlet temperature respectively. These parameters have significantly smaller PRCC values than the first seven most influential parameters, but still have  $p$ -values < 0.05. Clad OD affects the thermal resistance between the fuel pellet and the clad surface. System pressure and system inlet temperature affect the heat transfer coefficient from the clad surface to the coolant. With the exception of system power, it is noted that clad OD, system pressure, and system inlet temperature have relatively small ranges of uncertainty compared to the other more influential parameters.

System flow and the grid spacers will affect the mass flux through the hot channel and thus affect the heat transfer between the clad surface and the coolant. However with  $p$ -values > 0.05, the uncertainty in maximum fuel temperature caused by system flow

and the grid spacer loss coefficient is statistically insignificant relative to the effect of the remaining ten parameters.

#### *Maximum Clad Temperature*

The maximum clad temperature is taken as the highest clad inner wall temperature seen in the hot channel for each of the 5000 data samples. Sensitivity scatter plots for VIPRE-01 and RELAP5-3D are presented in Figure A-12 and Figure A-13 respectively. The PRCCs,  $p$ -values, and rank of each parameter against maximum clad temperature are shown in Table 5-6.

Table 5-6: Maximum clad temperature sensitivity analysis results.

Parameter	RELAP5-3D			VIPRE-01		
	PRCC	p-value	Rank	PRCC	p-value	Rank
Power	0.299	< 0.05	8	0.300	< 0.05	8
Pressure	0.528	< 0.05	5	0.521	< 0.05	5
System Flow	-0.061	< 0.05	9	-0.063	< 0.05	9
Inlet Temperature	0.346	< 0.05	6	0.347	< 0.05	6
Radial Power Factor	0.876	< 0.05	2	0.878	< 0.05	2
Axial Power Factor	0.839	< 0.05	3	0.839	< 0.05	3
Grid Spacer Form Loss	-0.001	0.96	12	0.000	0.99	12
Clad OD	0.659	< 0.05	4	0.656	< 0.05	4
Gap Conductivity	-0.003	0.85	11	-0.003	0.85	11
Gap Distance	-0.308	< 0.05	7	-0.308	< 0.05	7
UO <sub>2</sub> Fuel Conductivity	-0.019	0.18	10	-0.018	0.19	10
Zirconium Conductivity	-0.977	< 0.05	1	-0.977	< 0.05	1

Table 5-6 shows the most influential parameter on maximum fuel temperature is the zirconium clad conductivity. This is expected as the zirconium conductivity directly affects the ability to conduct thermal energy from the inner clad surface to the outer clad surface. The 2<sup>nd</sup> and 3<sup>rd</sup> most influential parameters are the radial and axial power factors. As before, these two parameters control local power generation within the hot channel.

The 4<sup>th</sup>, 5<sup>th</sup>, and 6<sup>th</sup> most influential parameters are clad OD, system pressure, and inlet temperature respectively. Clad OD changes the distance from the inner clad surface to the outer clad surface. This in turn affects the total thermal resistance between the inner clad surface and the outer clad surface. System pressure and inlet temperature both affect the subcooled nucleate boiling heat transfer coefficient between the clad and coolant calculated via the Chen correlation.

The 7<sup>th</sup> most influential parameter is gap distance. At steady state conditions, the inner clad surface temperature depends only on the thermal resistance network between the inner surface and the coolant. Therefore, it is expected that gap distance would have no influence on the maximum clad temperature. However, in the geometric model used in this study, gap distance also affects the inner clad radius. This in turn changes the clad thickness and thus the total thermal resistance to the coolant. This highlights the need to understand any interdependencies which may exist between parameters.

The 8<sup>th</sup> and 9<sup>th</sup> most influential parameters are power and system flow. As before, the system power affect heat generation within the hot channel on a global scale. System flow affects the mass flux through the hot channel, and thus impacts the heat transfer coefficient between the clad and coolant. It is noted that the PRCC between system flow and maximum clad temperature is significantly smaller than the remaining influential parameters.

With  $p$ -values  $> 0.05$ ,  $\text{UO}_2$  conductivity, gap conductivity, and grid spacer loss coefficient have no statistically significant effect on maximum clad temperature relative to the other parameters. As previously discussed,  $\text{UO}_2$  conductivity and gap conductivity do not affect the thermal resistance between the inner clad surface and coolant at steady-state conditions. Therefore, these parameters are not expected to influence maximum clad temperature. Given the relatively little impact grid spacers have on the mass flux in the hot channel, the grid spacer loss coefficient is not expected to significantly influence maximum clad temperature.

## 6. CONCLUSIONS

This study was performed to increase confidence in the thermal hydraulic safety analysis of a new reactor design through the application of uncertainty and sensitivity analysis methods. To fulfill this purpose, an uncertainty and sensitivity analysis methodology was developed and demonstrated through RELAP5-3D Version 4.0.3 and VIPRE-01 Mod 2.2.1. Several observations can be drawn from the successful application of this methodology.

### **Observations**

First, in order to facilitate an impartial comparison between the RELAP5-3D and VIPRE-01 results, an effort was made to reduce any bias caused by the deployment of the MASLWR core model itself. Differences between the RELAP5-3D and VIPRE-01 models, specifically gap conduction, were shown to cause no bias in the final results. This claim is further supported by the overall good agreement seen between RELAP5-3D and VIPRE-01 during uncertainty and sensitivity analysis. Furthermore, it was demonstrated that differences in hot channel flow rate resulted from calculations internal to RELAP5-3D and VIPRE-01 and not the employed MASLWR model.

Knowing that any differences in results stem from the RELAP5-3D and VIPRE-01 codes themselves, a valid comparison of the uncertainty associated with each selected FOM can be made. It was shown that the RELAP5-3D and VIPRE-01 predicted hot channel MDNBR, maximum fuel temperature, and maximum clad temperature are in good agreement. Furthermore, the predicted MDNBR, maximum fuel temperature, and maximum clad temperature satisfy the acceptance criteria found in NUREG-800 under the input parameter uncertainty ranges evaluated in this study. This supports the statement that the MASLWR design is safely operable at steady state conditions.

Finally, to give further insight into the uncertainty results discussed above, several observations can be made regarding the sensitivity of each uncertain parameter on the

selected FOMs. First, it is noted that the radial and axial power shapes have a high influence on all three FOMs. This is attributed to the fact that these parameters control the magnitude of the local phenomena which dictate each FOM response. Additionally, these two parameters have been assigned a relatively large range of uncertainty compared to the remaining inputs. It is also noted that certain parameters which are highly influential on some FOMs have little impact on other FOMs. These facts highlight the importance of assigning accurate uncertainty ranges to each input parameter. This also demonstrates the value of evaluating many uncertain parameters at once, versus limiting the number of parameters as done in the RS uncertainty analysis method.

### **Limitations & Assumptions**

The following limitations and assumptions should be considered when weighing the previously stated observations. First, the evaluated range of uncertainty assigned to each parameter will dictate the final uncertainty and sensitivity analysis results. Many of the parameter ranges used in this study come from sources relating to large NPPs. While these ranges are considered suitable because they reflect actual uncertainties in an operating NPP, it is recognized that uncertainties specific to the MASLWR would be different. Second, the MASLWR core model used in this study has been developed with the intention of reducing modeling bias between RELAP5-3D and VIPRE-01. Such models would require validation against experimental data before the presented FOM values could be considered best estimate results. Finally, evidence in the results points to the existence of interdependencies between both the input parameters and output quantities. The methodology employed in this study assumed such interdependencies did not exist.

### **Future Work**

This study was intended as the first attempt to characterize uncertainty in the subchannel analysis of the MASLWR core. Future studies should include:

- Input parameter uncertainty ranges validated for the MASLWR design.

- Correlations to account for the interdependencies visible between both the input parameters and the output quantities.
- Inclusion of additional uncertainty and sensitivity analysis metrics, such as those found in the U.S. NRC's State-of-the-Art Reactor Consequence Analysis (SOARCA) project [46].

## BIBLIOGRAPHY

1. Cleveland, J. (2005, November). *Overview of Global Development of Advanced Nuclear Power Plants*. IAEA, Natural circulation in water cooled power plants, Annex 1. IAEA-TECDOC-1474.
2. Modro S. M., Fisher, J. E., Weaver, K. D., Reyes, J. N., Groome, J. T., Babka, P., & Carlson, T. M. (2003, December). *Multi-Application Small Light Water Reactor Final Report*. Idaho National Engineering and Environmental Laboratory.
3. Helton, J. C., Johnson, J. D., Sallaberry, C. J., & Storlie, C. B. (2006). Survey of Sampling-Based Methods for Uncertainty and Sensitivity Analysis. Sandia National Laboratories, SAND2006-2901.
4. U.S. Nuclear Regulatory Commission. (1989, May). *Best-Estimate Calculations of Emergency Core Cooling System Performance*. Regulatory Guide 1.157
5. Mai, A. T. (2011, December). *Thermal Hydraulic and Fuel Performance Analysis for Innovative Small Light Water Reactor Using VIPRE-01 and FRAPCON-3*. Oregon State University.
6. Technical Program Group. (1989, December). *Quantifying Reactor Safety Margins*. NUREG/CR-5249.
7. Frepoli, C. (2008). *An Overview of Westinghouse Realistic Large Break LOCA Evaluation Model*. Science and Technology of Nuclear Installations, vol. 2008.
8. Martin, R., & O'Dell, L. (2005). *AREVA's realistic large break LOCA analysis methodology*. Nuclear Engineering and Design, 235(16).

9. Briggs, L. L. (2008, September). *Uncertainty Quantification Approaches for Advanced Reactor Analysis*. Argonne National Laboratory, Nuclear Engineering Division.
10. Nuclear Energy Agency. (2007, October). *BEMUSE Phase III Report, Uncertainty and Sensitivity Analysis of the LOFT L2-5 Test*.
11. Wilks, S. S. (1941). *Determination of Sample Sizes for Setting Tolerance Limits*. The Annals of Mathematical Statistics, 12(1).
12. Wilks, S. S. (1942). Statistical Prediction with Special Reference to the Problem of Tolerance Limits. *The Annals of Mathematical Statistics*, 13(4).
13. Glaeser, H. (2008). *GRS Method for Uncertainty and Sensitivity Evaluation of Code Results and Applications*. Science and Technology of Nuclear Installations, vol. 2008.
14. Hallee, B. T. (2013, March). *Feed-and-Bleed Transient Analysis of OSU APEX Facility using the Modern Code Scaling, Applicability, and Uncertainty Method*. Oregon State University.
15. Luo, H. (2012, November). *Quantified PIRT and Uncertainty Quantification for Computer Code Validation*. Oregon State University
16. Lloyd, M. W., & Feltus, M. A. (1995). *Statistical Core Design Methodology Using The VIPRE Thermal-Hydraulics Code*. Ann. Nucl. Energy, 22(8).
17. Ostle, B., & Mensing, R. (1975). *Statistics in Research*. 3rd edition, Chap. 5. Iowa State University Press.
18. Marcum, W. R., Woods, B. G., & Reese, S. R. (2010). *Experimental and theoretical comparison of fuel temperature and bulk coolant characteristics in the Oregon State TRIGA reactor during steady state operation*. Nuclear Engineering and Design, 240.

19. Galvin, M. R. (2009). *System Model of a Natural Circulation Integral Test Facility*. Oregon State University.
20. Mascari, F., Vella, G., Woods, B. G., & Auria, F. D. (2012). *Analyses of the OSU-MASLWR Experimental Test Facility*. Science and Technology of Nuclear Installations, vol. 2012.
21. Reyes, J. N., Groome, J., Woods, B. G., Young, E., Abel, K., Yao, Y., & Yoo, Y.J. (2007). *Testing of the Multi-Application Small Light Water Reactor (MASLWR) Passive Safety Systems*. Nuclear Engineering and Design, Vol. 237, Issue 18, pp. 1999-2005.
22. Soldatov, A. (2009, March). *Design and Analysis of a Nuclear Reactor Core for Innovative Small Light Water Reactors*. Oregon State University.
23. Wuth, B. J. (2014). *Comparative Analysis of the Zukauskas Method and Data from the OSU MASLWR Test Facility Steam Generator*. Oregon State University.
24. VIPRE-01 Team. (2001). *Volume 1: Mathematical Modeling*. Electric Power Research Institute.
25. VIPRE-01 Team. (2001). *Volume 2: User Manual*. Electric Power Research Institute.
26. VIPRE-01 Team. (1988). *Volume 5: Guidelines*. Electric Power Research Institute.
27. Todreas, N., & Kazimi, M. (2012). *Nuclear Systems: Thermal Hydraulic Fundamentals* (Second., Vol. 1). CRC Press.
28. Dittus, F.W., & Boelter, L. M. K. (1930). *Heat Transfer in Automobile Radiators of the Tubular Type*. University of California, Berkely. Publ. Eng., 2:443-461.

29. Chen, J. C. (1966). *A correlation for boiling heat transfer in convection flow*. ISEC Process Des. Dev., 5:322.
30. Geelhood, K. J., Luscher, W. G., Beyer, C. E., Senor, D. J., Cunningham, M. E., Lanning, D. D., & Adkins, H. E. (2009). *Predictive Bias and Sensitivity in NRC Fuel Performance Codes*. NUREG/CR-7001.
31. RELAP5-3D Code Development Team. (2012). *RELAP5-3D Code Manual Volume I: Code Structure, System Models and Solution Methods*. Idaho National Laboratory.
32. RELAP5-3D Code Development Team. (2012). *RELAP5-3D Code Manual Volume V: User's Guidelines*. Idaho National Laboratory.
33. NUREG-800, (2007) *U.S. Nuclear Regulatory Commission Standard Review Plan, Chapter 4.2 Fuel System Design*.
34. NUREG-800, (2007) *U.S. Nuclear Regulatory Commission Standard Review Plan, Chapter 4.4 Thermal and Hydraulic Design*.
35. Code of Federal Regulations Chapter 10 Part 50, (2014) *Appendix A to Part 50 - General Design Criteria for Nuclear Power Plants*.
36. Groeneveld, D. C., Shan, J. Q., Vasic, A. Z., Leung, L. K. H., Durmayaz, A., Yang, J., Cheng, S.C., Tanase, A. (2007). *The 2006 CHF look-up table*. Nuclear Engineering and Design, Volume 237, Issues 15-17, Pages 1909–1922.
37. International Atomic Energy Agency. (2002). *Accident Analysis for Nuclear Power Plants*. Safety Report Series No. 23.
38. Virginia Electric and Power Company. (2005). *North Anna Power Station Units 1 and 2 Proposed Technical Specification Changes Addition of Analytical Methodology to COLR*. NRC ADAMS Public Document ML051890034.

39. Vijayan, P.K., & Nayak, A.K. (2005, November). *Experimental Validation and Data Base of Simple Loop Facilities*. IAEA, Natural circulation in water cooled power plants, Annex 13. IAEA-TECDOC-1474.
40. Lefebvre, M. (2006). *Applied Probability and Statistics*. Springer.
41. Lee, S.W., Chung, B. D., Bang, Y., Bae, S. W., (2014, August). *Analysis of Uncertainty Quantification Method by Comparing Monte-Carlo method and Wilks' Formula*. Nuclear Engineering and Technology, Volume 46, No. 4.
42. Montgomery, D. C., Runger, G. C., & Hubele, N. F. (2007). *Engineering Statistics* (Fourth.). John Wiley & Sons, Inc.
43. Wasserman, L. (2006). *All of Nonparametric Statistics*. Springer.
44. Saltelli, A., Chan, K., & Scott, E. M. (2000). *Sensitivity Analysis*. John Wiley & Sons, Inc.
45. Westinghouse. (2007). *AP1000 Design Control Document Rev. 16*. NRC ADAMS Public Document ML071580898.
46. Draft NUREG/CR-7155. *State-of-the-Art Reactor Consequence Analyses Project: Uncertainty Analysis of the Unmitigated Long-Term Station Blackout of the Peach Bottom Atomic Power Station*. ADAMS Public Document ML13189A145.

## NOMENCLATURE

## Symbols

$A$	Flow cross sectional area.
$A_c$	Cross flow cross sectional area.
$A_r$	Surface area at radius $r$ .
$c(x_j, y)$	Partial correlation coefficient between $x_j$ and $y$ .
$D_G$	Outside diameter of the guide tube.
$D_H$	Hydraulic diameter.
$D_R$	Outside diameter of the fuel rod.
$\varepsilon_n$	Dvoretzky-Kiefer-Wolfowitz error term.
$erfc(x)$	Complementary error function.
$f$	Turbulent wall friction factor.
$f(x)$	Probability distribution function.
$f_G$	Total fraction of guide tubes
$f_H$	Horizontal pitch length fraction.
$f_P$	Total fraction of fuel rod pitch.
$f_R$	Total fraction of fuel rods.
$f_{sub}$	Total fraction of a single subchannel.
$f_V$	Vertical pitch length fraction.
$F(x)$	Cumulative distribution function.
$\hat{F}_n(x)$	Empirical cumulative distribution function.
$F_{hot}$	Desired radial power factor in the hot channel.
$F_R$	Radial power factor.
$F_Z$	Axial power factor.
$G$	Mass flux.
$G_l$	Local mass flux.
$h$	Heat transfer coefficient.
$h_f$	Saturated fluid enthalpy.
$h_g$	Saturated vapor enthalpy.
$h_l$	Local fluid enthalpy.
$k$	Thermal conductivity.
$K$	Grid spacer form loss coefficient.
$K_G$	Recommended later flow resistance.
$K_i$	Lateral flow resistance at connection $i$ .
$L$	Length.

$L(x)$	Empirical CDF lower confidence band.
$L_C$	Centroid distance.
$L_G$	Gap width.
$L_{volume}$	Length of an axial volume.
$\mu$	Fluid dynamic viscosity.
$N$	Number of data samples.
$N_i$	Rod rows between channel centroids at connection $i$ .
$\Delta p$	Pressure loss.
$\phi_R$	Radial power profile.
$\phi_Z$	Axial power profile.
$p_{val}$	$p$ -value.
$P$	Fuel rod pitch.
$P_{c,wet}$	Wetted perimeter of cross flow connection.
$P_{heat}$	Heated perimeter.
$P_l$	Local fluid pressure.
$P_R$	Power generated in a fuel rod.
$P_{R,avg}$	Core average power generated in a fuel rod.
$P_Z$	Power generated within an axial volume.
$P_{Z,avg}$	Rod average axial volume power generation.
$P_{wet}$	Wetted perimeter.
$q''_{CHF}$	Local critical heat flux.
$q''_{local}$	Local heat flux.
$q_r$	Heat transfer in radial direction.
$\rho$	Fluid density.
$r$	Radial axis.
$R$	Radius of the core.
$Re$	Reynolds number.
$T$	Temperature.
$U(x)$	Empirical CDF upper confidence band.
$V_m$	Mean (mass weighted) fluid velocity.
$x_j$	Input parameter of interest.
$x_p$	Remaining input parameters.
$X_l$	Local equilibrium quality.
$y$	Output variable of interest.
$z$	Vertical axis.

## Acronyms

ADS	Automatic Depressurization System
AOO	Anticipated Operational Occurrence
ATWS	Anticipated Transient without Scram
CDF	Cumulative Distribution Function
CHF	Critical Heat Flux
CSAU	Code Scaling, Applicability, and Uncertainty
DKW	Dvoretzky-Kiefer-Wolfowitz
DNB	Departure from Nucleate Boiling
DNBR	Departure from Nucleate Boiling Ratio
DOE	Department of Energy
ECCS	Emergency Core Cool System
ECDF	Empirical Cumulative Distribution Function
EPRI	Electric Power Research Institute
FOM	Figure of Merit
GDC	General Design Criteria
HEU	Highly Enriched Uranium
IAEA	International Atomic Energy Association
ID	Inner Diameter
LEU	Low Enriched Uranium
LOCA	Loss-of-Coolant Accident
LWR	Light Water Reactor
MASLWR	Multi Application Small Light Water Reactor
MDNBR	Minimum Departure from Nucleate Boiling Ratio
NERI	Nuclear Energy Research Initiative
NPP	Nuclear Power Plant
NRC	Nuclear Regulatory Commission
OD	Outer Diameter
OSTR	Oregon State TRIGA Reactor
OSU	Oregon State University

PDF	Probability Distribution Function
PRCC	Partial Ranked Correlation Coefficient
PSSCDM	Pennsylvania State Statistical Core Design Methodology
PWR	Pressurized Water Reactor
RPV	Reactor Pressure Vessel
RS	Response Surface
SAFDL	Specified Acceptable Fuel Design Limit
SG	Steam Generator
SMR	Small Modular Reactor
SOARCA	State-of-the-Art Reactor Consequence Analysis
SRS	Simplified Random Sampling

## APPENDIX A (SUPPLEMENTARY INFORMATION)

**Flow Channel Type Diagrams**

Diagrams showing geometry of each channel type are provided for clarity. A typical 17x17 PWR fuel assembly is shown. The highlighted section shows the specific channel geometry being modeled by each channel type. This geometry is common to every flow channel of that type regardless of the actual channel location within the fuel assembly.

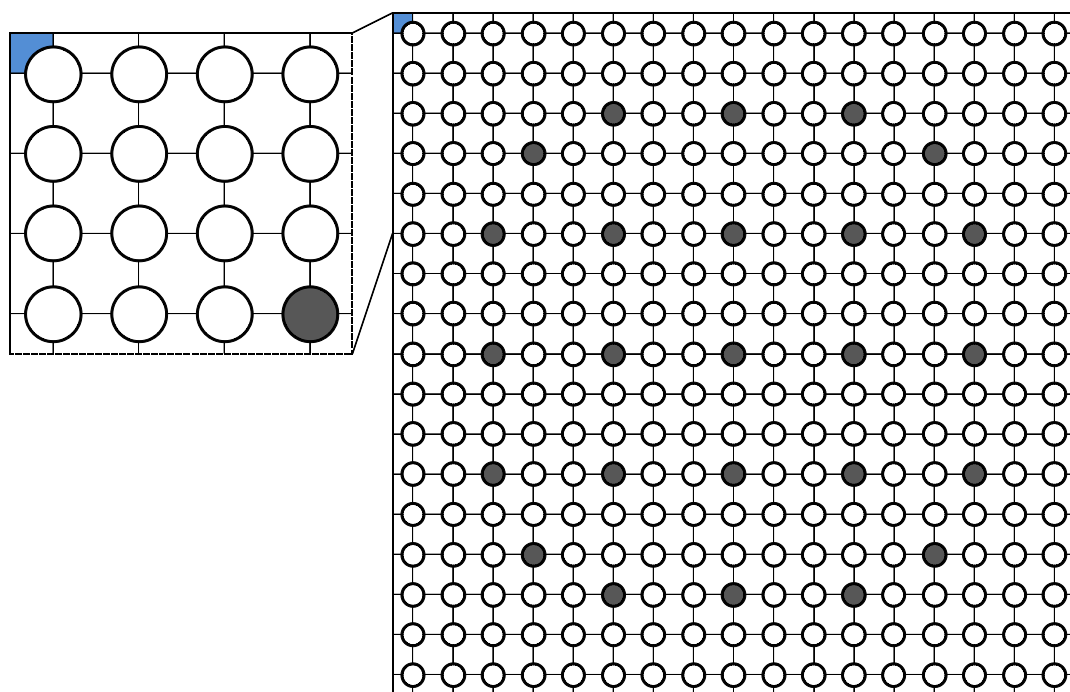


Figure A-1: Flow channel type 1; channel at assembly corner.

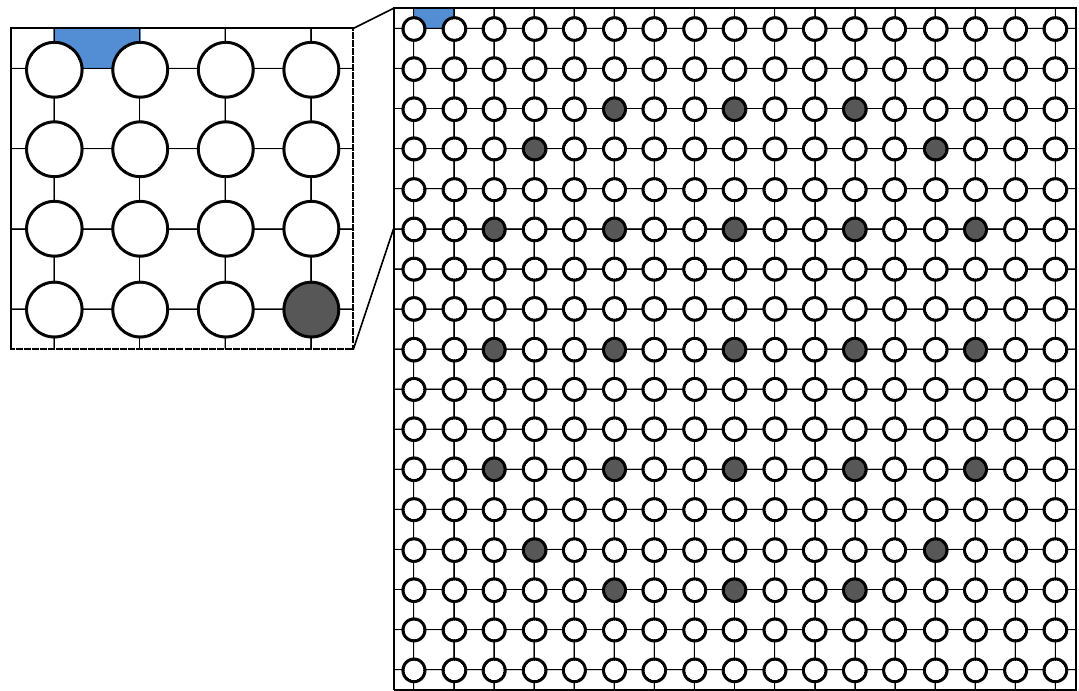


Figure A-2: Flow channel type 2; channel at assembly edge.

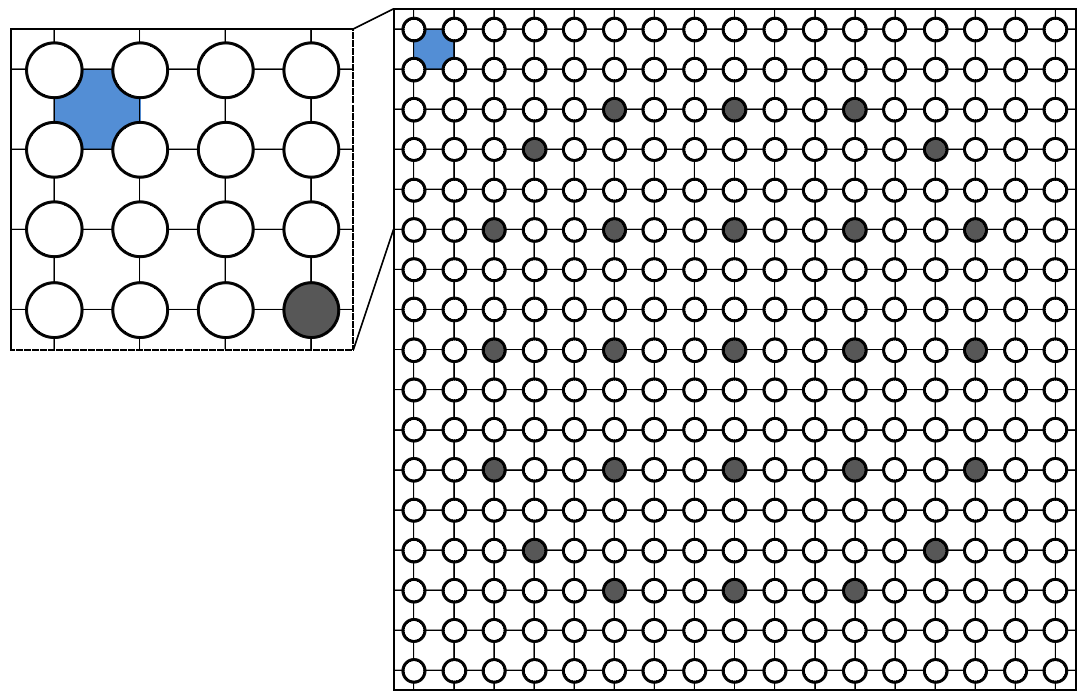


Figure A-3: Flow channel type 3; square subchannel with no guide tube.

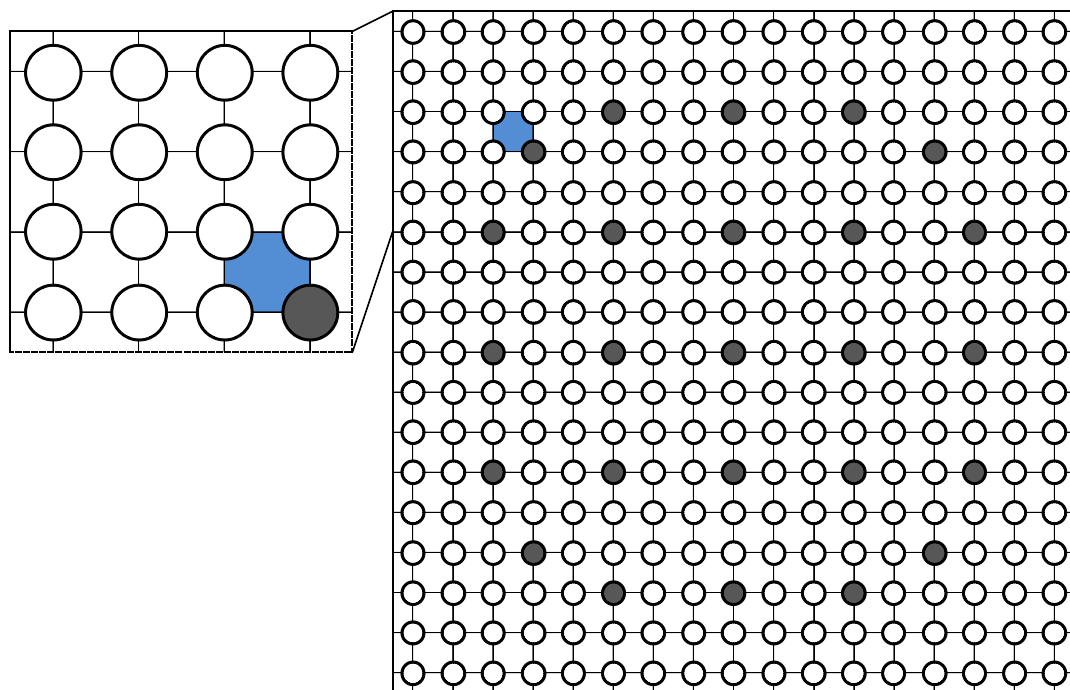


Figure A-4: Flow channel type 4; square subchannel with guide tube.

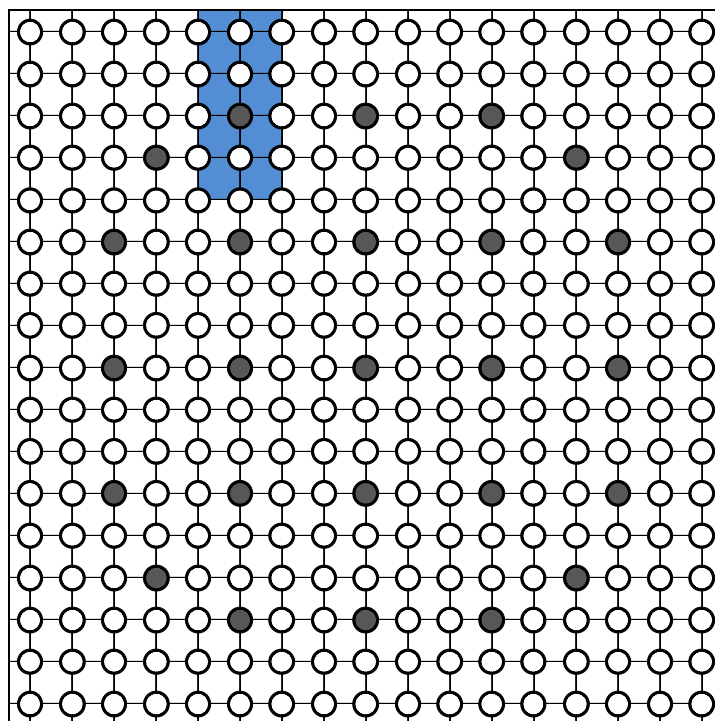


Figure A-5: Flow channel type 5; lumped 2x5 channel.

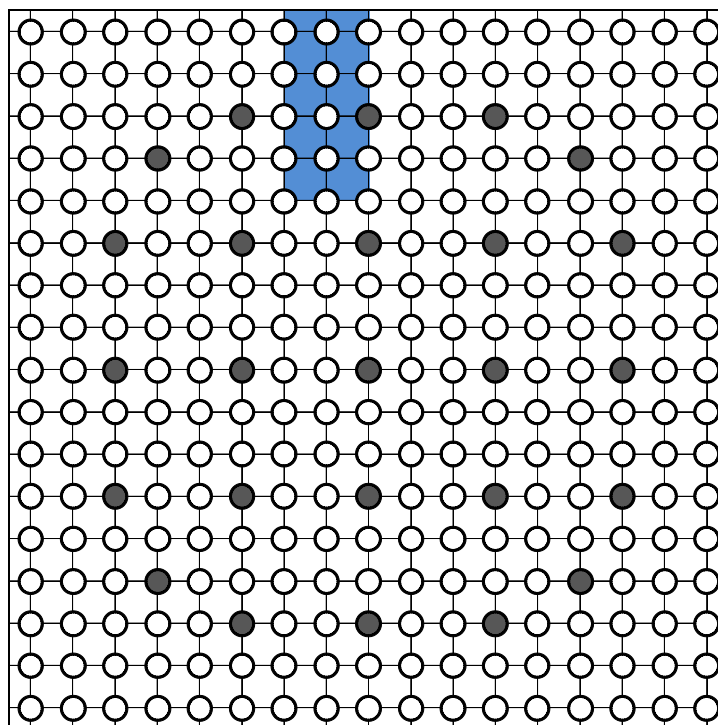


Figure A-6: Flow channel type 6; lumped 2x5 channel.

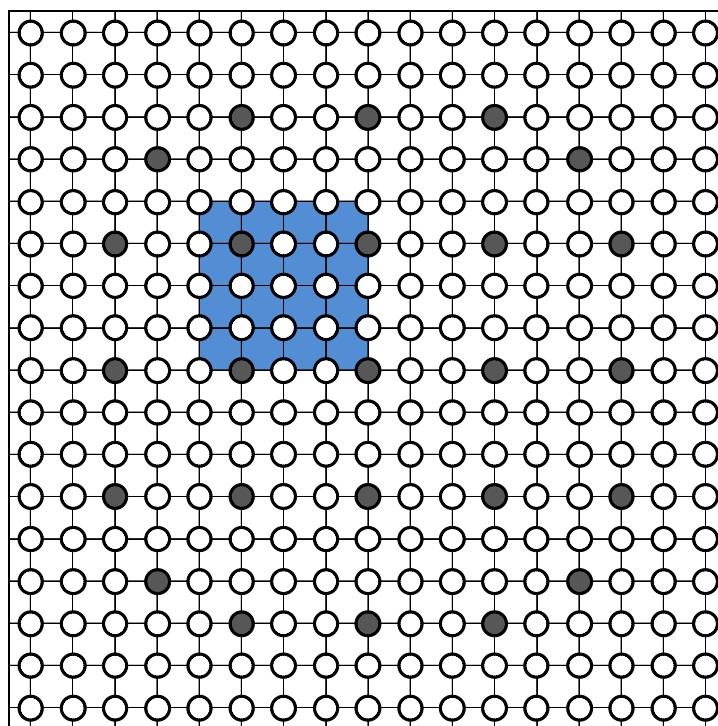


Figure A-7: Flow channel type 7; lumped 4x4 channel.

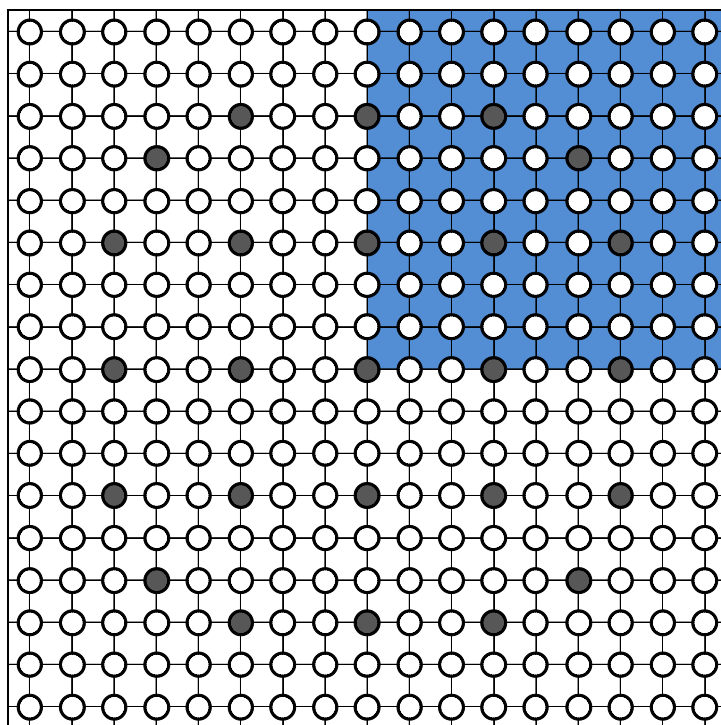


Figure A-8: Flow channel type 8; lumped one-quarter assembly.

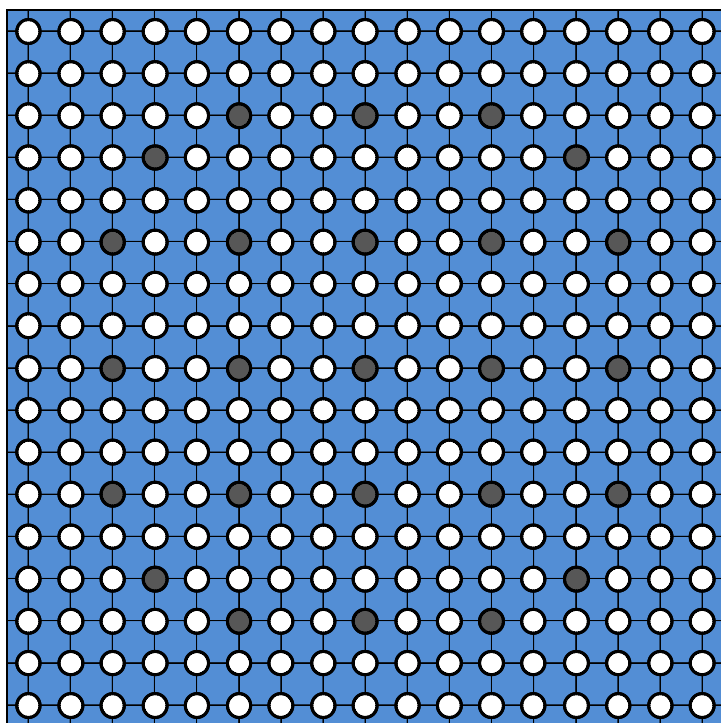


Figure A-9: Flow channel type 9; lumped full assembly.

### Cross Flow Geometry

The MASLWR core model described in Chapter 4 features 70 different crossflow paths. These paths allow transverse crossflow between adjacent subchannels. A detailed description of these paths is presented in Table A-1.

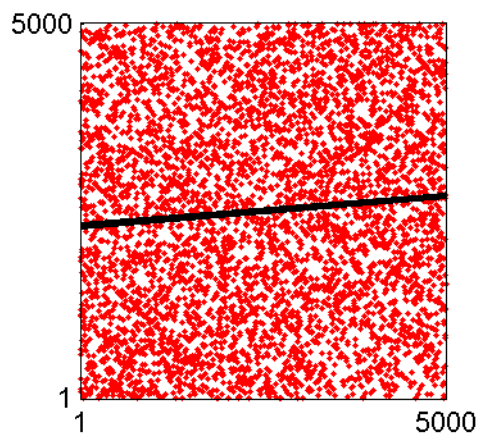
Table A-1: Cross flow path descriptions.

Gap Number	From Channel	To Channel	$K_i$	$f_P$	$f_R$	$f_G$	$f_H$	$f_V$
1	1	2	0.5	0.5	0.5	0.0	1.0	0.0
2	1	6	0.5	0.5	0.5	0.0	0.0	1.0
3	2	3	0.5	0.5	0.5	0.0	1.0	0.0
4	2	7	0.5	1.0	1.0	0.0	0.0	1.0
5	3	4	0.5	0.5	0.5	0.0	1.0	0.0
6	3	8	0.5	1.0	1.0	0.0	0.0	1.0
7	4	5	0.5	0.5	0.5	0.0	1.0	0.0
8	4	9	0.5	1.0	1.0	0.0	0.0	1.0
9	5	10	0.5	1.0	1.0	0.0	0.0	1.0
10	5	26	1.3	0.5	0.5	0.0	1.5	2.0
11	6	7	0.5	1.0	1.0	0.0	1.0	0.0
12	6	11	0.5	0.5	0.5	0.0	0.0	1.0
13	7	8	0.5	1.0	1.0	0.0	1.0	0.0
14	7	12	0.5	1.0	1.0	0.0	0.0	1.0
15	8	9	0.5	1.0	1.0	0.0	1.0	0.0
16	8	13	0.5	1.0	1.0	0.0	0.0	1.0
17	9	10	0.5	1.0	1.0	0.0	1.0	0.0
18	9	14	0.5	1.0	1.0	0.0	0.0	1.0
19	10	15	0.5	1.0	1.0	0.0	0.0	1.0
20	10	26	0.9	1.0	1.0	0.0	1.5	1.0
21	11	12	0.5	1.0	1.0	0.0	1.0	0.0
22	11	16	0.5	0.5	0.5	0.0	0.0	1.0
23	12	13	0.5	1.0	1.0	0.0	1.0	0.0
24	12	17	0.5	1.0	1.0	0.0	0.0	1.0
25	13	14	0.5	1.0	1.0	0.0	1.0	0.0
26	13	18	0.5	1.0	1.0	0.0	0.0	1.0
27	14	15	0.5	1.0	1.0	0.0	1.0	0.0
28	14	19	0.5	1.0	1.0	0.0	0.0	1.0
29	15	20	0.5	1.0	1.0	0.0	0.0	1.0
30	15	26	0.8	1.0	1.0	0.0	1.5	0.0
31	16	17	0.5	1.0	1.0	0.0	1.0	0.0

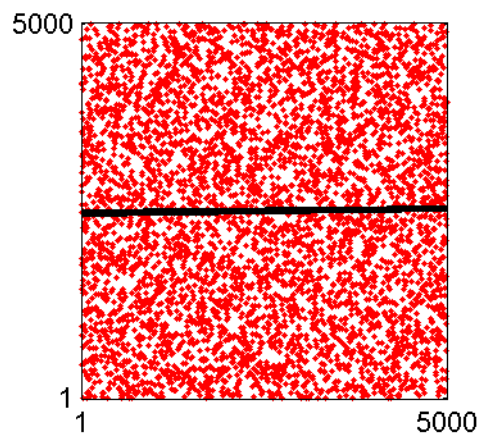
32	16	21	0.5	0.5	0.5	0.0	0.0	1.0
33	17	18	0.5	1.0	1.0	0.0	1.0	0.0
34	17	22	0.5	1.0	1.0	0.0	0.0	1.0
35	18	19	0.5	1.0	1.0	0.0	1.0	0.0
36	18	23	0.5	1.0	1.0	0.0	0.0	1.0
37	19	20	0.5	1.0	0.5	0.5	1.0	0.0
38	19	24	0.5	1.0	0.5	0.5	0.0	1.0
39	20	25	0.5	1.0	0.5	0.5	0.0	1.0
40	20	26	0.9	1.0	1.0	0.0	1.5	1.0
41	21	22	0.5	1.0	1.0	0.0	1.0	0.0
42	21	27	1.3	0.5	0.5	0.0	2.0	1.5
43	22	23	0.5	1.0	1.0	0.0	1.0	0.0
44	22	27	0.9	1.0	1.0	0.0	1.0	1.5
45	23	24	0.5	1.0	1.0	0.0	1.0	0.0
46	23	27	0.8	1.0	1.0	0.0	0.0	1.5
47	24	25	0.5	1.0	0.5	0.5	1.0	0.0
48	24	27	0.9	1.0	1.0	0.0	1.0	1.5
49	25	26	1.3	1.0	1.0	0.0	1.5	2.0
50	25	27	1.3	1.0	1.0	0.0	2.0	1.5
51	26	28	1.0	4.5	4.5	0.0	2.0	0.0
52	26	30	2.3	2.0	2.0	0.0	1.0	4.5
53	27	29	1.0	4.5	4.5	0.0	0.0	2.0
54	27	30	2.3	2.0	2.0	0.0	4.5	1.0
55	28	30	2.3	2.0	2.0	0.0	1.0	4.5
56	28	31	2.9	4.5	3.5	1.0	5.5	2.0
57	29	30	2.3	2.0	2.0	0.0	4.5	1.0
58	29	32	2.9	4.5	3.5	1.0	5.5	2.0
59	30	31	3.5	4.5	2.5	1.5	6.5	2.5
60	30	32	3.5	4.5	2.5	1.5	2.5	6.5
61	31	33	4.5	8.5	6.0	2.5	0.0	9.0
62	31	34	6.6	8.5	8.5	0.0	12.5	4.5
63	32	33	4.5	8.5	6.0	2.5	9.0	0.0
64	32	36	6.6	8.5	8.5	0.0	4.5	12.5
65	33	34	6.6	8.5	8.5	0.0	12.5	4.5
66	33	36	6.6	8.5	8.5	0.0	4.5	12.5
67	34	35	8.5	17.0	17.0	0.0	17.0	0.0
68	34	37	8.5	17.0	17.0	0.0	0.0	17.0
69	36	37	8.5	17.0	17.0	0.0	17.0	0.0
70	36	38	8.5	17.0	17.0	0.0	0.0	17.0

### **Sensitivity Analysis Scatter Plots**

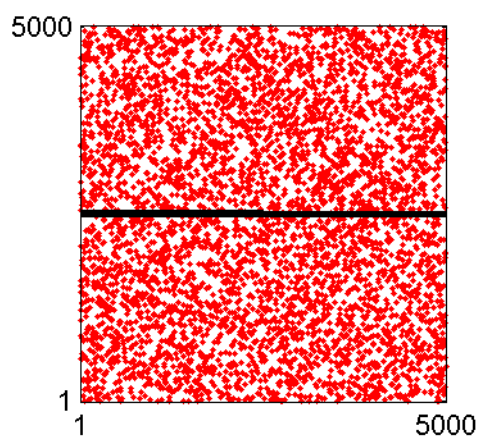
Sensitivity scatter plots are presented for maximum fuel temperature and maximum clad temperature using rank transformed data ranging from one to 5000. RELAP5-3D results are presented in red while VIPRE-01 results are presented in blue. Each subplot shows the correlation between the given FOM and a single uncertain input parameter.



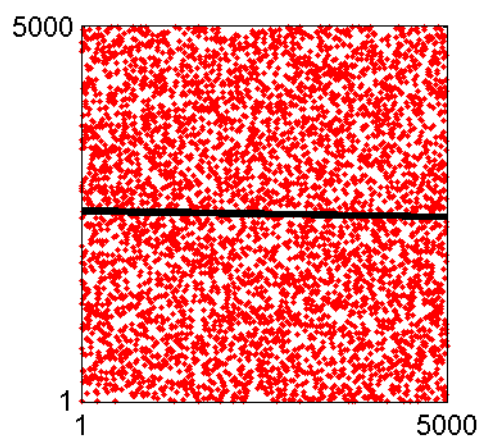
(a) Power



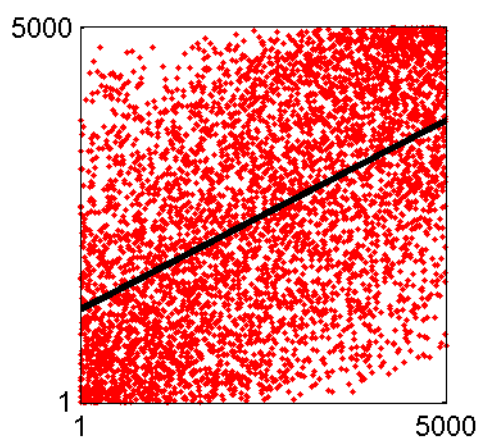
(b) Pressure



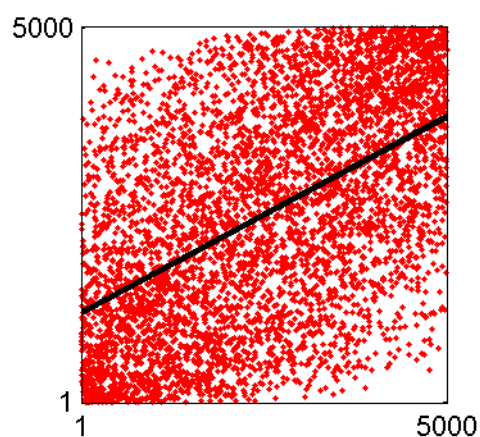
(c) System Flow



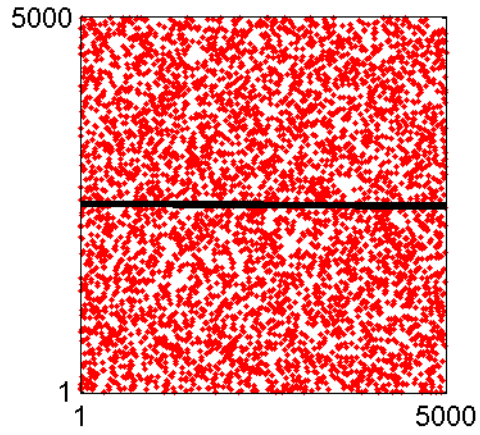
(d) Inlet Temperature



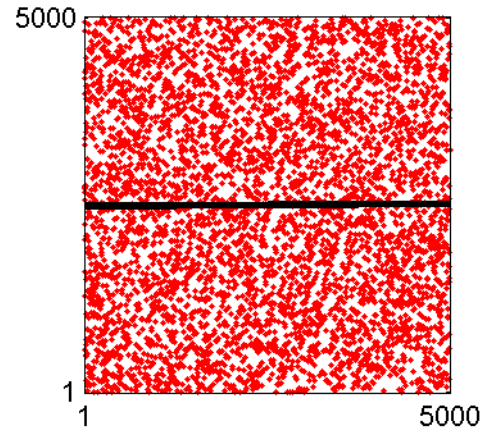
(e) Radial Power Factor



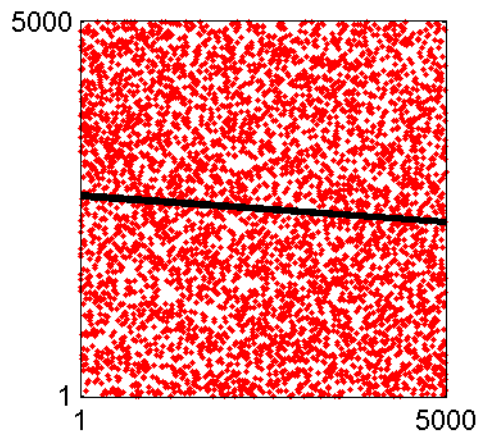
(f) Axial Power Factor



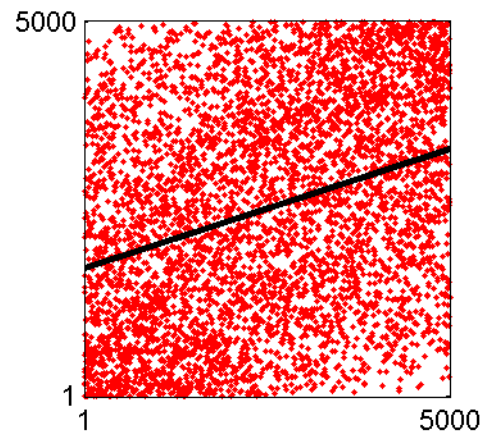
(g) Grid Spacer Form Loss



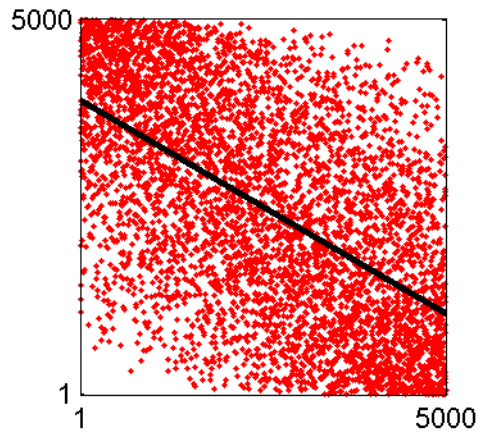
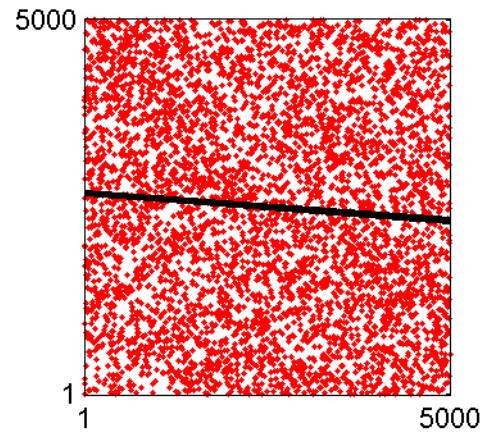
(h) Clad OD



(i) Gap Conductivity

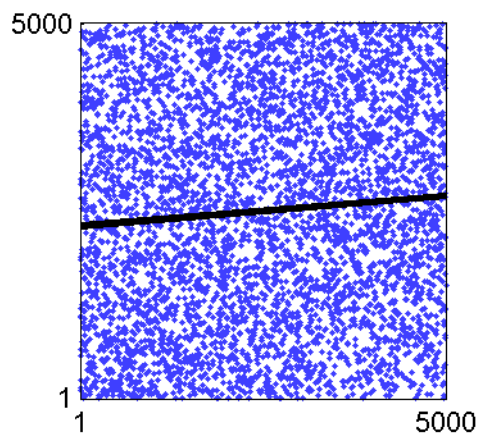


(j) Gap Distance

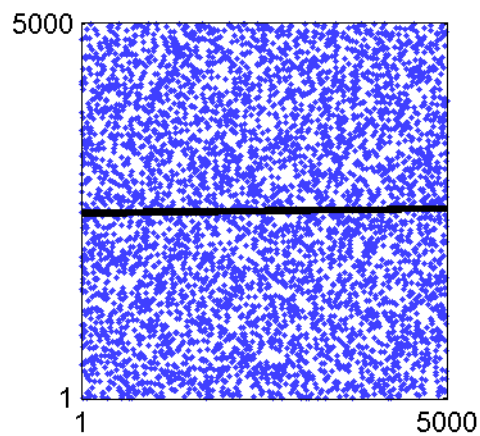
(k) UO<sub>2</sub> Fuel Conductivity

(l) Zirconium Conductivity

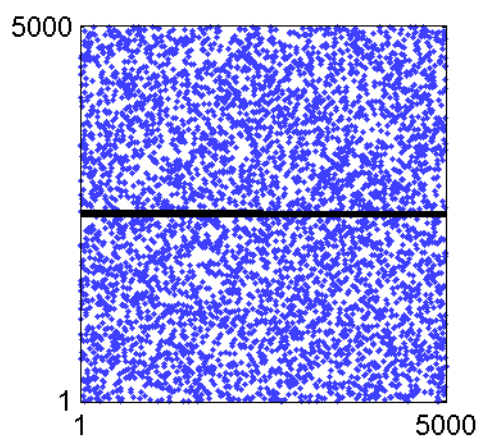
Figure A-10: RELAP5-3D maximum fuel temperature ranked sensitivity plots.



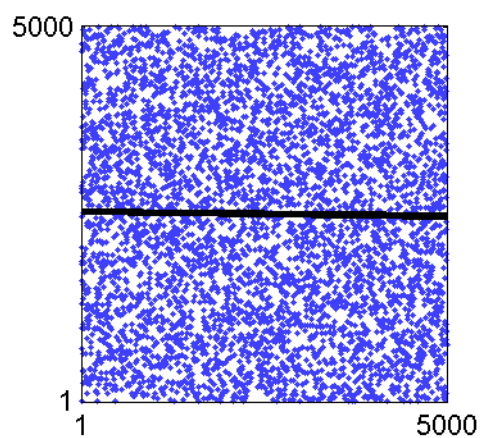
(a) Power



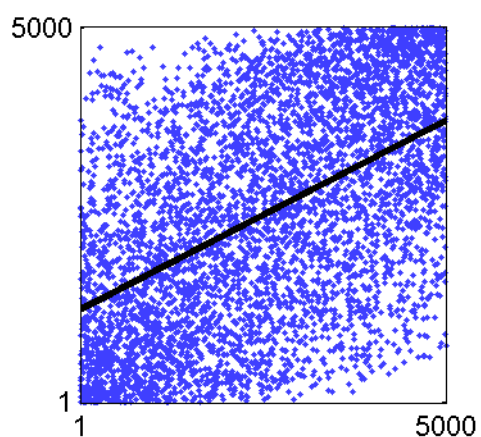
(b) Pressure



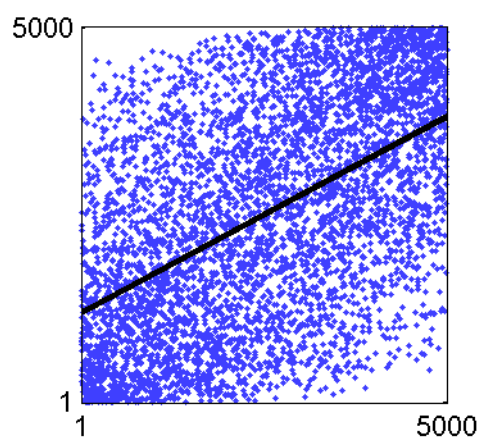
(c) System Flow



(d) Inlet Temperature



(e) Radial Power Factor



(f) Axial Power Factor

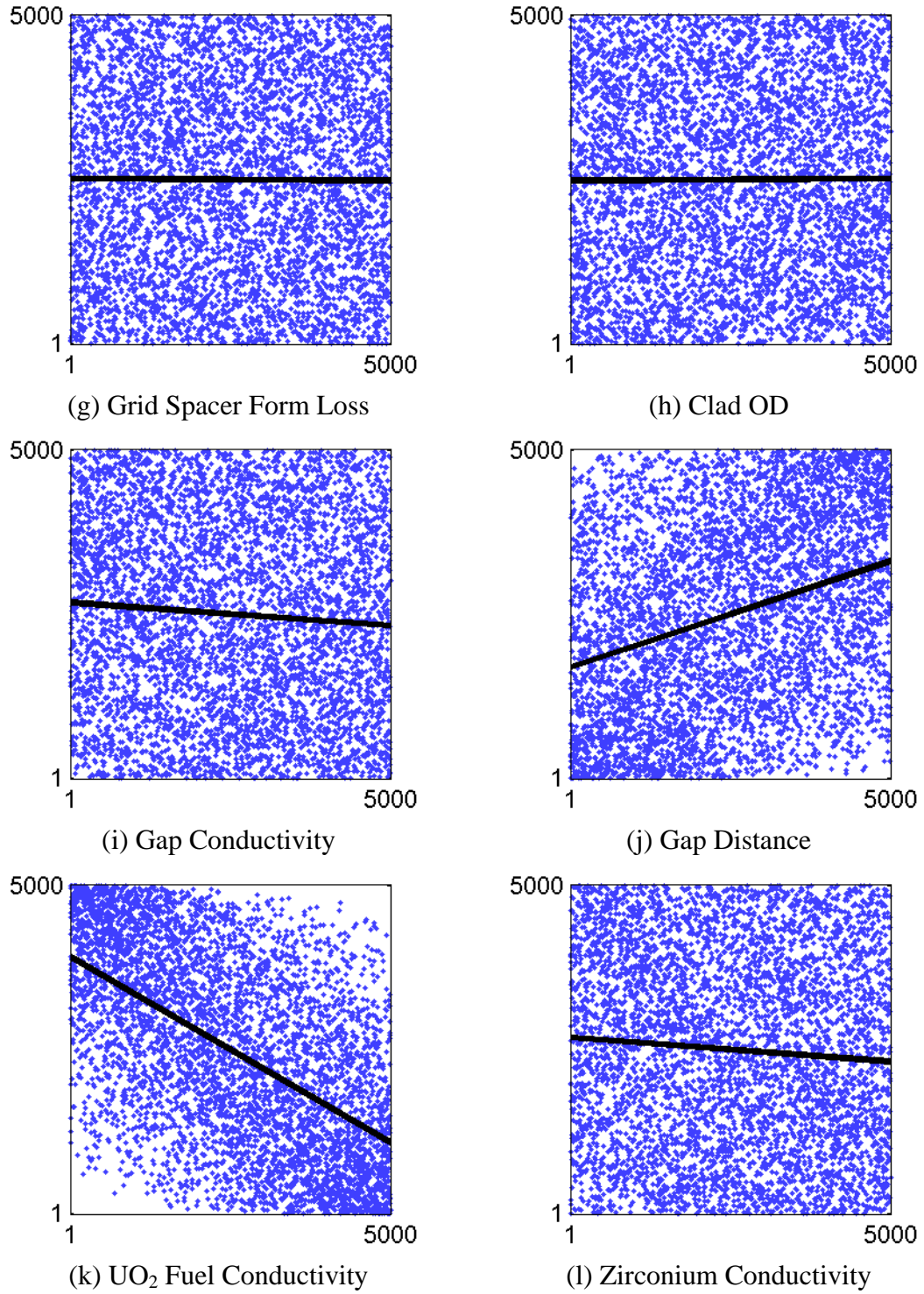
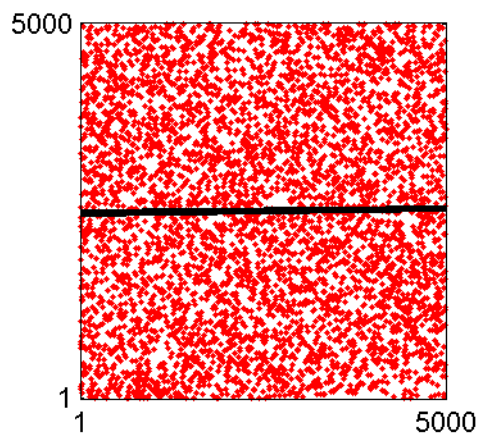
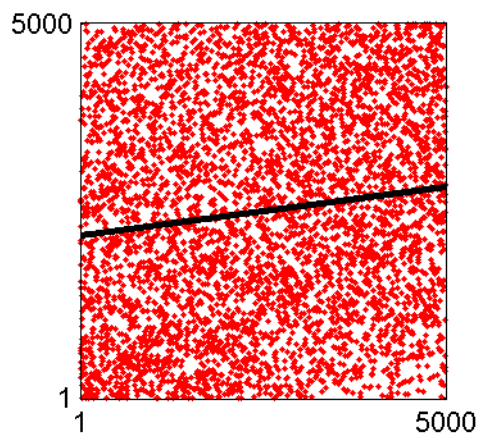


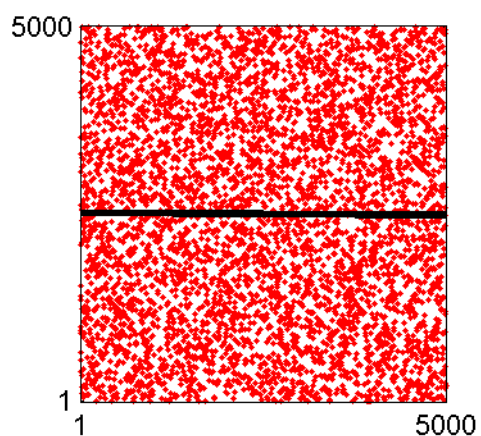
Figure A-11: VIPRE-01 maximum fuel temperature ranked sensitivity plots.



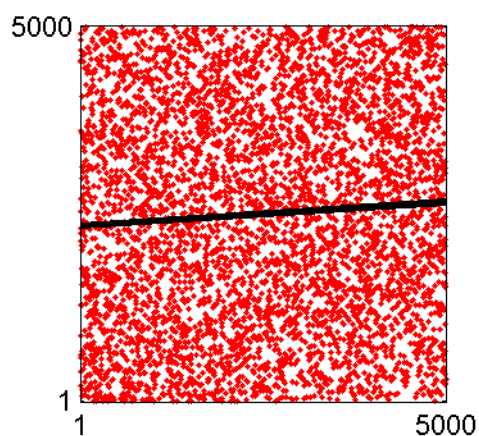
(a) Power



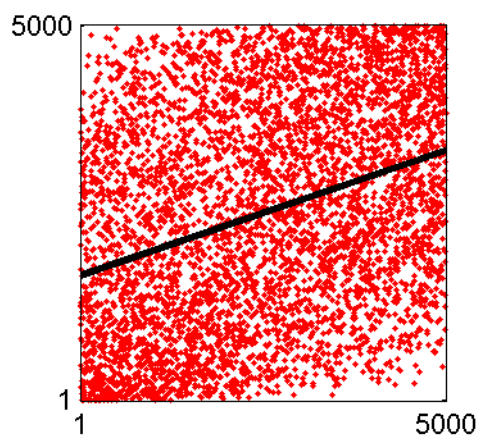
(b) Pressure



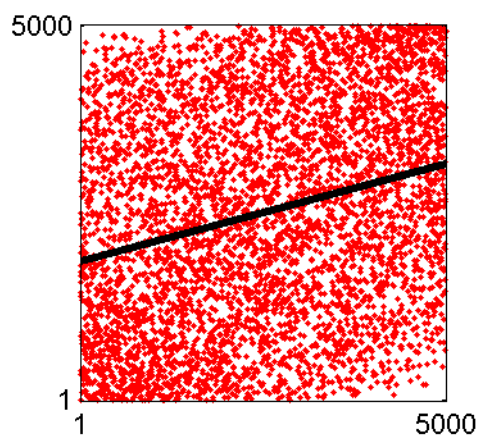
(c) System Flow



(d) Inlet Temperature



(e) Radial Power Factor



(f) Axial Power Factor

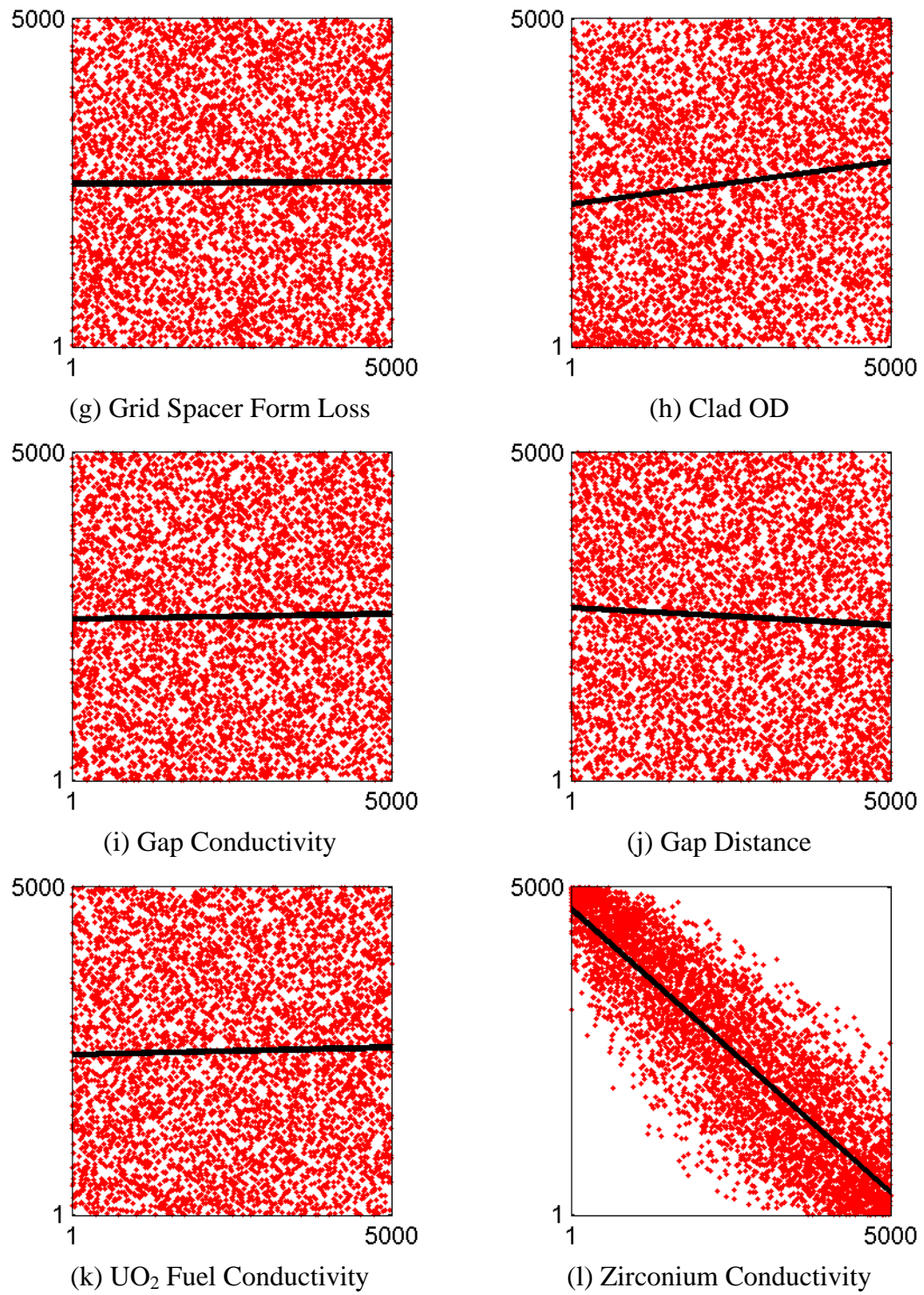
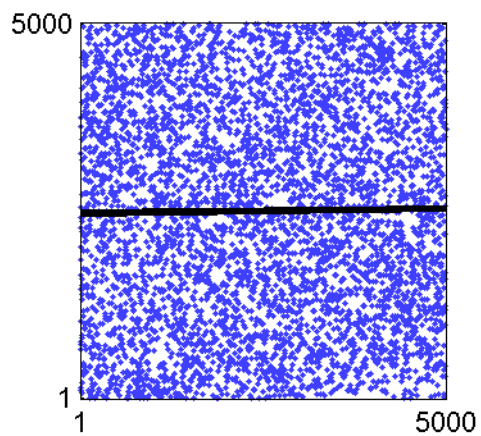
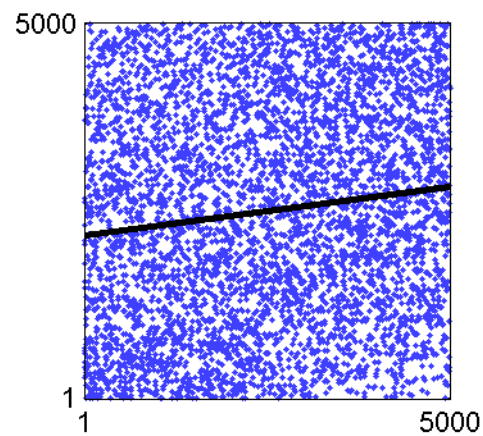


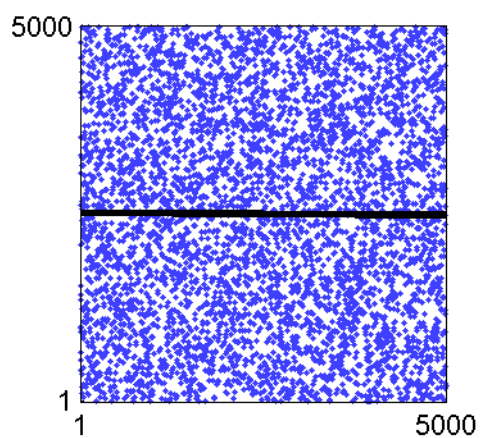
Figure A-12: RELAP5-3D maximum clad temperature ranked sensitivity plots.



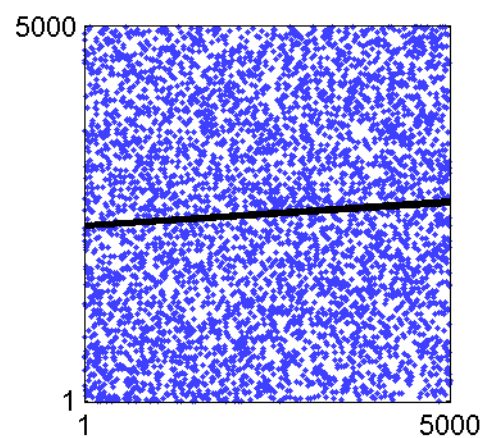
(a) Power



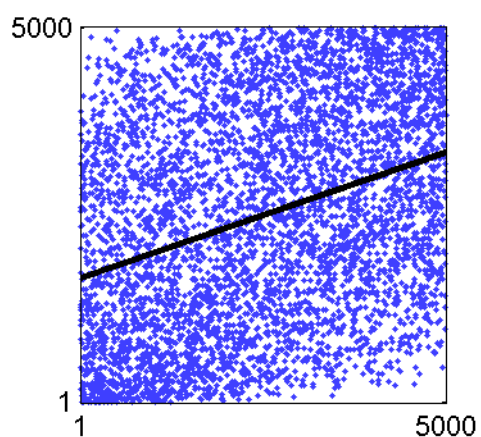
(b) Pressure



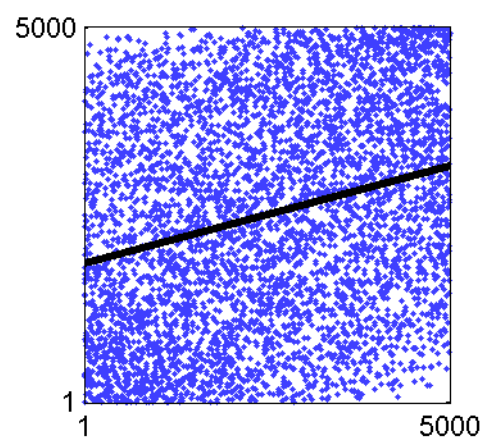
(c) System Flow



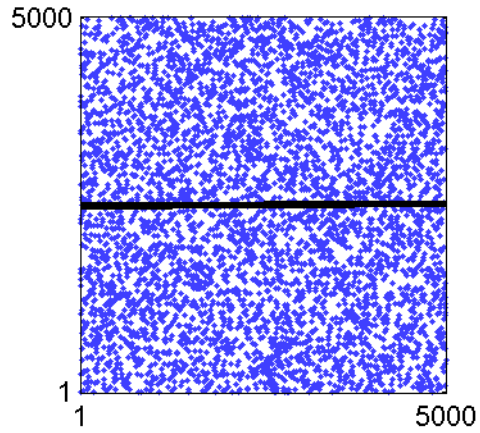
(d) Inlet Temperature



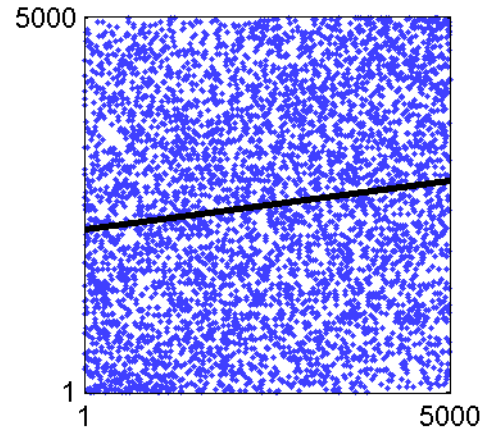
(e) Radial Power Factor



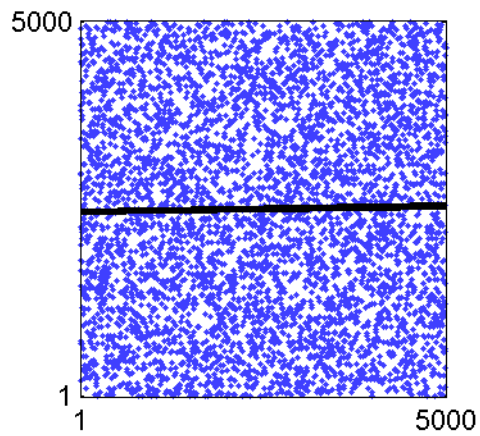
(f) Axial Power Factor



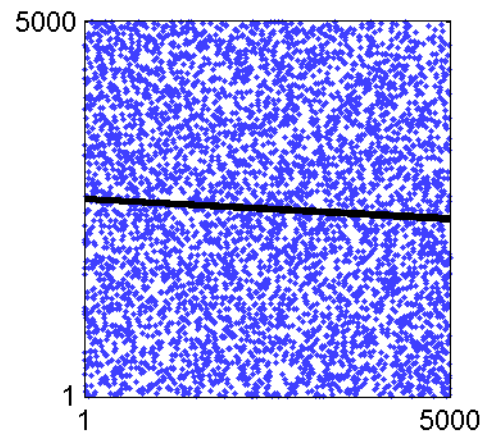
(g) Grid Spacer Form Loss



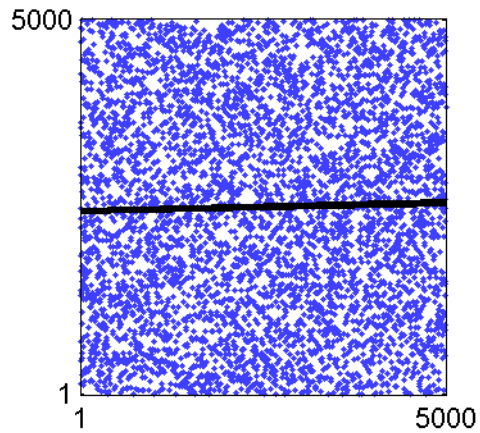
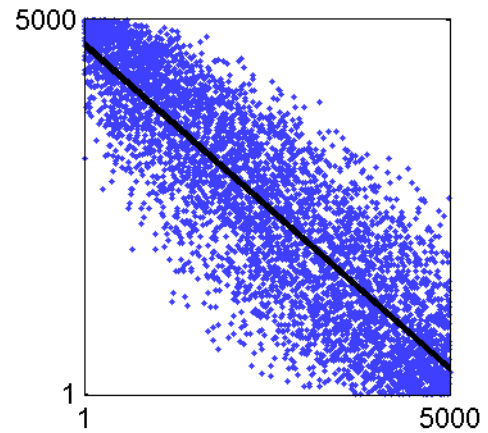
(h) Clad OD



(i) Gap Conductivity



(j) Gap Distance

(k) UO<sub>2</sub> Fuel Conductivity

(l) Zirconium Conductivity

Figure A-13: VIPRE-01 maximum clad temperature ranked sensitivity plots.